ON THE USE OF METAHEURISTIC ALGORITHMS FOR SOLVING CONDUCTIVITY-TO-MECHANICS INVERSE PROBLEMS IN STRUCTURAL HEALTH MONITORING OF SELF-SENSING COMPOSITES

by

Hashim Hassan

A Dissertation

Submitted to the Faculty of Purdue University

In Partial Fulfillment of the Requirements for the degree of

Doctor of Philosophy

School of Aeronautics and Astronautics

West Lafayette, Indiana

May 2021

THE PURDUE UNIVERSITY GRADUATE SCHOOL
STATEMENT OF COMMITTEE APPROVAL

Dr. Tyler N. Tallman, Chair

School of Aeronautics and Astronautics

Dr. William A. Crossley

School of Aeronautics and Astronautics

Dr. Fabio Semperlotti

School of Aeronautics and Astronautics

Dr. Vikas Tomar

School of Aeronautics and Astronautics

Approved by:

Dr. Gregory A. Blaisdell

.

For my wife & daughter.

ACKNOWLEDGMENTS

First and foremost, I would like to thank my advisor, Professor Tyler N. Tallman, for his guidance, wisdom, and unending support through my successes and failures in graduate school. Professor Tallman's meticulous nature and incredibly high standards have helped me produce work of exceptional quality and have elevated my writing and research skills. For this and much more, thank you Professor Tallman. I feel lucky to have had such an outstanding advisor.

I would also like to thank my committee members, Professor William A. Crossley, Professor Fabio Semperlotti, and Professor Vikas Tomar for sharing their wisdom, insight, and expertise. I especially thank Professor Crossley for introducing me to metaheuristic algorithms and for allowing me to use his genetic algorithm in my research. Without it, this thesis would not have been possible and I would not have had the tools to explore this exciting and challenging new subject.

I would like to thank Dr Pankaj Sharma for giving me the opportunity to work at the Energy Center and the Integrative Data Science Initiative (IDSI). I also want to thank the Purdue University Graduate School for providing financial support through the Bilsland Dissertation Fellowship.

I gratefully thank Dr Ben Denos, Dr Rebecca Cutting, and Professor R Byron Pipes in the Composites Manufacturing and Simulation Center (CMSC) for helping with DIC. I also gratefully thank graduate research assistant Nesredin Kedir and Professor Wayne Chen in the Impact Science Lab for their assistance with optical microscopy, and Dr Christopher Gilpin in the Purdue Life Sciences department for performing SEM imaging.

To my current and former lab mates, Julio Hernandez, Goon mo Koo, Akshay Jacob Thomas, and Ishan Karnik, I want to say a big thank you for the daily conversations, shared advice, and laughs. You have made my time at Purdue quite spectacular.

A big thank you to my mother and sister for their continuous support and encouragement throughout my education. Lastly, I want to express my deepest appreciation for my wife and daughter who have supported me through the best and worst of my times in graduate

school. Their love, warmth, and encouragement gave me the strength I needed to see my doctoral studies through to the end. Thank you, Qudsiya and Zayneb.

TABLE OF CONTENTS

LIST OF TABLES

LIST OF FIGURES

ABBREVIATIONS

CB	Carbon black
CFRP	Carbon fiber-reinforced polymer
CNF	Carbon nanofiber
CNT	Carbon nanotube
DCB	Double cantilever beam
EIT	Electrical impedance tomography
FEM	Finite element method
GFRP	Glass-fiber reinforced polymer
GA	Genetic algorithm
MWCNT	Multi-walled carbon nanotube
NDE	Nondestructive evaluation
PSO	Particle swarm optimization
SA	Simulated annealing
SHM	Structural health monitoring

ABSTRACT

Structural health monitoring (SHM) has immense potential to improve the safety of aerospace, mechanical, and civil structures because it allows for continuous, real-time damage prognostication. However, conventional SHM methodologies are limited by factors such as the need for extensive external sensor arrays, inadequate sensitivity to small-sized damage, and poor spatial damage localization. As such, widespread implementation of SHM in engineering structures has been severely restricted. These limitations can be overcome through the use of multi-functional materials with intrinsic self-sensing capabilities. In this area, composite materials with nanofiller-modified polymer matrices have received considerable research interest. The electrical conductivity of these materials is affected by mechanical stimuli such as strain and damage. This is known as the piezoresistive effect and it has been leveraged extensively for SHM in self-sensing materials. However, prevailing conductivity-based SHM modalities suffer from two critical limitations. The first limitation is that the mechanical state of the structure must be indirectly inferred from conductivity changes. Since conductivity is not a structurally relevant property, it would be much more beneficial to know the displacements, strains, and stresses as these can be used to predict the onset of damage and failure. The second limitation is that the precise shape and size of damage cannot be accurately determined from conductivity changes. From a SHM point of view, knowing the precise shape and size of damage would greatly aid in-service inspection and nondestructive evaluation (NDE) of safety-critical structures. The underlying cause of these limitations is that recovering precise mechanics from conductivity presents an under-determined and multi-modal inverse problem. Therefore, commonly used inversion schemes such as gradient-based optimization methods fail to produce physically meaningful solutions. Instead, metaheuristic search algorithms must be used in conjunction with physics-based damage models and realistic constraints on the solution search space. To that end, the overarching goal of this research is to address the limitations of conductivity-based SHM by developing metaheuristic algorithm-enabled methodologies for recovering precise mechanics from conductivity changes in self-sensing composites.

Three major scholarly contributions are made in this thesis. First, a piezoresistive inversion methodology is developed for recovering displacements, strains, and stresses in an elastically deformed self-sensing composite based on observed conductivity changes. For this, a genetic algorithm (GA) is integrated with an analytical piezoresistivity model and physics-based constraints on the search space. Using a simple stress-based failure criterion, it is demonstrated that this approach can be used to accurately predict material failure. Second, the feasibility of using other widely used metaheuristic algorithms for piezoresistive inversion is explored. Specifically, simulated annealing (SA) and particle swarm optimization (PSO) are used and their performances are compared to the performance of the GA. It is concluded that while SA and PSO can certainly be used to solve the piezoresistive inversion problem, the GA is the best algorithm based on solution accuracy, consistency, and efficiency. Third, a novel methodology is developed for precisely determining damage shape and size from observed conductivity changes in self-sensing composites. For this, a GA is integrated with physics-based geometric models for damage and suitable constraints on the search space. By considering two specific damage modes —through-holes and delaminations —it is shown that this method can be used to precisely reconstruct the shape and size of damage.

In achieving these goals, this thesis advances the state of the art by addressing critical limitations of conductivity-based SHM. The methodologies developed herein can enable unprecedented NDE capabilities by providing real-time information about the precise mechanical state (displacements, strains, and stresses) and damage shape in self-sensing composites. This has incredible potential to improve the safety of structures in a myriad of engineering venues.

1. LITERATURE REVIEW

1.1 Introduction

Engineering structures in high-risk applications such as aircraft and bridges can fail catastrophically. Figure 1.1 shows two recent examples of structural failure that can potentially result in significant loss of life. Both of these failures occurred due to the presence of undetected damage. In order to prevent structural failure, damage must be preemptively detected before it reaches a critical level and preventive measures must be taken. For the two cases shown in Figure 1.1, it may be argued that catastrophic failure could have been avoided through regular inspection and proper maintenance. This can be significantly challenging for large structures, such as bridges and buildings, as these require meticulous inspection for small-sized damage over large areas. Structures that incorporate advanced materials, such as composite airframes and wings, also present challenges. While these materials offer several benefits such as high strength-to-weight ratios and excellent manufacturability, it is well known that they suffer from matrix cracking, delamination, and fiber breakage. Even worse, these damage modes are often outwardly invisible. Due to the complexity of these failure modes, traditional damage tolerant design strategies that rely on intermittent inspection often prove insufficient for composites because they require a good understanding of damage initiation and growth mechanisms. Structural health monitoring (SHM) [1]–[4] has potential to address this limitation. SHM collectively refers to methodologies, technologies, and systems that continuously monitor the condition of a structure. Because SHM can enable real-time damage prognostication, it has incredible potential to improve the safety of engineering structures. Broadly speaking, SHM may be categorized into two main areas: conventional SHM, where external sensors are used to interrogate the structure, and SHM via self-sensing materials, where the materials used to design the structure function as their own sensors. The forthcoming sections examine both of these areas in detail.

(a)

(b)

Figure 1.1. Two recent examples of catastrophic structural failure. (a) Mid-flight engine failure on an Airbus A380 [5]. This occurred due to the presence of an undetected crack in the fan hub. (b) Collapse of a pedestrian bridge in Taiwan [6]. This occurred due to the accumulation of corrosion damage.

1.2 Conventional SHM

Conventional SHM encompasses a wide range of methodologies and systems that may be broadly categorized into three main categories: vibration-based SHM, guided wave-based SHM, and embedded sensor-based SHM. The basic premise of vibration-based SHM [7]–[10] is that damage affects the mass, stiffness, and energy absorption properties of the structure and therefore affects its dynamic response. The most commonly measured dynamic properties are the resonant frequencies and mode shape vectors. For example, Zhang et al. [11] were able to spatially localize delaminations with high accuracy in simply-supported and cantilever composite beams by measuring natural frequency shifts. Figure 1.2, taken from this study, shows the frequency shift as a function of position along the length of the beam and delamination size. In some cases, mode shape curvature changes [12] and dynamically measured flexibility changes [13] have also be used to locate damage. Vibration-based SHM is readily applicable to large structures but is often insensitive to small-sized damage. This is because the low-frequency response of a structure, which is the most practical dynamic response to measure, is generally not affected by small-sized defects.

Guided wave-based SHM [14]–[17] uses ultrasonic mechanical wave propagation to detect the presence of damage. The waves are forced to follow pre-defined paths along the structure (hence the term 'guided') and are dispersed or attenuated when they encounter a discontinuity such as a defect or a crack. In this area, Lamb waves have been used extensively to study cracks in thin plates and shells. For example, Sherafat et al. [18] used guided Lamb waves to investigate debonding in a composite skin-stringer panel. The waves were generated using a piezo-ceramic transducer and the authors studied the reflection, transmission, and scattering of the waves using laser Doppler vibrometry (LDV) when an artificially induced delamination was encountered. Figure 1.3, taken from this study, compares the influence of excitation frequency and mode number on the scattering behavior between the damaged and undamaged panels. In other cases, Rayleigh waves have been used for damage detection. For example, Chakrapani and Dayal [19] used A- and B-scans to study how Rayleigh waves undergo mode conversion into Lamb waves when they encounter the leading edge of a delamination. The authors also proposed a method for determining delamination thickness

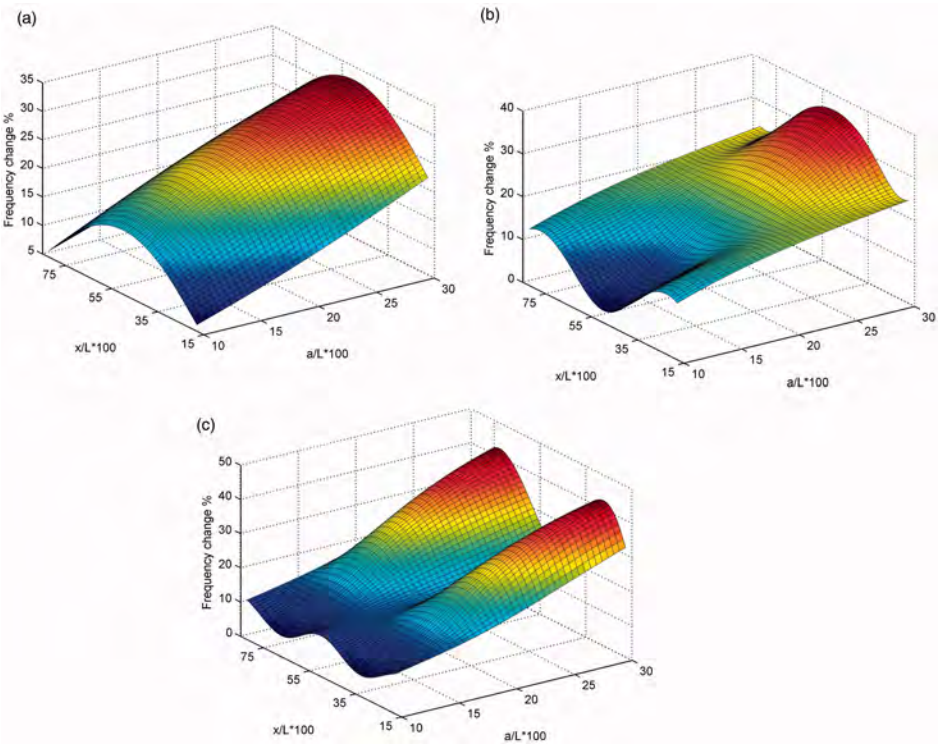

Figure 1.2. Resonant frequency shift of (a) mode 1, (b) mode 2, and (c) mode 3, as a function of position along the length of the beam (x/L) and delamination size (a/L) in a simply supported composite beam [11].

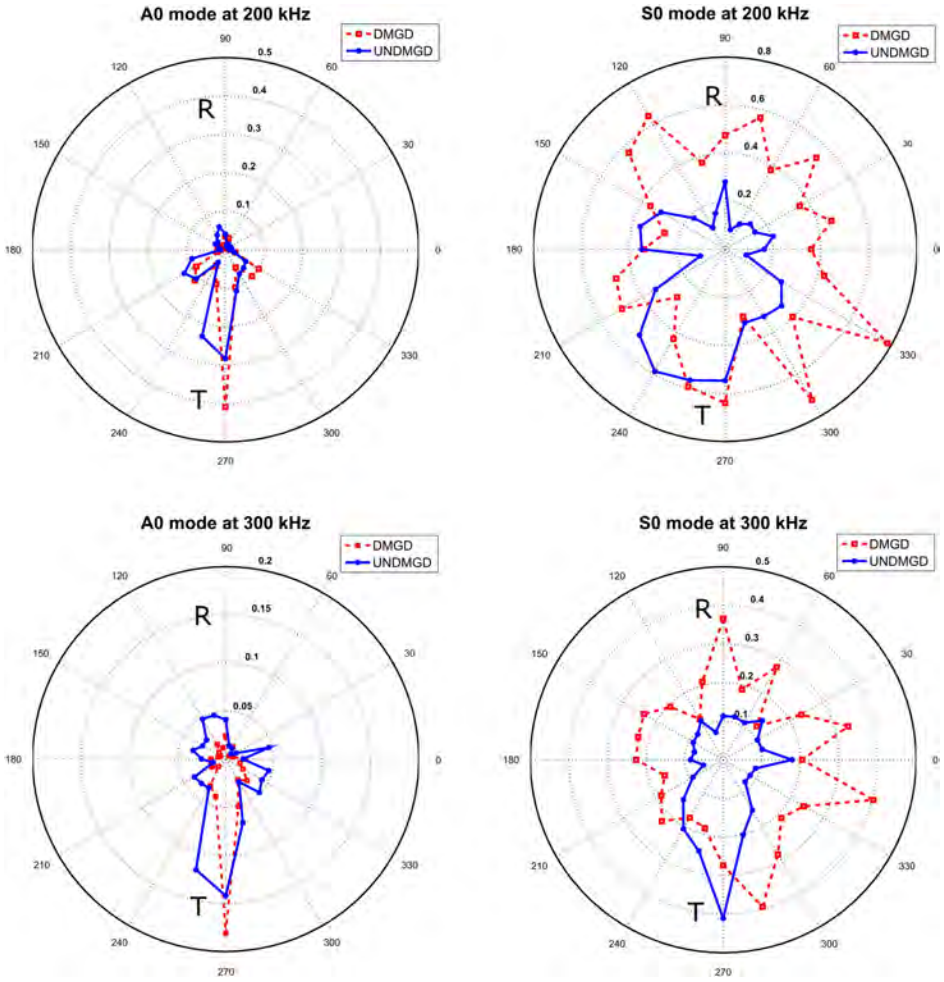

Figure 1.3. Influence of excitation frequency and mode number on the scattering behavior of the waves in damaged and undamaged panels [18]. The $A0$ mode is an anti-symmetric mode and the $S0$ mode is a symmetric mode.

by measuring Lamb wave velocity and dispersion inside the delamination. These studies show that high-frequency guided waves can be used to detect small-sized defects with good precision. Also, large areas can be scanned with a relatively small number of ultrasonic transducers. However, physical integration of the transducers within the structure is required to generate and catch the waves.

Lastly, consider embedded sensor-based SHM, where the structure is instrumented with sensors that monitor the local mechanical, electrical, thermal, and chemical condition of the structure. The most commonly used sensors for composite structures include strain gauges [20]–[22], piezoelectric sensors [23]–[26], and fiber-optic sensors [27]–[32]. Strain gauges relay

changes in electrical resistance to the local strain state of the material. These are are extremely common in experimental testing of composites and other structural materials [33]. Piezoelectric sensors consist of materials that convert mechanical effects (such as applied strain and pressure) into electrical signals. For example, Vitola et al. [34] developed a piezoelectric sensing system for detecting temperature changes and evaluated the performance of the sensor on a composite plate subjected to temperature variations. A schematic of the sensor arrangement and the response of a single sensor to changing temperatures is shown in Figure 1.4. In fiber-optic sensing, optical fibers are embedded within the material and changes in the light transmission properties of the fibers are used to measure the local strain state. Numerous types of fiber-optic sensors have been explored, each with their own strengths and weaknesses. Intensity-modulated sensors [35] measure changes in the intensity of the transmitted light. These are simple to implement but are susceptible to light fluctuations. Interferometric sensors [36] measure strain by recording phase changes in the transmitted light. For example, Jothibasu et al. [37] developed an interferometric sensor based on Rayleigh backscattering and used the sensor to successfully detect strains in cross-ply and unidirectional composites loaded in tension. A schematic of the experimental setup and the strains measured using the sensor are shown in Figure 1.5. Interferometric sensors have excellent sensitivity to small strains but can be difficult to develop into distributed sensing networks. Fiber Bragg grating (FBG) sensors [38] incorporate reflective Bragg gratings that experience wavelength changes when subjected to applied strains. FBGs are simple to implement but are very sensitive to temperature changes. In general, embedded sensors have excellent sensitivity to small-sized defects and can detect localized damage with good accuracy. However, similar to guided wave-based SHM, these sensors need to be physically integrated within the structure. Additionally, numerous sensors are needed for damage monitoring over large areas. In the case of fiber-optic sensors, this can weaken the material [39], [40].

Although conventional SHM is widely used and highly effective, it suffers from several limitations such as the need for external sensors and actuators, inadequate sensitivity to small-sized defects, and practical limitations associated with damage monitoring in large structures. These limitations can be addressed through the use of materials with intrinsic

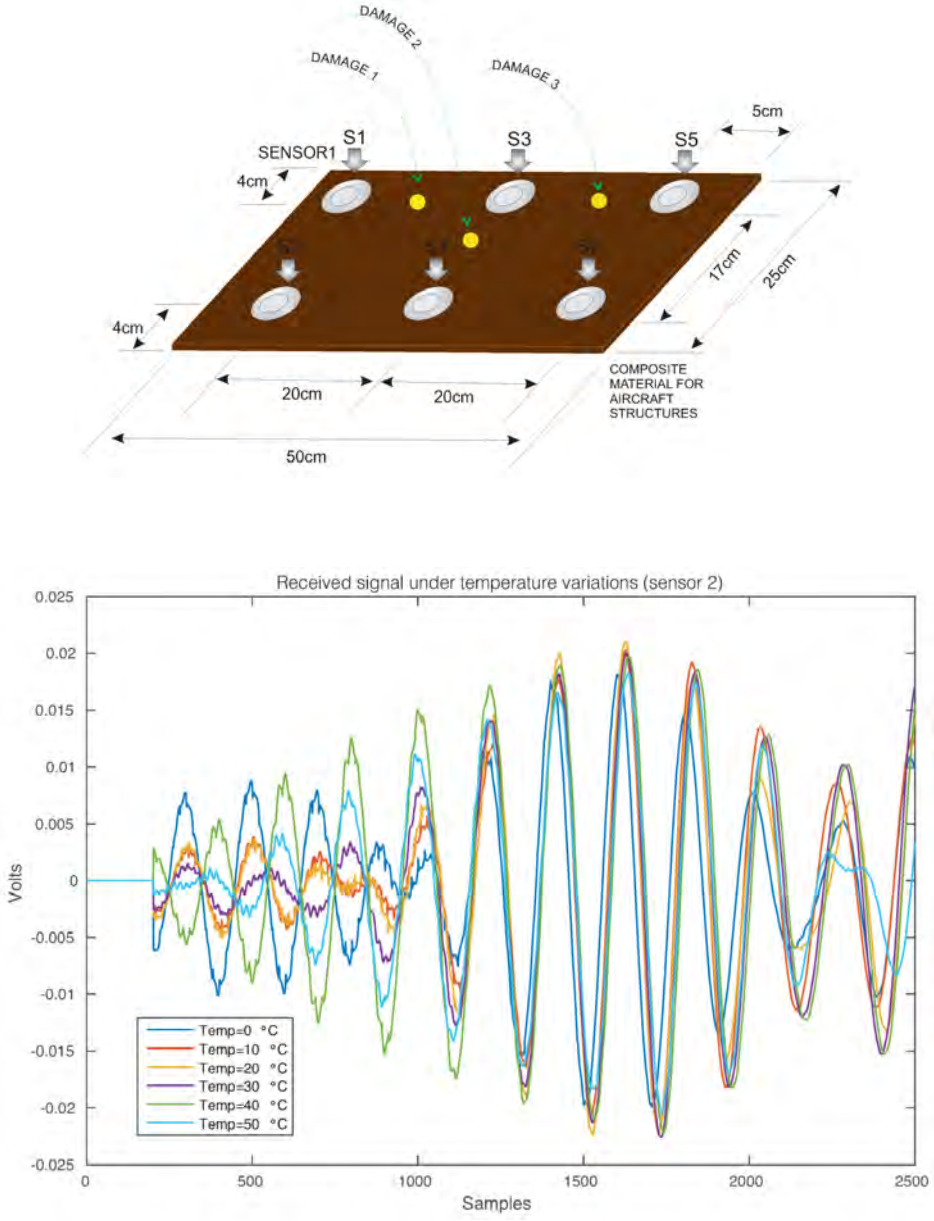

Figure 1.4. Performance of a piezoelectric temperature sensing system evaluated on a composite plate subjected to temperature variations [34]. Top: Schematic of composite plate showing the sensor locations (indicated by the S's). Bottom: Signal received by sensor S2 due to various applied temperatures.

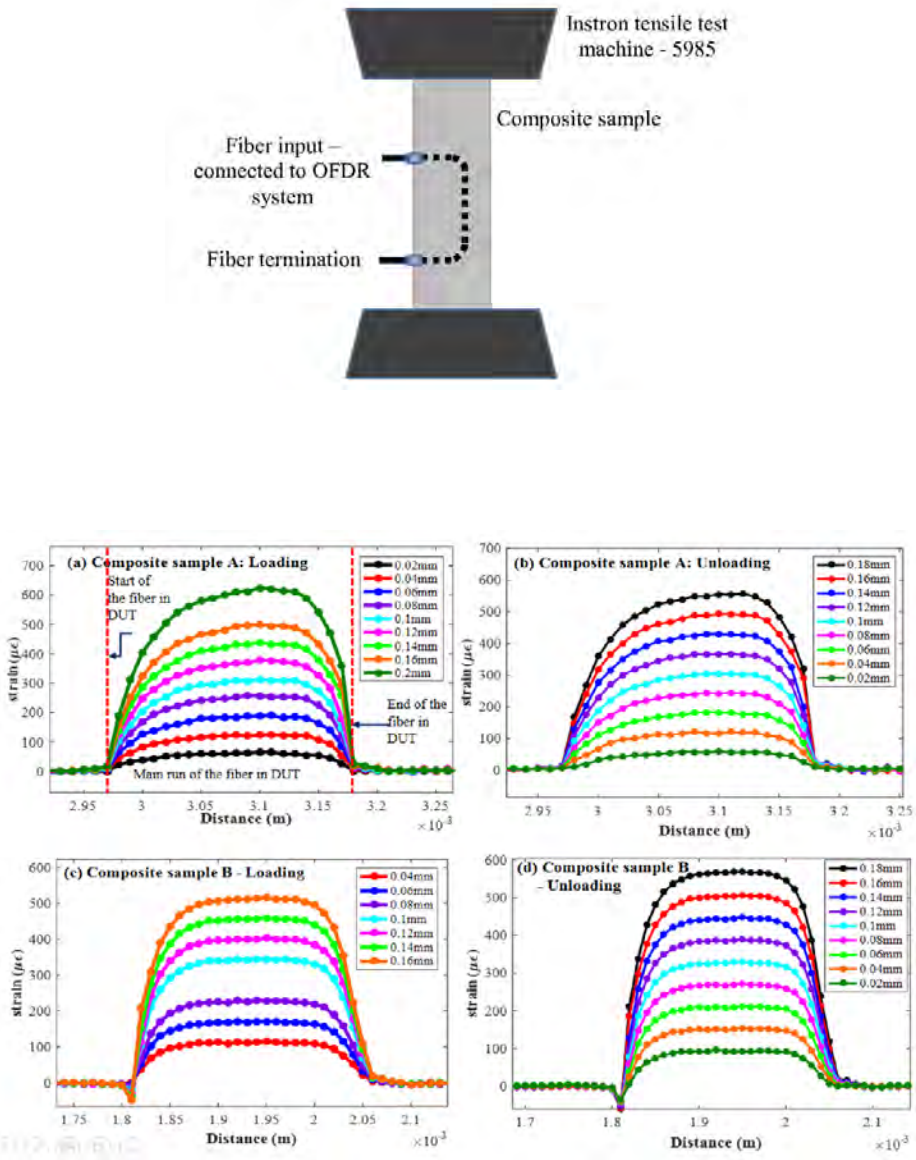

Figure 1.5. Fiber-optic sensor used to measure tensile strains in composite laminates [37]. Top: Schematic of experimental setup. The fiber-optic sensor was embedded inside the laminate and connected to an optical frequency domain reflectometry (OFDR) system. Bottom: Strains measured for loading and unloading cycles of sample A (cross-ply laminate) and sample B (unidirectional laminate). The different colored lines indicate different applied displacements.

self-sensing capabilities. The next section discusses how self-sensing materials can be used for SHM.

1.3 Self-Sensing SHM

Self-sensing materials possess one or more stimulus-responsive properties that allow them to 'sense' their condition. Changes in these properties can therefore be relayed to changes in the mechanical, thermal, and even chemical state of the material. As opposed to discrete, point-based sensors that only provide information local to their vicinity, self-sensing materials can provide information at every point since the material functions as its own sensor. In the context of SHM, this means that structures incorporating self-sensing materials can enable spatially continuous, real-time damage sensing over large areas and complex geometries. One particular category of self-sensing materials that has attracted considerable research interest for SHM is nanofiller-modified materials. These materials are electrically conductive because the nanofillers form percolating networks for electron transport. As a representative example, Figure 1.6 shows scanning electron microscopy (SEM) images of polyurethane modified with carbon nanofibers (CNFs). When an external mechanical stimulus, such as strain or damage, is applied to a self-sensing material, it can reorient the nanofiller networks, affect the tunneling resistance felt by mobile electrons, and cause a change in conductivity. This self-sensing property, whereby mechanical effects manifest as changes in electrical conductivity, is known as piezoresistivity. The piezoresistive effect is qualitatively illustrated in Figure 1.7. Piezoresistivity has been extensively explored in several material systems including polymer composites [41]–[47], cements and concrete [48]–[51], ceramics [52], [53], and alloys [54]–[56]. SHM in piezoresistive materials typically employs one of three methods for detecting strain and/or damage: 1-D resistance change methods, 2-D resistance change methods, and tomographic imaging.

1.3.1 1-D Resistance Change Methods

In 1-D resistance change methods, the structure is instrumented with a single pair of electrodes. The resistance between the electrodes is measured as the structure experiences

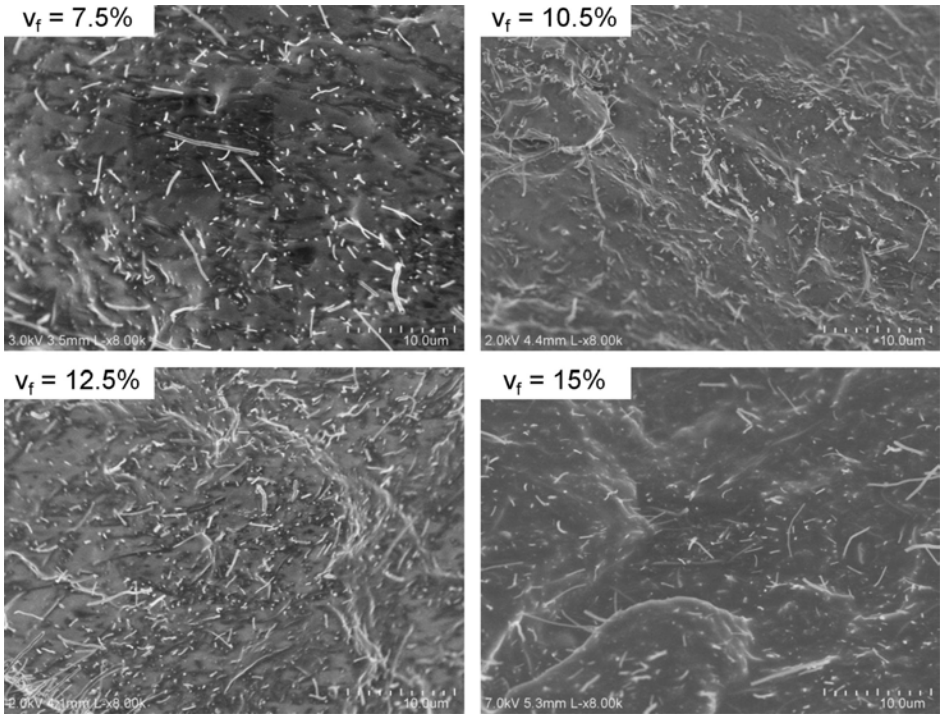

Figure 1.6. Scanning electron microscopy (SEM) images of a self-sensing CNF-modified polyurethane nanocomposite with different nanofiller volume fractions [42].

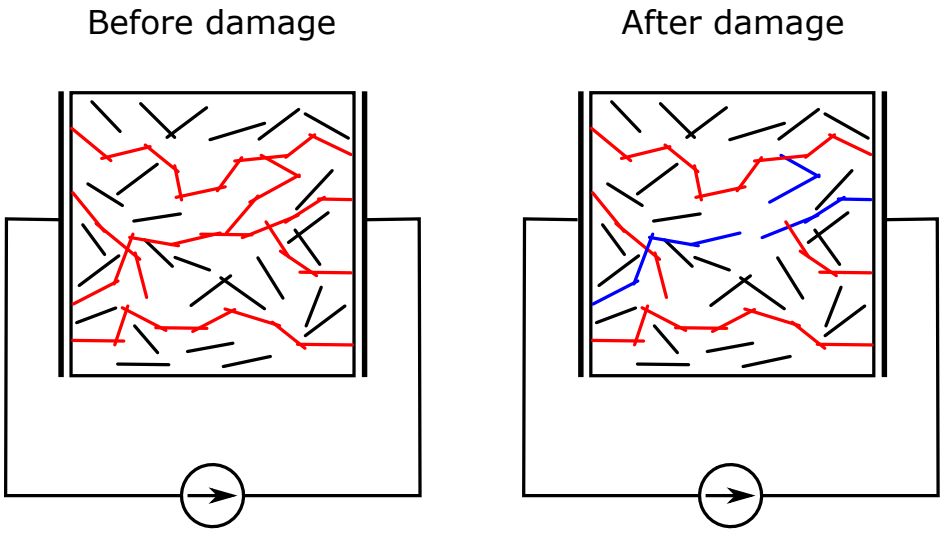

Figure 1.7. Qualitative illustration of the piezoresistive effect in nanofiller-modified materials. Right: Nanofillers dispersed inside the material form well-connected electrically conductive pathways, indicated in red. Left: Damage occurs and severs the connectivity between proximate nanofillers, indicated in blue. This manifests as a change in electrical conductivity.

damage or deformation. Under elastic loading in tension, the resistance increases as the nanofiller networks are stretched and the distance between neighboring nanofillers increases. Conversely, under elastic compression, the inter-filler distance decreases as the nanofillers are pushed closer together and the resistance decreases. In both cases the resistance generally returns to its original value when the load is removed (assuming the deformations are indeed purely elastic). At the onset of material failure, the resistance increases dramatically and does not return to its original value even after the load is removed. Murray et al. [57] observed the reversibility of resistance changes in a unidirectional E-glass composite modified with carbon nanotubes (CNTs) under elastic deformation using 1-D resistance changes. The composite was machined into tensile specimens and a single electrode pair was applied to each specimen to measure the resistance change during tensile loading. It was also observed that as damage accumulates in the form of transverse matrix cracks and delaminations, irreversible resistance changes occur due to permanent severing of conductive networks. Similarly, Panozzo et al. [58] developed an analytical model to track the growth of delaminations in a multi-directional carbon fiber-reinforced epoxy laminate and validated it experimentally using 1-D resistance changes in a DCB configuration. The electrodes were painted on the top and bottom surfaces of the DCB and the resistance change was recorded during the test. Generally, 1-D resistance changes are reported by plotting the normalized resistance change, $\Delta R/R_0$, as a function of the applied load or strain. In this case, the authors reported $\Delta R/R_0$ as a function of delamination extension, as shown in Figure 1.8. Other work has investigated the use of 1-D resistance changes for monitoring monotonic [59], [60] and fatigue [61]–[63] loading as shown in Figure 1.9, studying mechanisms of delamination toughening [64], and characterizing the strain sensitivity of novel material-based sensors [65]–[68]. Although 1-D resistance changes are simple to implement and are very useful for detecting the onset and growth of damage, they provide no information about the location of damage within the structure other than its mere presence between the electrodes. This limitation can be addressed using 2-D resistance change methods.

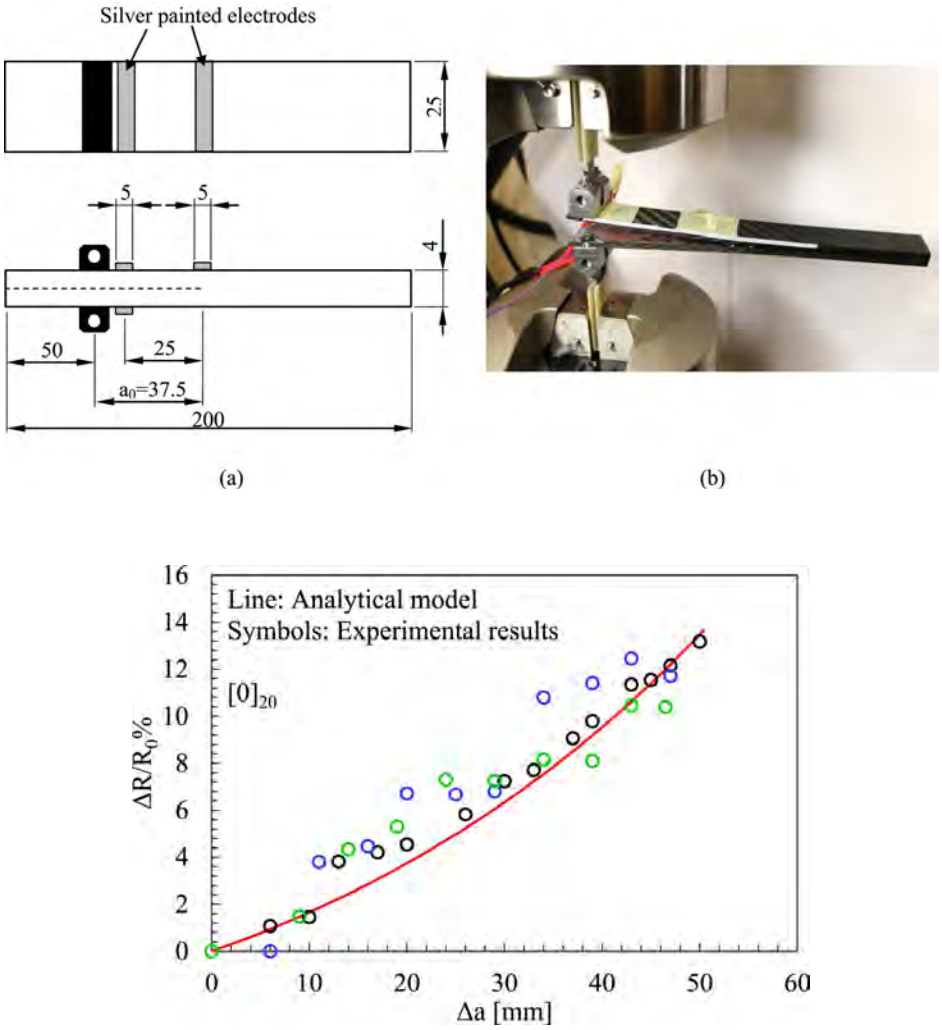

Figure 1.8. 1-D resistance changes used to measure delamination extension in a self-sensing DCB specimen [58]. Top: (a) Schematic showing specimen dimensions and electrode arrangement. (b) Photo of experimental setup. Bottom: Normalized resistance change as a function of delamination extension. Note that the resistance increases as the delamination grows.

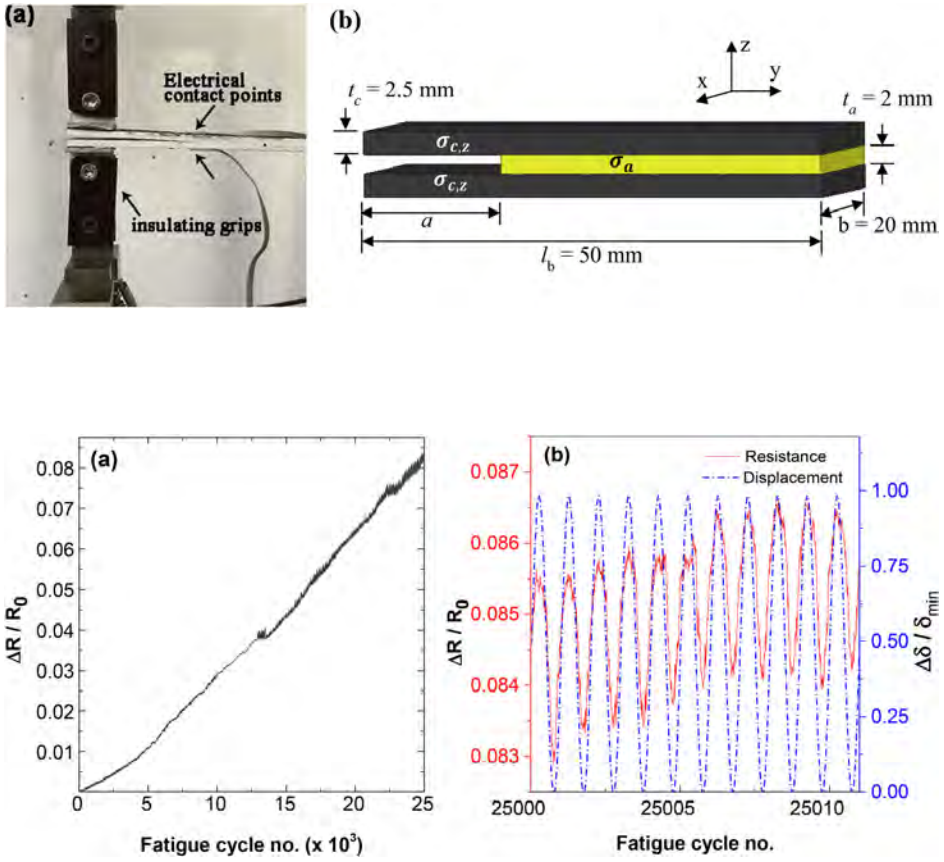

Figure 1.9. 1-D resistance changes used to measure damage growth in a CNF-modified carbon fiber-reinforced polymer (CFRP) under cyclic fatigue loading [61]. Top: (a) Photo of experimental loading setup. (b) Schematic of specimen geometry. Bottom: Normalized resistance change plots for (a) 5 Hz and (b) 0.01 Hz cyclic fatigue frequency.

1.3.2 2-D Resistance Change Methods

2-D resistance change methods extend the principle of 1-D resistance change methods by instrumenting the structure with a grid or an array of electrodes rather than a single pair. The resistance changes between adjacent electrodes are measured before, during, and after a damage causing event has occurred. Damage can then be detected and spatially localized by identifying the electrode pair with the largest resistance change. For example, Naghashpour and Van Hoa [69], [70] used 2-D resistance changes to detect damage in carbon fiber-reinforced epoxy modified with multi-walled carbon nanotubes (MWCNTs). Rectangular composite plates with different weight fractions of MWCNT were manufactured and instrumented with grids of evenly spaced electrodes. The resistance change between the electrodes was used to detect and localize through-hole and impact damage, as shown in Figure 1.10. Discrete resistance changes between electrodes can be interpolated to produce a spatially continuous resistance change distribution. For example, Viets et al. [71] instrumented the top surface of a MWCNT-modified GFRP composite with a grid of electrodes. They then used 2-D interpolated resistance changes to produce a continuous resistance change distribution and locate impact damage in the plate, as shown in Figure 1.11. Similarly, Zhang et al. [72] used 2-D interpolated resistance changes for impact damage assessment in a GFRP composite modified with carbon black (CB) and copper chloride (CC) fillers. Other work in this area has specifically studied the effects of delaminations on the electrical properties of nanofiller-modified composites using 2-D electrode grids and arrays [73]–[78]. Although 2-D resistance change methods have much better spatial damage localization capabilities than 1-D resistance change methods, they generally require a dense grid of electrodes for good resolution. For example, in the case of Viets et al. [71], a total of 100 electrodes were used to produce the image shown in Figure 1.11. Similarly, Zhang et al. [72] used a total of 81 electrodes to produce images that were comparable in quality to ultrasonic C-scans.

1.3.3 Tomographic Imaging

Tomographic imaging techniques continuously image the internal resistivity or conductivity of a structure. In contrast to 1-D and 2-D resistance change methods which simply

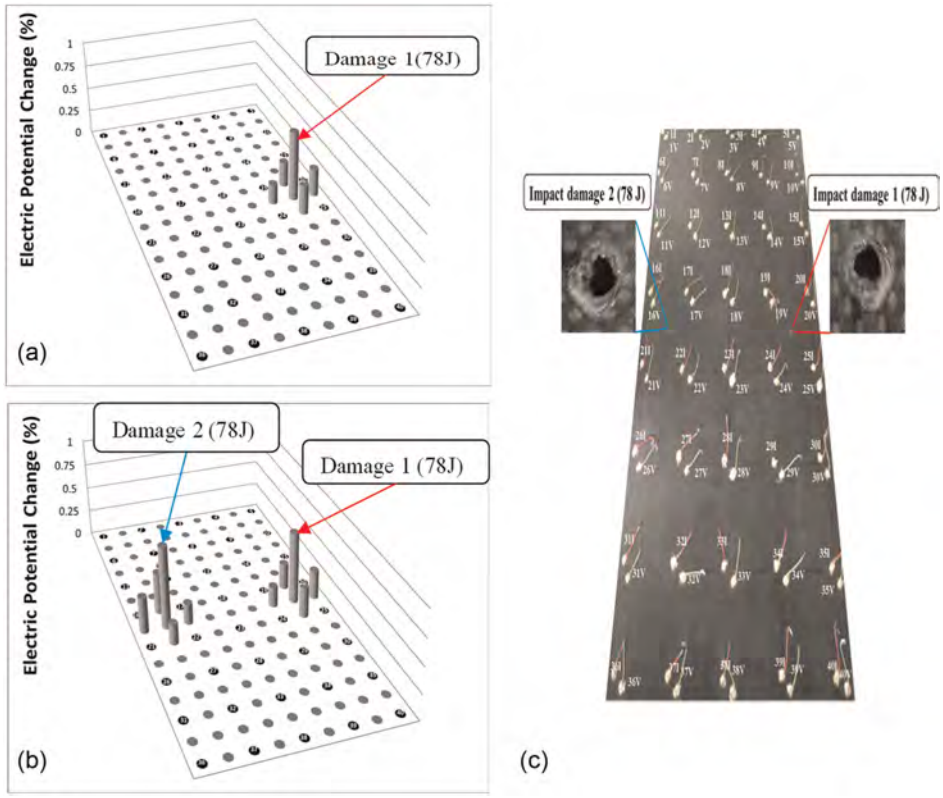

Figure 1.10. An example of using discrete 2-D resistance changes to detect impact damage in a MWCNT-modified carbon fiber-reinforced composite plate [69]. The resistance change is largest in the regions where damage has occurred.

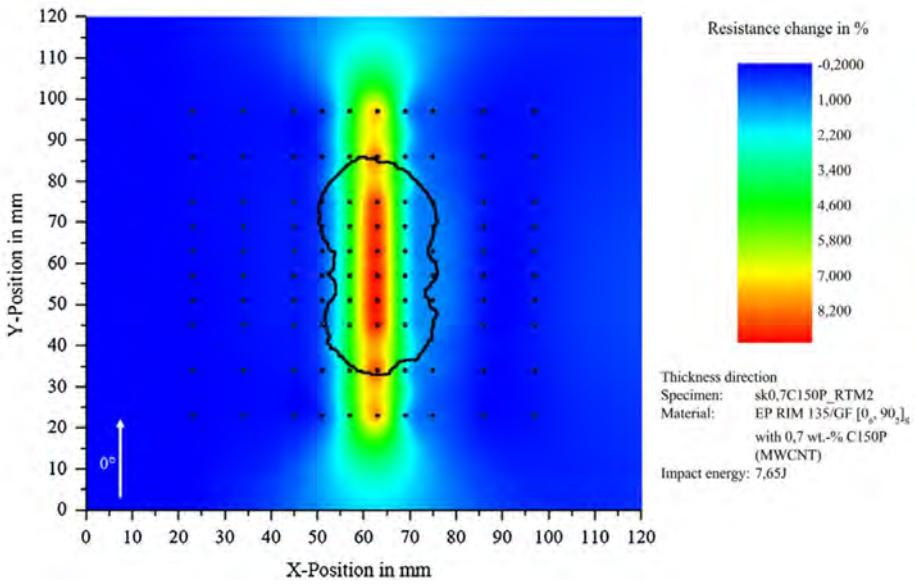

Figure 1.11. An example of using interpolated 2-D resistance changes for impact damage detection in a MWCNT-modified carbon fiber-reinforced composite plate [71]. The black dots indicate the electrode locations and the black outline indicates the actual impact damage shape obtained via ultrasonic C-scan. A total of 100 electrodes were used in this study.

interpolate between discrete resistance measurements, tomographic imaging models the underlying physics of electric diffusion within the structure to produce a spatially continuous resistance distribution. In this area, electrical impedance tomography (EIT) is a widely used technique. EIT was originally developed for geospatial imaging [79] but it has also found extensive use in medical imaging [80]–[83] because it is low-cost, non-invasive, portable, and has nearly real-time imaging capabilities. Recently, EIT has emerged as a viable SHM modality for self-sensing materials due to the piezoresistive effect [84]. The expansive body of work in this area may be categorized by the type of structure being interrogated.

The first category of research uses EIT for SHM in structures that are inherently self-sensing because they incorporate self-sensing materials. Most work in this area has focused on detecting damage in planar structures such as thin composite plates. For example, Dai et al. [85] used EIT to image cut-outs, cracks, and impact damage in a rectangular CNT-based aramid nanocomposite. The EIT results for cut-out imaging from this study are shown in Figure 1.12. Similarly, Tallman et al. [86] used EIT to image through-hole and impact damage in a GFRP composite modified with carbon black (CB) nanofillers, as shown in Figure 1.13. Other work in planar structures has explored the use of EIT for imaging damage in CNF-modified epoxy [87] and CFRP [88], [89] plates. In non-planar structures, Thomas et al. [90] successfully used EIT for imaging through-hole and impact damage in self-sensing composite tubes, as shown in Figure 1.14.

The second category of research uses EIT for SHM in structures that are not inherently self-sensing but employ external self-sensing media for detecting strain and damage. In this area, considerable work has been done toward the development of polymer-based sensing skins and films [91]–[95]. These skins generally consist of conductive fillers suspended in a polymer matrix and are therefore piezoresistive. The skins can be applied to both highly-conductive and non-conductive structures. Any damage or deformation in the structure causes damage or deformation in the skin and manifests as a change in conductivity. For example, Hou et al. [92] developed a CNT-based sensing skin using a layer-by-layer (LbL) technique. The skin was then damaged in various locations and EIT was used to image the resulting conductivity change. The researchers also applied the skin to a ductile polyvinyl chloride (PVC) test coupon, loaded the coupon in tension, and observed a decrease in the

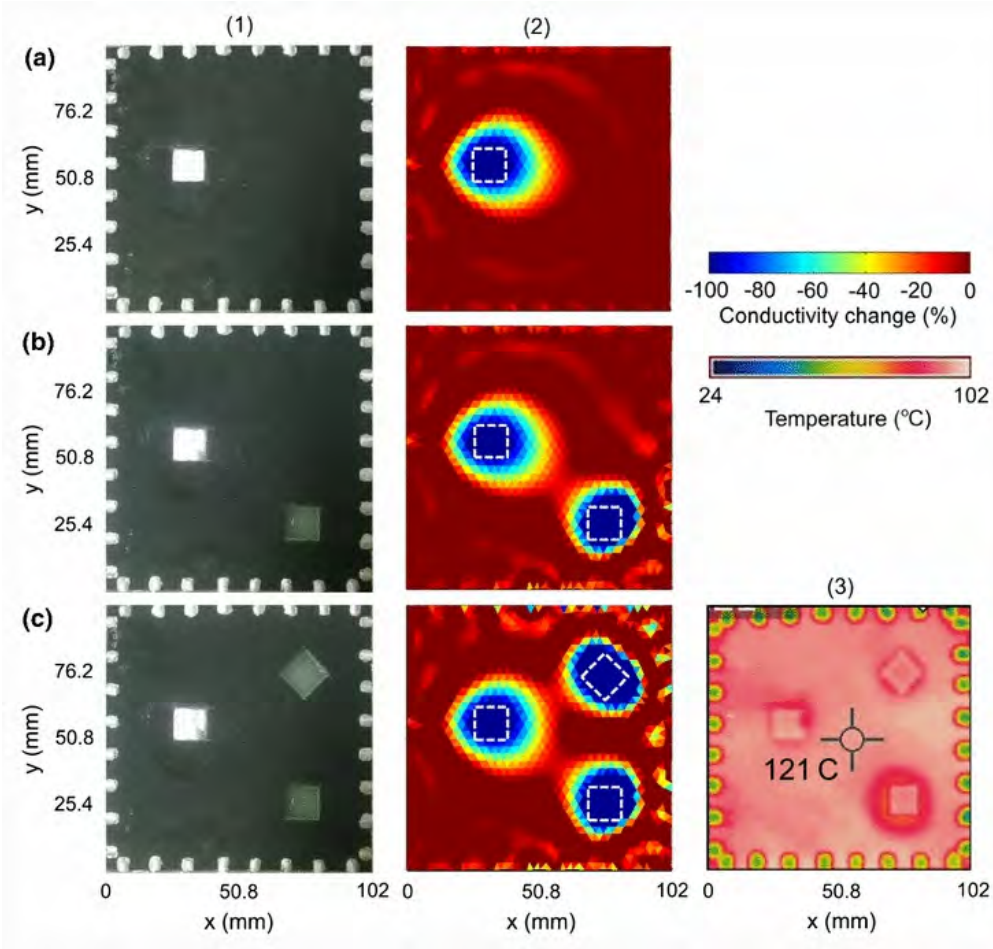

Figure 1.12. EIT used to image cut-out damage in a CNT-based aramid fabric plate [85]. Rows (a) to (c) corrspond to the number of square holes cut out. Column (1) shows top-down photos of the sensor, column (2) shows the corresponding EIT image, and column (3) shows a temperature distribution obtained via infrared (IR) thermography.

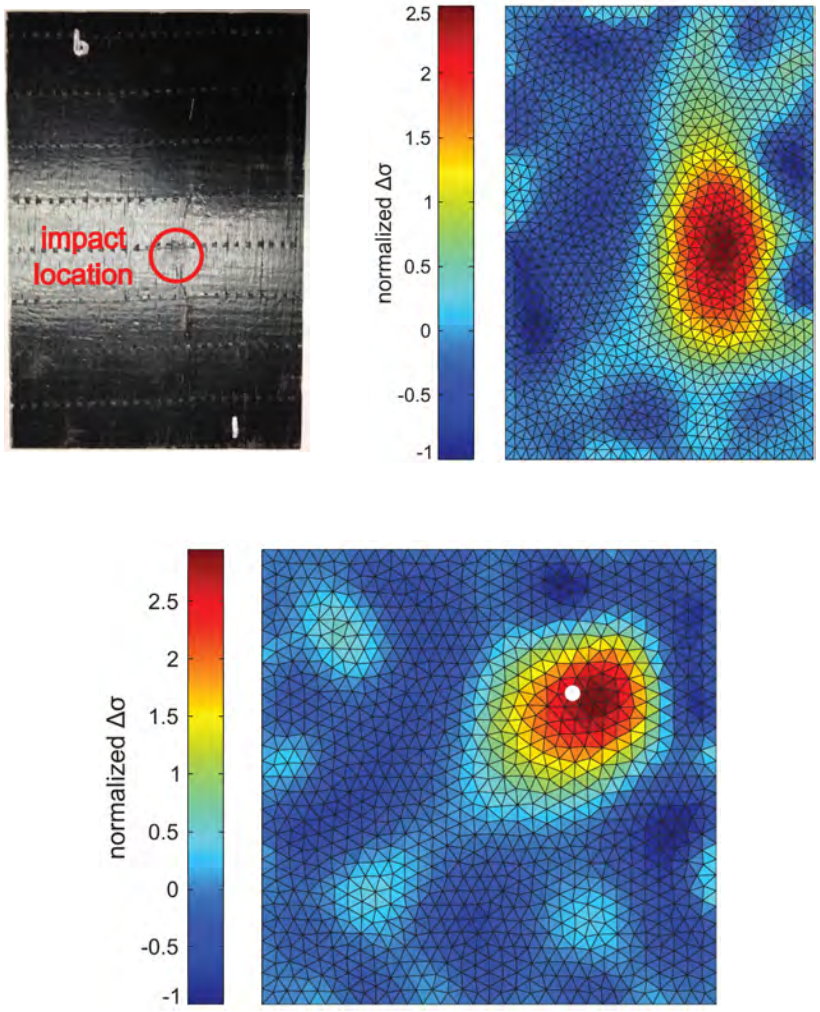

Figure 1.13. EIT used to image through-hole and impact damage in GFRP composites with CB nanofillers [86]. Top left: CB-modified GFRP plate with impact location labeled. Top right: EIT-imaged conductivity change for impacted plate. Bottom: Conductivity change for plate with 3.18 mm diameter through-hole. The white circle indicates the actual location and size of the hole.

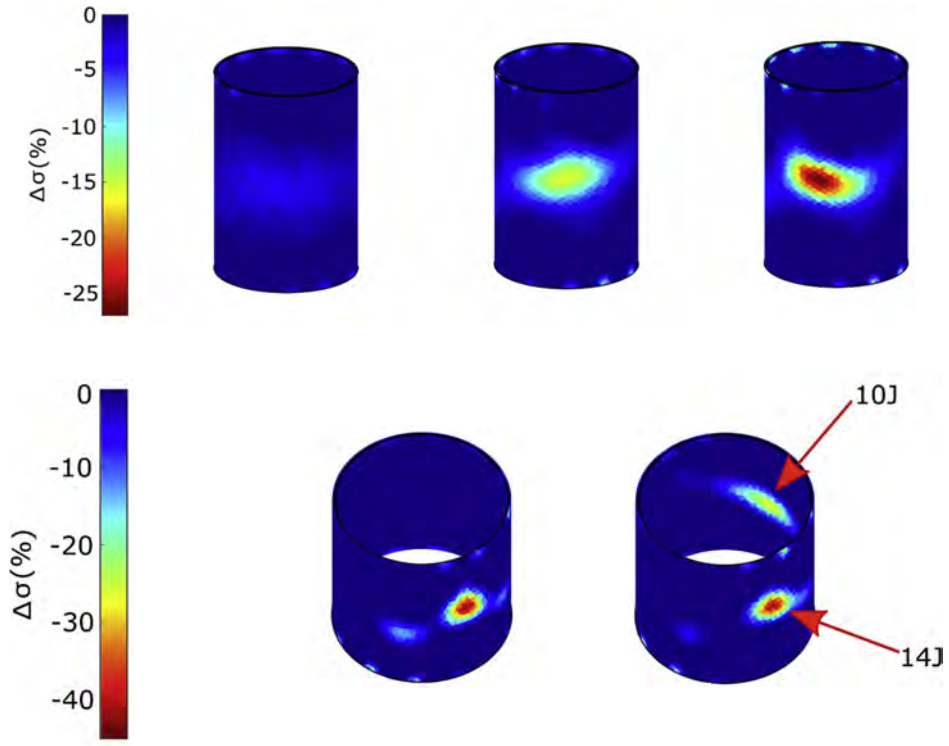

Figure 1.14. EIT used to detect through-hole and impact damage in self-sensing composite tubes [90]. Top left to right: EIT images for 4.76 mm, 7.94 mm, and 9.53 mm diameter holes. Bottom left: EIT image for 14 J impact. Bottom right: EIT image for 14 J and 10 J impacts.

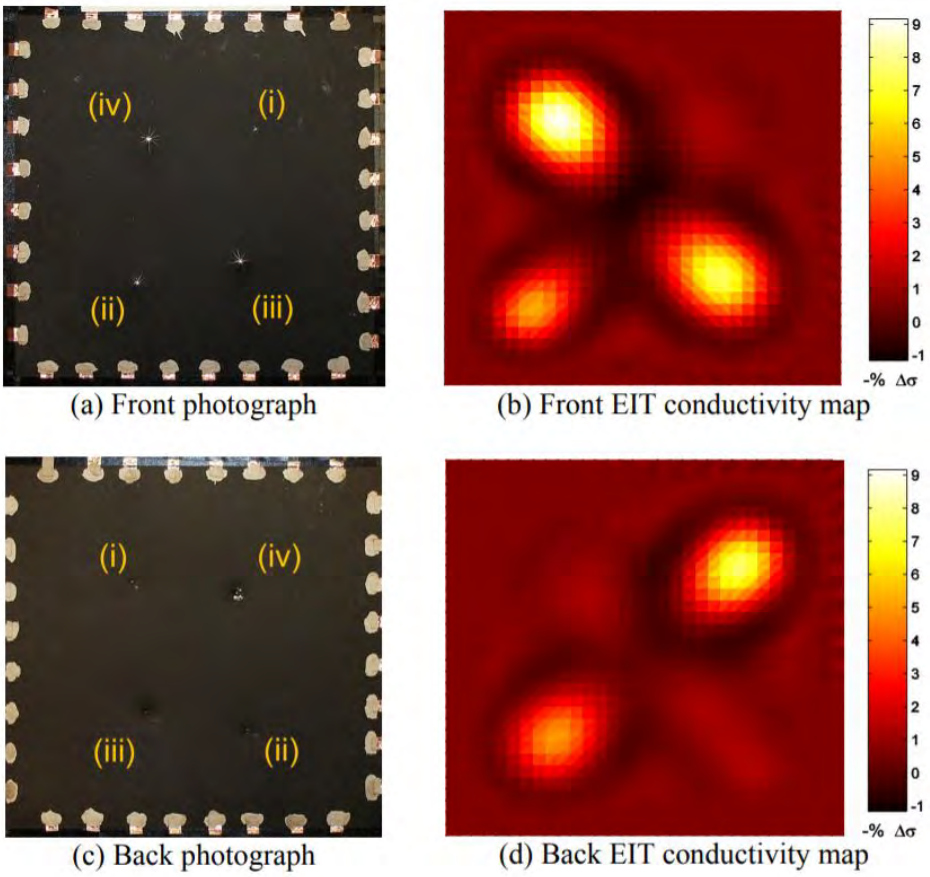

Figure 1.15. EIT used to detect impact damage in a CNT-based sensing skin [94]. Left column: Photos of the impacted sensing skin. Right column: EIT images of the front and back of the skin.

conductivity of the skin with an increase in the applied strain. Similarly, Loh et al. [94] developed a CNT-based sensing skin using LbL and used it to detect impact damage, shown in Figure 1.15, and corrosion damage in a metallic structure. Other forms of external sensing media include spray-on sensors for strain sensing [96], [97] and conductive paint-based sensors for detecting cracking and corrosion [98]–[101]. A major advantage of EIT is that it generally requires fewer electrodes than 2-D interpolated resistance change methods to produce good quality images. For example, Dai et al. [85] used a total of 32 electrodes to produce the EIT images shown in Figure 1.12 and Tallman et al. [86] used 16 electrodes to produce the EIT images shown in Figure 1.13.

2. PROBLEM STATEMENT, RESEARCH GOAL, THESIS CONTRIBUTIONS, AND THESIS ORGANIZATION

Based on the discussion in the previous chapter, two important observations can be made. First, self-sensing composites have incredible potential for SHM because they are piezoresistive. This means that changes in the mechanical state of the material, due to applied strains and damage, manifest as measurable changes in electrical conductivity. Second, EIT offers superior spatial imaging capabilities than interpolated resistance change methods and is therefore a viable modality for conductivity-based health monitoring. A critical gap in the current state-of-the-art can also be identified. Although EIT has been extensively used for SHM in self-sensing composites, its application has been mostly limited to damage detection. That is, most work has focused on imaging damage and strain-induced conductivity changes. So far there has been very little effort in determining precise mechanics from electrical measurements. This limitation exists for two major reasons. First, considerable research has explored the feasibility of conductivity-based health monitoring in various self-sensing materials. Consequently, resistance change methods and tomographic imaging techniques are well-established and have proven to be highly effective at detecting damage in a plethora of self-sensing material systems. And second, recovering precise mechanics from electrical measurements is an extremely challenging inverse problem. This is because the relation between mechanics quantities, such as strain and damage, and electrical measurements, such as resistance changes and conductivity, is generally not unique. This means, for example, that multiple strain states can give rise to the same observed conductivity change. Therefore, obtaining mechanics information from electrical measurements is an inverse problem with many possible solutions. Because of this, conventional optimization strategies such as gradient-based minimization schemes fail to produce physically meaningful solutions. Herein, we recognize this as a crucial limitation that must be addressed in order to transform conductivity-based SHM from mere damage detection to much more complete characterization of the mechanics and damage condition of the structure. In light of this, we can state the following problem statement, research goals, and contributions of this thesis work.

Problem Statement: Self-sensing piezoresistive composites can positively impact the safety of engineering structures. Coupling piezoresistivity with conductivity-based damage detection techniques can enable spatially continuous, real-time SHM. However, prevailing conductivity-based health monitoring provides little-to-no information about the underlying mechanics of the structure such as the displacements, strains, stresses, and damage mechanisms and shapes. This is a critical limitation because the underlying mechanics, and not the conductivity, are pertinent to the condition of the structure. For example, conductivity in itself cannot be used to prognosticate material failure. However, if the stress state in the material is known, failure can be immediately predicted.

Research Goal: In light of the preceding limitation, the primary goal of this research is to develop methods for recovering precise mechanics information from conductivity measurements in self-sensing composites.

Thesis Contributions: This thesis makes three important contributions toward the above research goal.

1. A new method for solving the piezoresistive inversion (conductivity-to-strain) problem in self-sensing composites is developed. This method integrates a genetic algorithm (GA) with an analytical piezoresistivity model to inversely compute the displacements, strains, and stresses using EIT-imaged conductivity changes. Experimental results are used to demonstrate that this method can be used to accurately predict structural failure in self-sensing composites.

2. Three prominent metaheuristic algorithms are compared for solving the piezoresistive inversion problem and the best algorithm is identified. GAs, simulated annealing (SA), and particle swarm optimization (PSO) are used to solve the piezoresistive inversion problem. The results from each algorithm are validated against numerical FE and experimental results and a comparison is drawn between the three algorithms in terms of solution quality, variability, accuracy, and computational efficiency.

3. A novel technique is developed for precisely determining the shape and size of specific damage modes in self-sensing composites using EIT-imaged conductivity changes and boundary voltages. This technique integrates a GA with physics-based models that

relate damage geometry to material conductivity. The accuracy and precision of this approach is validated experimentally on self-sensing composite laminates.

The organization of this thesis is as follows. The EIT forward and inverse problems are first mathematically formulated. Next, conductivity-to-mechanics inverse problems are discussed and solution strategies for these problems using metaheuristic algorithms are developed. Two specific problems are addressed: piezoresistive inversion (conductivity-to-strain) and precise damage shaping (conductivity-to-damage geometry). Self-sensing composites are then manufactured and experimentally tested in scenarios pertaining to each of these problems. The metaheuristic algorithm-enabled inversion results are then compared with experimental results and important insights are drawn. Finally, this thesis ends by summarizing the scholarly contributions, their broader impact for SHM, and recommendations for future work.

3. ELECTRICAL IMPEDANCE TOMOGRAPHY

This chapter presents the mathematical formulation of the EIT forward and inverse problems. As discussed earlier, EIT is a method of imaging the internal conductivity distribution of a domain using voltages measured at the domain boundary. EIT can be used to spatially image mechanically-induced conductivity changes in piezoresistive nanocomposites and therefore has much potential for self-sensing SHM. Additionally, EIT has broad appeal for imaging in biomedical [102], [103], robotics [104], geospatial applications [105] due to the fact that it is low cost, non-invasive, and can resolve conductivity changes in nearly real-time.

Mathematically, EIT works by minimizing the difference between a vector of experimentally measured boundary voltages and a vector of numerically computed boundary voltages. The experimental voltages are collected by first lining the periphery of the domain with electrodes. Next, current injections and voltage measurements are most often collected using one of two injection schemes (note, however, other more sophisticated injection schemes exist particularly in biomedical applications of EIT [106], [107]). In the 'across' injection scheme, current is injected between two opposing pairs of electrodes while voltage differences are measured between the remaining opposing pairs. The current injection is then moved to the next opposing electrode pair and voltage differences are again measured between the remaining opposing electrode pairs. This continues until all opposing electrode pairs have received a current injection and a vector of $(L/2)(L/2-1)$ voltage differences is obtained, where L is the total number of electrodes. The across injection scheme is illustrated schematically in Figure 3.1. This scheme is more practical for imaging cases where two opposite edges of the domain are not accessible and thus cannot be instrumented with electrodes. This scheme may also be advantageous for cases where the conductivity artifact is far from the edge of the domain because it forces the electrical current to interact with the artifact as it propagates across the domain [108].

For domains where all edges are accessible, the 'adjacent' injection scheme is often used. Current is injected between one pair of adjacent electrodes while voltage differences are measured between the remaining adjacent electrode pairs. The current injection is then moved to the next adjacent electrode pair and voltage differences are again measured between

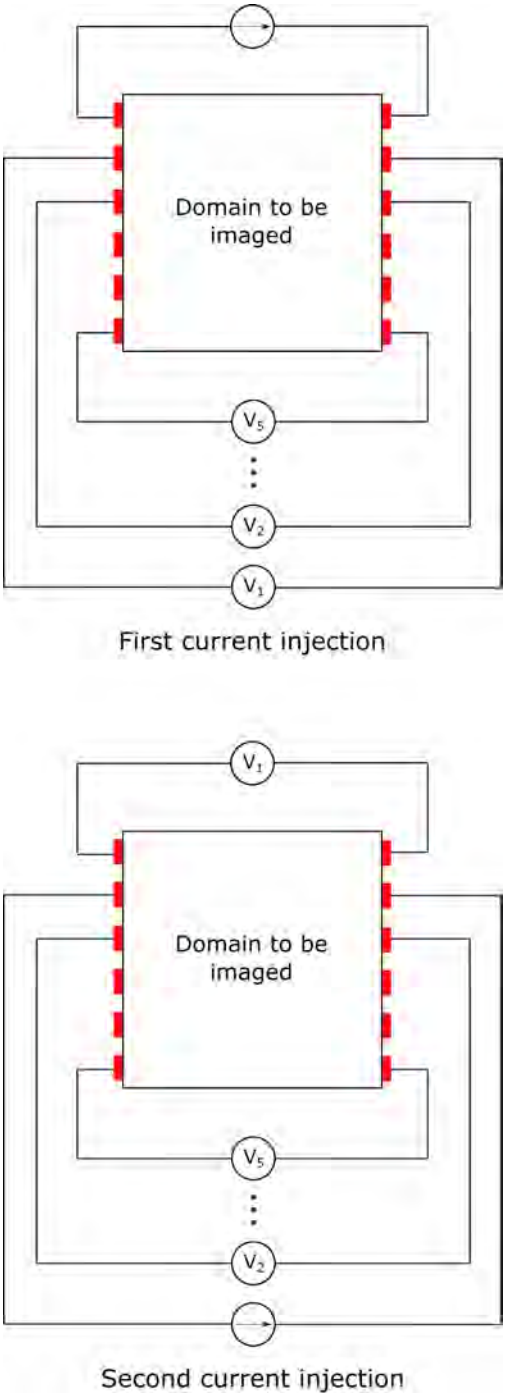

Figure 3.1. Illustration of first (top) and second (bottom) current injections for across injection scheme. Two opposite edges of the domain are lined with electrodes, indicated by the red rectangles. Current is injected between the first pair of opposing electrodes and voltages differences are measured between the remaining opposing electrode pairs. The current injection is then moved to the next opposing electrode pair and voltages differences are again measured.

the remaining adjacent electrode pairs. This process continues until all adjacent electrode pairs have received a current injection and a vector of $L(L-3)$ voltage differences is obtained. The adjacent injection scheme is illustrated schematically in Figure 3.2.

3.1 Forward Problem

The procedure of computing the numerical boundary voltages for a known domain conductivity is known as the EIT forward problem. Mathematical formulation of the forward problem begins with Laplace's equation for steady-state diffusion in the absence of internal current sources. This is shown in equation (3.1), where σ_{ij} is the domain conductivity and ϕ is the domain potential.

$$\frac{\partial}{\partial x_i}\sigma_{ij}\frac{\partial \phi}{\partial x_j} = 0 \tag{3.1}$$

Indicial notation is used here and repeated indices imply summation over the dimension of the problem. Summation is not implied for indices where electrodes are involved unless the summation operator is explicitly used. We then enforce two complete electrode model boundary conditions on equation (3.1). These are shown in equations (3.2) and (3.3). Equation (3.2) simulates contact impedance between the perfectly conducting domain and the electrodes and equation (3.3) enforces conservation of charge by requiring that the sum of the current through the electrodes is zero. In these equations, z_l is the contact impedance between the lth electrode and the domain, n_i is an outward pointing normal vector, E_l is the length of the lth electrode, and V_l is the voltage of the lth electrode.

$$\sigma_{ij}\frac{\partial \phi}{\partial x_i}n_j = \frac{1}{z_l}(V_l - \phi) \tag{3.2}$$

$$\sum_{l=1}^{L}\int_{E_l}\sigma_{ij}\frac{\partial \phi}{\partial x_i}n_j \,\mathrm{d}S_l = 0 \tag{3.3}$$

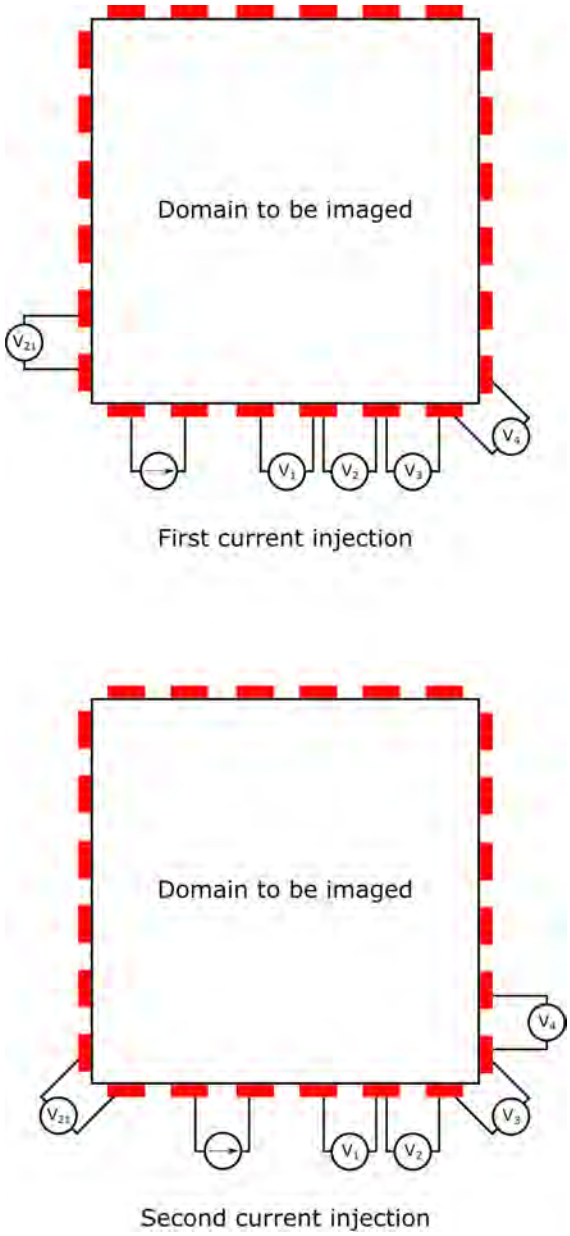

Figure 3.2. Illustration of first (top) and second (bottom) current injections for adjacent injection scheme. All edges of the domain are lined with electrodes. Current is injected between the first pair of adjacent electrodes and voltage differences are measured between the remaining adjacent electrode pairs. The current injection is then moved to the next adjacent electrode pair and voltages differences are again measured.

Equations (3.1) to (3.3) can be solved conveniently via the finite element (FE) method, as shown in equation (3.4). The individual matrices $\boldsymbol{A}_M$, $\boldsymbol{A}_Z$, $\boldsymbol{A}_W$, and $\boldsymbol{A}_D$ are formed as shown in equations (3.5) to (3.8).

$$\begin{bmatrix} \boldsymbol{A}_M + \boldsymbol{A}_Z & \boldsymbol{A}_W \\ \boldsymbol{A}_W^T & \boldsymbol{A}_D \end{bmatrix} \begin{bmatrix} \boldsymbol{\Phi} \\ \boldsymbol{V} \end{bmatrix} = \begin{bmatrix} \boldsymbol{0} \\ \boldsymbol{I} \end{bmatrix} \tag{3.4}$$

$$A^e_{M\ ij} = \int_{\Omega_e} \frac{\partial w_i}{\partial x_k} \sigma_{kl} \frac{\partial w_j}{\partial x_l}\, \mathrm{d}\Omega_e \tag{3.5}$$

$$A_{Z\ ij} = \sum_{l=1}^{L} \int_{E_l} \frac{1}{z_l} w_i w_j\, \mathrm{d}S_l \tag{3.6}$$

$$A_{W\ li} = -\int_{E_l} \frac{1}{z_l} w_i\, \mathrm{d}S_l \tag{3.7}$$

$$A_D = \mathrm{diag}\left(\frac{E_l}{z_l}\right) \tag{3.8}$$

In the preceding equations, $\boldsymbol{\Phi}$ is a vector of domain potentials, $\boldsymbol{V}$ is a vector of electrode voltages, and $\boldsymbol{I}$ is a vector of injected currents. The ith component of the jth column of the local diffusion stiffness matrix for the eth element is calculated as shown in equation (3.5), where w_i is the ith FE interpolation or basis function. In this work, linear interpolation functions are used by discretizing the domain using triangular elements in two dimensions and hexahedral elements in three dimensions. The local diffusion stiffness matrices are then assembled into the global stiffness matrix, $\boldsymbol{A}_M$. Equations (3.6) to (3.8) account for the additional degrees of freedom introduced due to the contact impedance of the electrodes. A detailed solution to these equations is presented in Appendix A.

3.2 Inverse Problem

The EIT inverse problem attempts to recover the conductivity distribution of the domain interior using the current-voltage behavior observed at the domain boundary. In this work, difference imaging via a one-step linearization scheme is used to solve the inverse problem.

Difference imaging is generally robust to experimental noise and modeling errors because it seeks the conductivity change (or difference) between two states. Therefore, measurement or modeling errors common to both states are cancelled out when differences are taken. Other commonly used inversion techniques include the Gauss-Newton iterative method [109], maximum a posteriori (MAP) estimates [110], and the primal dual interior point method (PDIPM) [111]. A comprehensive overview of these techniques can be found in reference [112].

Returning to the inverse problem, one set of boundary voltages is collected before the domain experiences damage or deformation and another set of boundary voltages is collected after the domain experiences damage or deformation. The goal of the one-step linearized inverse problem is to then find the conductivity change that minimizes the difference between the pre- and post-damage voltages. We begin by defining the vector $\delta \boldsymbol{V}$ as the difference between the post- and pre-damage voltages collected at times t_2 and t_1, respectively, as shown in equation (3.9).

$$\delta \boldsymbol{V} = \boldsymbol{V}(\sigma_2, t_2) - \boldsymbol{V}(\sigma_1, t_1) \tag{3.9}$$

We then define an equivalent numerically computed vector, $\boldsymbol{W}(\delta \boldsymbol{\sigma})$, as shown in equation (3.10). In this equation, $\boldsymbol{F}(\cdot)$ are the numerically computed voltages obtained by solving the forward problem at the conductivity in the argument, $\boldsymbol{\sigma}_0$ is the baseline or undamaged conductivity, and $\delta \boldsymbol{\sigma}$ is the conductivity change vector we seek. Quantities that have been discretized via finite elements have been boldfaced.

$$\boldsymbol{W}(\delta \boldsymbol{\sigma}) = \boldsymbol{F}(\boldsymbol{\sigma}_0 + \delta \boldsymbol{\sigma}) - \boldsymbol{F}(\boldsymbol{\sigma}_0) \tag{3.10}$$

We proceeed by linearizing the first term on the right hand side of equation (3.10) using a Taylor series expansion about $\boldsymbol{\sigma}_0$ and retaining only the linear terms, as shown in equation (3.11).

$$\boldsymbol{F}(\boldsymbol{\sigma}_0 + \delta \boldsymbol{\sigma}) \approx \boldsymbol{F}(\boldsymbol{\sigma}_0) + \frac{\partial \boldsymbol{F}(\boldsymbol{\sigma}_0)}{\partial \boldsymbol{\sigma}} \delta \boldsymbol{\sigma} \tag{3.11}$$

Substituting equation (3.11) into equation (3.10) and defining $\boldsymbol{J} = \partial \boldsymbol{F}(\boldsymbol{\sigma}_0)/\partial \boldsymbol{\sigma}$ as the sensitivity matrix yields equation (3.12).

$$\boldsymbol{W}(\delta\boldsymbol{\sigma}) \approx \boldsymbol{J}\delta\boldsymbol{\sigma} \tag{3.12}$$

We then seek the conductivity change vector, $\delta\boldsymbol{\sigma}^*$, that minimizes the difference between $\boldsymbol{W}(\delta\boldsymbol{\sigma})$ and $\delta\boldsymbol{V}$. However, $\boldsymbol{J}$ cannot be directly inverted because it is severely rank-deficient. As such, the inverse problem is ill-posed and Tikhonov regularization is necessary to obtain a physically meaningful solution. The regularized inverse problem is shown in equation (3.13). Here, $\boldsymbol{L}$ is the regularization term and its contribution is controlled by the scalar parameter α. Note that equation (3.13) minimizes the l_2-norm for both the error and the regularization terms in the least-square sense. In this thesis, the discrete Laplace operator is used as the regularization term. Other choices for the error and regularization norms have been explored in literature [113], such as the l_1-norm and total variation (TV) regularization. However, the l_2-norm is very common in SHM [50], [85], [86] because it has a smoothing effect on large variations in conductivity. The explicit solution for $\delta\boldsymbol{\sigma}$ is shown in equation (3.14). In this thesis, a modified form of equation (3.14) is used. This form, shown in equation (3.15), incorporates constraints on $\delta\boldsymbol{\sigma}$ based on *a priori* knowledge of the expected conductivity change. Equation (3.15) will be specialized to specific EIT problems in a later chapter of this thesis.

$$\delta\boldsymbol{\sigma}^* = \min_{\delta\boldsymbol{\sigma}} \left(||\delta\boldsymbol{V} - \boldsymbol{J}\delta\boldsymbol{\sigma}||_2^2 + \alpha||\boldsymbol{L}\delta\boldsymbol{\sigma}||_2^2 \right) \tag{3.13}$$

$$\delta\boldsymbol{\sigma}^* = (\boldsymbol{J}^T\boldsymbol{J} + \alpha^2\boldsymbol{L}^T\boldsymbol{L})^{-1}\boldsymbol{J}^T\delta\boldsymbol{V} \tag{3.14}$$

$$\delta\boldsymbol{\sigma}^* = \min_{\delta\boldsymbol{\sigma}_{\min} \leq \delta\boldsymbol{\sigma} \leq \delta\boldsymbol{\sigma}_{\max}} \frac{1}{2} \left(\left|\left| \begin{bmatrix} \boldsymbol{J} \\ \alpha\boldsymbol{L} \end{bmatrix} \delta\boldsymbol{\sigma} - \begin{bmatrix} \delta\boldsymbol{V} \\ \boldsymbol{0} \end{bmatrix} \right|\right|_2^2 \right) \tag{3.15}$$

$$\boldsymbol{L} = L_{ij} = \begin{cases} \text{degree}(\Omega_i) & \text{if } i = j \\ -1 & \text{if } i \neq j \text{ and } \Omega_i \text{ is adjacent to } \Omega_j \\ 0 & \text{otherwise} \end{cases} \tag{3.16}$$

The discrete Laplace operator is formed as shown in equation (3.16). $\boldsymbol{L} = L_{ij}$ is a square matrix with a dimension equal to the number of elements in the FE mesh. The ith element in the diagonal is equal to the number of elements that share an edge in two dimensions and a surface in three dimensions with the ith element. If the ith and jth elements share an edge in two dimensions or a surface in three dimensions, $L_{ij} = L_{ji} = -1$. All other components of $\boldsymbol{L}$ are zero.

Going back to equation (3.12), the sensitivity matrix, $\boldsymbol{J}$, is formed by relating perturbations in the electrode voltages to perturbations in the domain conductivity. The final result is shown in equation (3.17). A closed form derivation of equation (3.17) can be found in Holder [114].

$$J_{MNe} = -\int_{\Omega_e} \frac{\partial \phi^M}{\partial x_i} \sigma_{ij} \frac{\partial \overline{\phi}^N}{\partial x_i} \, \mathrm{d}\Omega_e \tag{3.17}$$

In the above equation, MN represents a single index of $\boldsymbol{J}$ and is computed as the integral of the contraction of the gradient of the voltage on the eth element due to the current supplied by the Mth electrode injection pair and the gradient of the voltage on the eth element due to the Nth adjoint field [115]. The adjoint field is the domain solution for a unit current injection supplied to the Nth electrode injection pair. Physically, this can be thought of as the sensitivity of the Nth electrode measurement pair to a conductivity perturbation in the eth element when current is supplied by the Mth electrode pair. Detailed sensitivity matrix calculations are given in Appendix B.

3.3 Summary

This chapter presented the mathematical formulation of the EIT forward and inverse problems. Briefly, the forward problem solves for the boundary voltages for a specified

interior conductivity while the inverse problem attempts to recover the interior conductivity for a known set of boundary voltages. EIT will be used multiple times in this thesis to image strain- and damage-induced conductivity changes in self-sensing composites. Compared to 1-D and 2-D resistance change methods, EIT offers superior shaping capabilities with fewer electrodes. This makes it an attractive modality for spatially-continuous SHM in self-sensing structures.

4. CONDUCTIVITY-TO-MECHANICS INVERSE PROBLEMS

4.1 Introduction

Although EIT affords better spatial localization than interpolated resistance change methods, its imaging capabilities are still somewhat indistinct. This can be observed from Figures 1.13 to 1.15, where the edges of the damage-induced conductivity artifacts are not sharply defined. This is due to the fact that the EIT inverse problem is ill-posed and thus requires regularization to obtain a physically meaningful solution. This leads to a smearing effect in the reconstructed conductivity change distribution. The lack of sharply defined features is viewed as a limitation and as such, there has been considerable work on improving the spatial resolution of EIT.

One simple method to improve resolution is to use a large number of electrodes to make the problem less ill-posed. However, this is not always practical for SHM since all edges of a structure may not be fully accessible for instrumentation. In an effort to circumvent the need for a large number of electrodes for good resolution, Hassan et al. [116] showed via numerical simulations that the spatial resolution of EIT can be significantly improved by incorporating non-local conductivity changes via piezoresistivity. This approach was shown to produce good quality images but was not experimentally validated. Other work has explored different types of norms for solving the inverse problem [113], shape driven difference imaging [117], B-splines [118], moving morphable components (MCCs) [119], and relaxed regularization [120] for extracting sharp features from EIT images. These approaches, while undoubtedly powerful, are of limited direct benefit to SHM because they do not model the underlying mechanics of the structure. Instead, they focus on reconstructing conductivity based on parameterized geometric shapes or *a priori* knowledge of the conductivity change. From a SHM point of view, conductivity is not a structurally-relevant property. It would be much more beneficial to know the underlying displacements, strains, stresses, and damage sizes and mechanisms in a structure rather than the size of a conductivity artifact. This leads to a class of problems known as conductivity-to-mechanics inverse problems, where the goal is to recover the precise underlying mechanical state of a structure from observed conductivity changes.

4.2 Metaheuristic Algorithms

Conductivity-to-mechanics inverse problems are challenging to solve because the mathematical relation between mechanics quantities, such as strain and damage, and conductivity change is generally not one-to-one. This means that multiple mechanical states can cause the same conductivity change. Furthermore, mechanics quantities such as displacement and strain can have multiple components. Consequently, recovering mechanics from observed conductivity changes is an under-determined inverse problem with several mathematically feasible solutions. From a mechanics point of view, however, there can only be one feasible solution (a linear elastic structure can only have one strain state, for example). In order to surmount these problems, it is necessary to pose conductivity-to-mechanics inverse problems as constrained l_n-norm minimization problems of the form shown in equation (4.1).

$$x^* = \underset{x_{\min} \leq x \leq x_{\max}}{\arg\min} \; (||y - M(x)||_n) \tag{4.1}$$

In the above equation, y is an experimentally observed quantity, $M(\cdot)$ is a mechanics-based model, and x is a quantity that represents the mechanical state. An optimization strategy can then be used to obtain a solution to equation (4.1). However, it is well known that gradient-based optimization only leads to locally optimum solutions depending on the initial estimate. A locally optimum solution may not be mechanically feasible. This is illustrated qualitatively in Figure 4.1, where the function $f(x) = ||y - M(x)||_n$ has several locally optimum solutions but only one of these solutions is physically admissible. Therefore, in order to find the only physically admissible solution, any optimization strategy for conductivity-to-mechanics inverse problems requires two key components. First, a metaheuristic global search algorithm is needed so that all possible solutions are tested to find those that satisfy the minimization. In this work, three different metaheuristic algorithms are used: genetic algorithms (GAs), simulated annealing (SA), and particle swarm optimization (PSO). It is important to note that the goal of this thesis is not to develop new metaheuristic algorithms but to use existing algorithms to solve challenging conductivity-to-mechanics inverse problems. The three aforementioned algorithms were chosen because

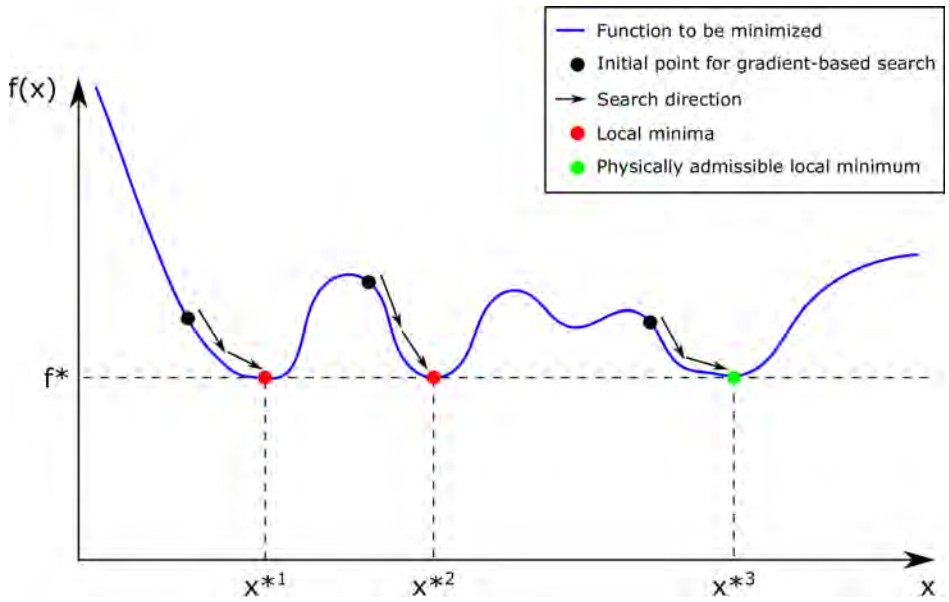

Figure 4.1. Qualitative illustration of multi-modality. The function $f(x) = ||y - M(x)||_n$ has several minimizing solutions. However, only one solution (x^{*3}) is physically admissible. Gradient-based optimization schemes only lead to the local minimum solution closest to the initial estimate.

they are well-established and widely used to solve global optimization problems. Below, a brief overview of each of these metaheuristic algorithms is given.

GAs [121], [122] are a family of global search algorithms inspired by natural evolution. GAs work by initializing a population of candidate solutions dispersed inside a pre-defined search space. Each candidate has a numerically defined chromosome and gene. The function to be minimized, known as the fitness function, is evaluated for each candidate. The population then evolves and the candidates compete in order to determine which genes will be passed on to the next generation. Candidates that result in a lower fitness function value have a higher probability of passing their genes. Additionally, cross-over and mutation take place to ensure some genetic diversity in the population. This evolutionary process, which is analogous to natural selection, continues until a certain level of genetic similarity is achieved in the population. The degree of genetic similarity in the population is quantified via the bit-string affinity (BSA). Figure 4.2 shows a flowchart for a typical GA. In this thesis, a GA originally developed by W. A. Crossley and used successfully by Raghavan et al. [123] for nondestructive testing of jet engine turbine blades is used.

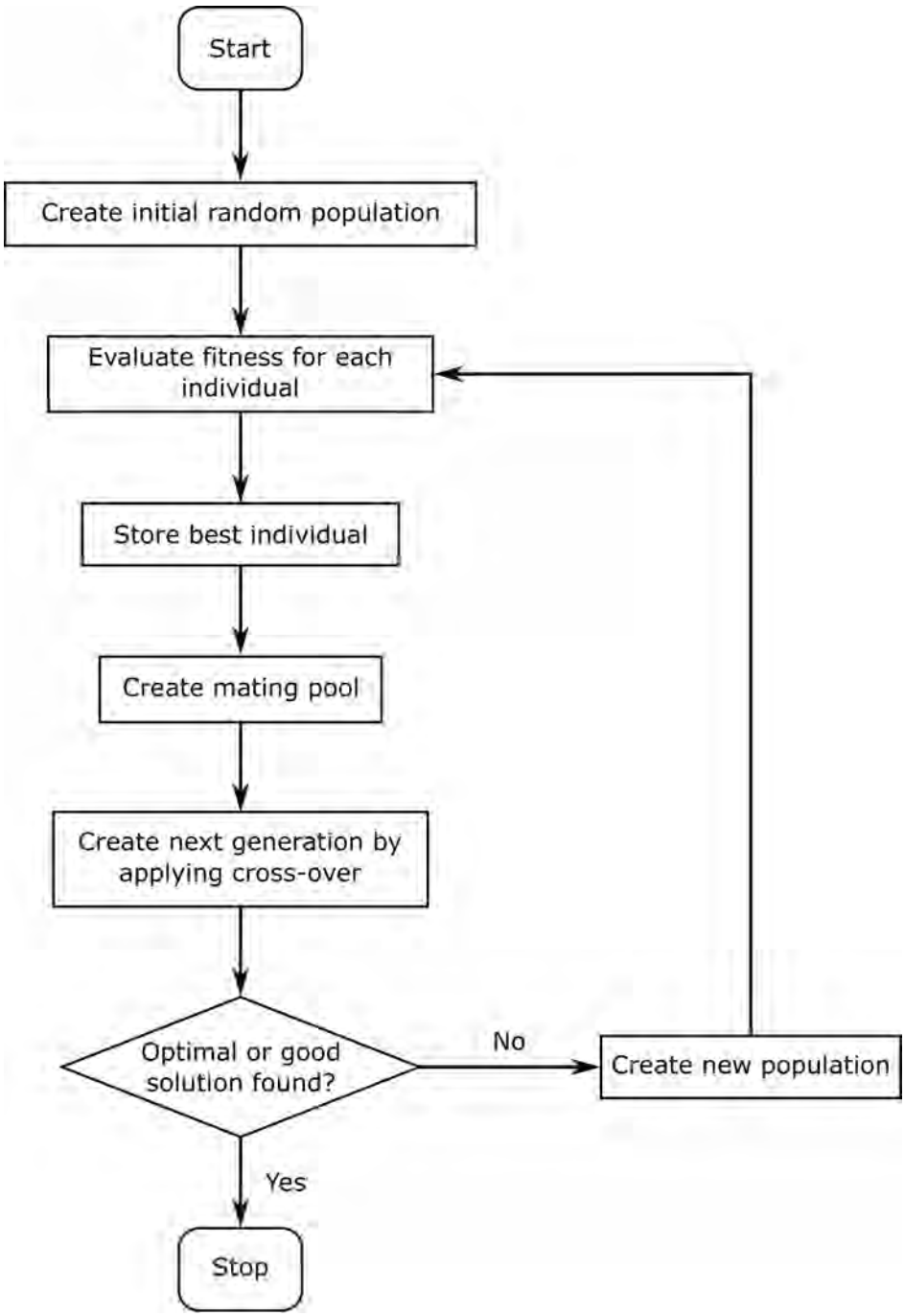

Figure 4.2. Flowchart for a general GA adapted from Sivanandam and Deepa [124].

SA [125] is a type of metaheuristic algorithm inspired by the metallurgical process of annealing, where a metal is heated to a high temperature and then allowed to cool down slowly so that the atoms attain a minimum energy configuration. Very simply, the SA algorithm generates a new candidate solution, analogous to the heated state of the metal, based on a virtual annealing temperature. If the new state is an improvement over the initial state (based on the fitness function value), then the candidate is accepted. If, however, the candidate is not an improvement over the initial state then it is only accepted with a probability based on the Metropolis criterion [126]. This allows the SA algorithm to 'explore' the search space much more than traditional hill-climbing algorithms that only accept solutions which improve the state of the system and are therefore more likely to find locally optimum solutions. This probabilistic procedure of selecting candidates continues until convergence is satisfied. Figure 4.3 shows a flowchart for a general SA algorithm. In this work, a MATLAB-based SA algorithm based on the work Ingber [127] is used.

Lastly, PSO is an evolutionary algorithm inspired by the behavior of groups of social organisms such as a flock of birds or a school of fish. The PSO algorithm generates a population or 'swarm' of solutions, individually known as 'particles', inside a pre-specified search space. Each particle has a certain position and velocity. However, the particles do not move independent from each other. Rather, the trajectory of each particle is guided by the 'best' position and velocity of the collective swarm and also the best position and velocity of each particle. In this manner, the particles share information and the swarm moves around the search space until convergence is achieved. A schematic showing the movement of particles in a typical PSO algorithm is shown in Figure 4.4. In this thesis, a MATLAB-based PSO algorithm based on the works of Kennedy and Eberhart [129], Mezura-Montes and Coello [130], and Pedersen [131] is used.

The second component of a solution strategy for conductivity-to-mechanics inverse problems are physics-based models that relate the mechanical state (displacements, strains, stresses, and damage) to conductivity changes. These are essential to ensure that only physically admissible solutions are selected. In the forthcoming sections, specialized models are discussed in detail for solving two important problems: piezoresistive inversion, where

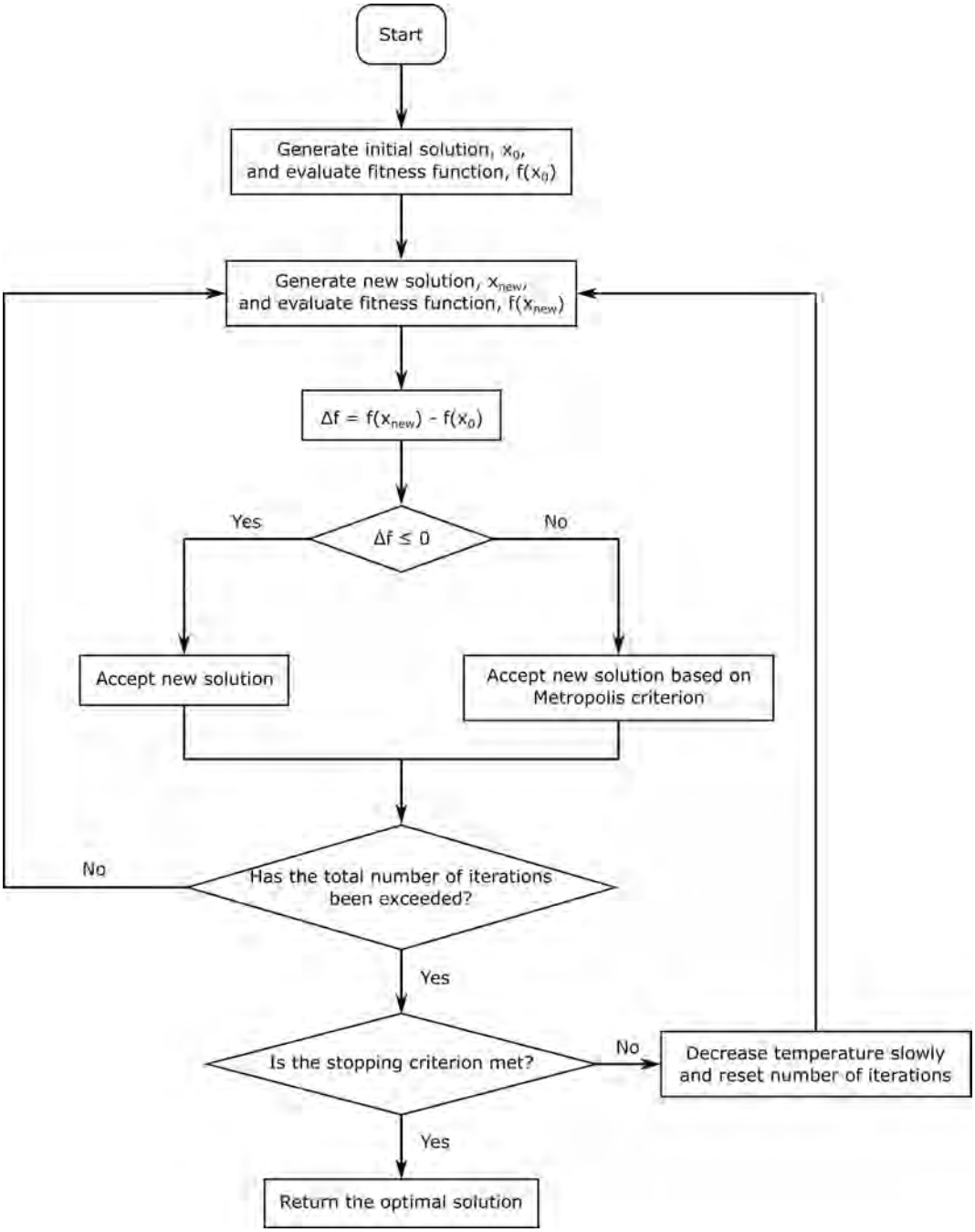

Figure 4.3. Flowchart for a general SA algorithm adapted from Yao et al [128].

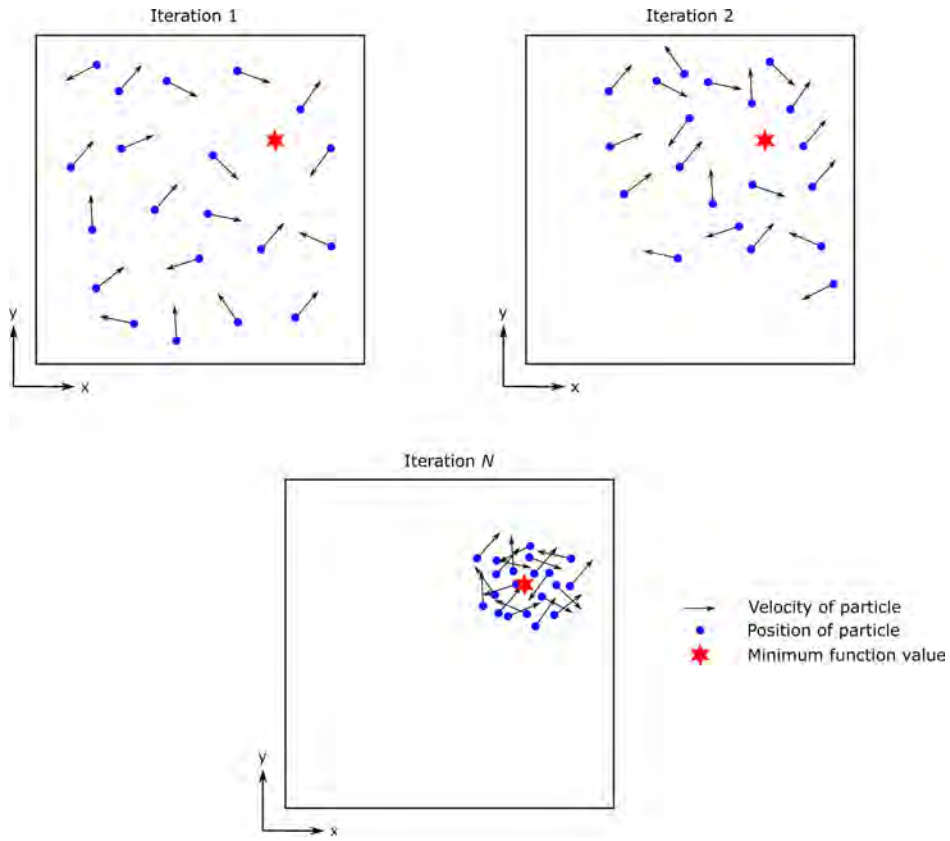

Figure 4.4. Schematic showing the movement of particles during a typical PSO search. The trajectory of each particle is described by its position and velocity. In iteration 1, the particles are randomly dispersed with different positions and velocities. As the number of iterations increases, the particles begin to move toward the minimum function value. Convergence is satisfied when the change in the particle positions and velocities becomes very small, indicating that the minimum function value has been attained.

the goal is to recover strains from conductivity changes, and precise damage shaping, where the goal is to recover precise damage geometry from conductivity changes.

4.3 Piezoresistive Inversion

The goal of piezoresistive inversion is to recover the underlying strain state giving rise to an observed conductivity distribution in a piezoresistive self-sensing composite. This problem was first explored computationally by Tallman and Wang [132] and later experimentally by Tallman et al [133]. The piezoresistive inversion problem is inherently under-determined because conductivity is generally treated as a single-valued scalar while strain has six independent components. The original approach developed by Tallman and Wang [132] used gradient-based optimization via a Gauss-Newton iterative algorithm to find the strain state that minimized the difference between an observed conductivity and a conductivity predicted analytically. In the work of Tallman et al. [133], the observed conductivity was obtained via EIT and the analytical conductivity was predicted using a piezoresistivity model. Although this approach was highly effective and computationally efficient at determining the strain state, the use of gradient-based optimization implies that it can only be used in certain limited scenarios where the actual solution is relatively 'close' to the initial estimate. To extend this approach to more general loading scenarios, in this thesis the piezoresistive inversion problem is solved using metaheuristic algorithms. First, however, it is vital to establish a model that accurately captures the relation between strain and conductivity in piezoresistive materials.

4.3.1 Analytical Piezoresistivity Model

The phenomenon of piezoresistivity in self-sensing materials has been widely studied [134] and several types of models have been developed to describe the relationship between conductivity and deformation. These include equivalent resistor network-based models [135], [136], computational micromechanics-based models [137], [138], and tensor-based resistivity-strain relations [44], [139]. Herein, we will use an analytical piezoresistivity model developed by Tallman and Wang [140] and based on a nanocomposite conductivity model proposed by

Takeda et al [141]. According to Tallman and Wang [140], the conductivity of a nanocomposite can be calculated according to the following equation.

$$\sigma_p = \sigma_m + \frac{4Pvl_f}{3\pi\lambda^2 d_f^2 \left[\frac{4l_f}{\pi d_f^2 \sigma_f} + \frac{h^2 t}{Ae^2\sqrt{2m\phi}}\exp\left(\frac{4\pi t}{h}\sqrt{2m\varphi}\right)\right]} \tag{4.2}$$

In the above equation, σ_p is the nanocomposite conductivity, σ_m is the matrix conductivity, σ_f is the conductivity of an individual nanofiller, P is the percolation probability given by $P = K(v - v_c)^{\psi}$, v is the nanofiller volume fraction, v_c is the critical nanofiller volume fraction, l_f is the length of a single nanofiller, d_f is the nanofiller diameter, λ is the nanofiller waviness ratio, A is the overlapping nanofiller area, t is the average inter-filler spacing given by $t = \alpha(v - v_c)^{\beta}$, h is Planck's constant, e is the elementary charge of a single electron, and ϕ is the potential barrier height felt by tunneling electrons. Tallman and Wang [140] expressed v as a function of the infinitesimal strain tensor, ε_{ij}. Therefore, P and t can also be expressed as functions of ε_{ij} and the conductivity of a nanocomposite can be calculated for an arbitrary strain state. This formulation was then integrated with the FE method to make the model amenable to multi-scale analysis. Tallman and Wang [132] later updated this model with a sigmoidal relation for t to allow for differentiability. Equation (4.2) can be used to predict the conductivity of any nanofiller-modified polymer by adjusting the values of α and β in the expression for the average inter-filler spacing for a state of zero strain.

4.3.2 Metaheuristic Algorithm-Enabled Conductivity-to-Strain Problem

The piezoresistive inversion problem, as formulated by Tallman and Wang [132], seeks the strain state that minimizes the difference between an experimentally observed conductivity and a conductivity predicted analytically. This can be cast as the following l_n-norm minimization problem.

$$\varepsilon_{ij}^* = \arg\min_{\varepsilon_{ij}}(||\sigma_e - \sigma_p(\varepsilon_{ij})||_n) \tag{4.3}$$

In the above equation, ε_{ij}^* is the strain state we seek, σ_e is an experimentally observed conductivity, and $\sigma_p(\varepsilon_{ij})$ is a conductivity predicted using a piezoresistivity model evaluated

for the strain state in the argument. In this thesis, σ_e will be imaged via EIT and since EIT is performed on a FE mesh, σ_e is a vector quantity due to discretization. Therefore, the experimentally observed conductivity can be written as the boldfaced vector quantity $\boldsymbol{\sigma}_e$. Furthermore, since infinitesimal strain can be written as the gradient of the displacement, the analytically predicted conductivity can be expressed as a function of the global displacement vector, $\boldsymbol{d}$. Equation (4.3) can then be restated as follows.

$$\boldsymbol{d}^* = \arg\min_{\boldsymbol{d}}(||\boldsymbol{\sigma}_e - \boldsymbol{\sigma}_p(\boldsymbol{d})||_n) \tag{4.4}$$

The goal of equation (4.4) is to recover the global displacement vector, $\boldsymbol{d}^*$, rather than strains. Tallman and Wang [132] used $n = 2$ in equation (4.4) to ensure differentiability with respect to strain for gradient-based optimization. In order to integrate this problem with a metaheuristic algorithm, equation (4.4) can be rewritten as equation (4.5), shown below.

$$\boldsymbol{d}_m^* = \arg\min_{\boldsymbol{d}_m}(||\boldsymbol{\sigma}_e - \boldsymbol{\sigma}_p(\boldsymbol{d}_m)||_n) \tag{4.5}$$

In equation (4.5), $\boldsymbol{d}_m$ is a global displacement vector generated using a metaheuristic algorithm and $\boldsymbol{\sigma}_p(\boldsymbol{d}_m)$ is a conductivity predicted analytically using the metaheuristic algorithm generated displacement vector. Since metaheuristic algorithms do not compute gradients, we will use $n = 1$ in equation (4.5). Also, the l_1-norm is generally less sensitive to outlier experimental data, which is not uncommon in EIT. Next, in light of the EIT one-step linearization scheme, we can express the predicted conductivity as $\boldsymbol{\sigma}_p(\boldsymbol{d}_m) = \delta\boldsymbol{\sigma}_p(\boldsymbol{d}_m) + \boldsymbol{\sigma}_0$ and the experimental conductivity as $\boldsymbol{\sigma}_e = \delta\boldsymbol{\sigma}_e + \boldsymbol{\sigma}_0$, where $\boldsymbol{\sigma}_0$ is the baseline or undeformed conductivity. Substituting these expressions into equation (4.5) gives equation (4.6).

$$\boldsymbol{d}_m^* = \arg\min_{\boldsymbol{d}_m}(||\delta\boldsymbol{\sigma}_e - \delta\boldsymbol{\sigma}_p(\boldsymbol{d}_m)||_1) \tag{4.6}$$

The goal of the preceding equation is to find the displacement vector, $\boldsymbol{d}^*$, that minimizes the difference between an experimentally observed conductivity change, $\delta\boldsymbol{\sigma}_e$, and a conductivity change predicted analytically using a metaheuristic algorithm, $\delta\boldsymbol{\sigma}_p(\boldsymbol{d}_m)$. However, metaheuristic algorithms cannot be used to directly produce displacement fields because they

are ignorant of mechanics principles such as equilibrium and strain compatibility. Instead, the global displacement field must be computed using a mechanics-based approach to ensure equilibrium and compatibility, and the metaheuristic algorithm generated displacement, $\boldsymbol{d}_m$, must be a subset of the global displacement. This is achieved by formulating a boundary value problem (BVP). The boundary conditions of the BVP are based on what is known about the loading and geometry of the structure. The boundary conditions can then be classified as either 'known' or 'unknown' and can be either Dirichlet or Neumann. However, at least one Dirichlet boundary condition must be specified for a physically meaningful solution. The metaheurstic algorithm then searches for the unknown boundary conditions and for each candidate boundary condition generated, linear elastic FEM is used to solve the associated BVP for the global displacement field. This is illustrated schematically in Figure 4.5. The global displacement field is then used to calculate strains and the conductivity, $\boldsymbol{\sigma}_p(\boldsymbol{d}_m)$, is calculated using equation (4.2). The fitness function is calculated according to equation (4.7).

$$f = ||\delta\boldsymbol{\sigma}_e - \delta\boldsymbol{\sigma}_p(\boldsymbol{d}_m)||_1 \tag{4.7}$$

$$|f_n^* - f_{n+1}^*| \leq 1 \times 10^{-3} \tag{4.8}$$

The algorithm continues to generate candidate boundary conditions until convergence is satisfied. The convergence criterion is dependent on the type of algorithm being used. Once convergence is satisfied, the search stops, the search space is reduced based on the minimum and maximum values of $\boldsymbol{d}_m^*$, and a new search initiates inside the updated search space. This process repeats until the convergence criterion shown in equation (4.8) is satisfied, where f_n^* is the minimum fitness function value obtained after the nth search. The displacements obtained at this point are treated as the final converged solution. At this point, having integrated a metaheuristic algorithm with realistic mechanics (an analytical piezoresistivity model and linear elastic FEM), the solution strategy for piezoresistive inversion is complete. In a later chapter of this thesis, this approach will be experimentally validated.

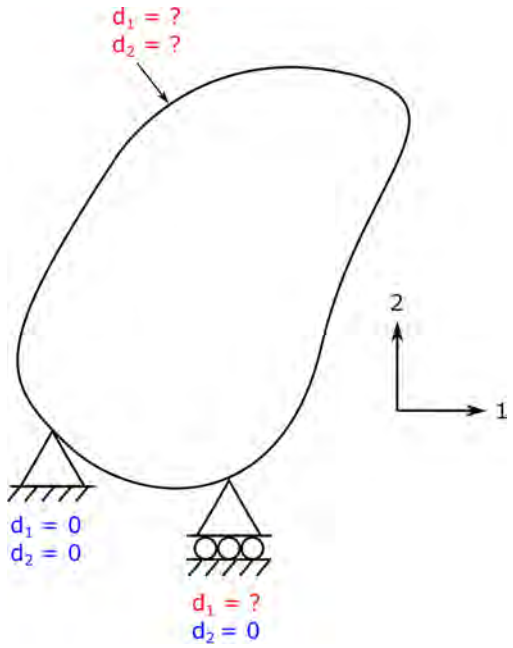

Figure 4.5. Representative boundary value problem (BVP) for piezoresistive inversion. The structure has known (blue) and unknown (red) displacement boundary conditions. The metaheuristic algorithm generates candidates for the unknown boundary conditions and linear elastic FEM is used to solve the BVP to obtain the global displacement field. In this case, all boundary conditions are of the Dirichlet type.

4.4 Precise Damage Shaping

The goal of the precise damage shaping problem is to recover the geometry and location of specific damage modes from EIT-imaged conductivity changes. However, there are no well-defined mathematical relationships between damage shape and material conductivity. This makes damage shaping a multi-modal inverse problem. As such, gradient-based optimization schemes cannot generally be implemented. Instead, similar to piezoresistive inversion, two key components are needed for a solution strategy. First, physics-based models are needed to realistically describe how specific damage modes affect material conductivity. And second, metaheuristic algorithms are needed to search for all physically viable solutions. In the forthcoming sections, geometric models for two specific damage modes —through-holes and delaminations —are developed and the mathematical formulation of the precise damage shaping problem is then integrated with these damage models and metaheuristic algorithms.

4.4.1 Geometric Models for Damage Mechanisms

Two parametric representations of damage geometry are developed in this thesis. First, consider the case of a through hole, which is a circular cavity in the domain where no conductive material is present. Through holes are commonly used for benchmarking damage detection capabilities and are likewise used herein. The geometry of a circular through hole can be described using the parametric representation $s = [x_c, y_c, r]$, where x_c and y_c are the x- and y- coordinates, respectively, of the center of the hole and r is the radius. The region inside the hole has zero conductivity while the undamaged domain has a conductivity equal to the undamaged baseline conductivity. This is illustrated schematically in Figure 4.6.

Next, consider a delamination, which is a separation of the layers of a laminate. The conductivity in the separated region is approximately zero since little or no conductive material is present here. For the simple case of a laminate consisting of only two layers, this can be modeled as a thin 'interface' region of approximately zero conductivity sandwiched between the two undamaged layers. Although a delamination can be arbitrarily shaped, in this thesis delaminations will be modeled as ellipses. This is not an unrealistic assumption since delaminations have been modeled as ellipses in prior work on failure of composite structures

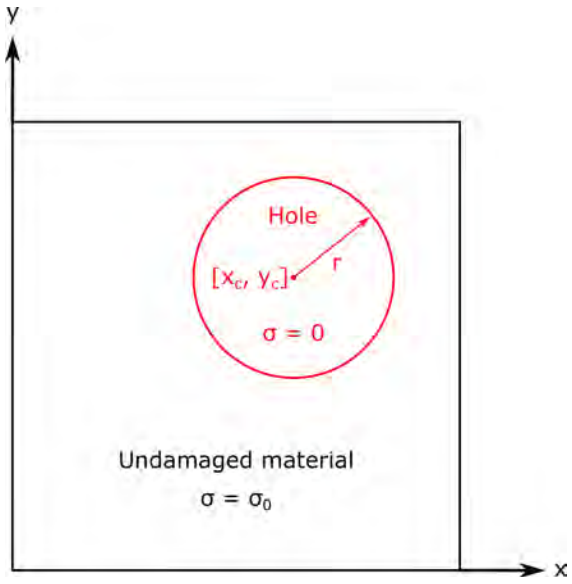

Figure 4.6. Geometric model for a through-hole. The red circle indicates a through-hole and the black rectangle is the domain. The size and location of the hole can be described using the x- and y-coordinates of the center of the hole and the radius of the hole. The interior of the hole has a conductivity of $\sigma = 0$ while the undamaged region has a conductivity equal to the baseline conductivity, σ_0.

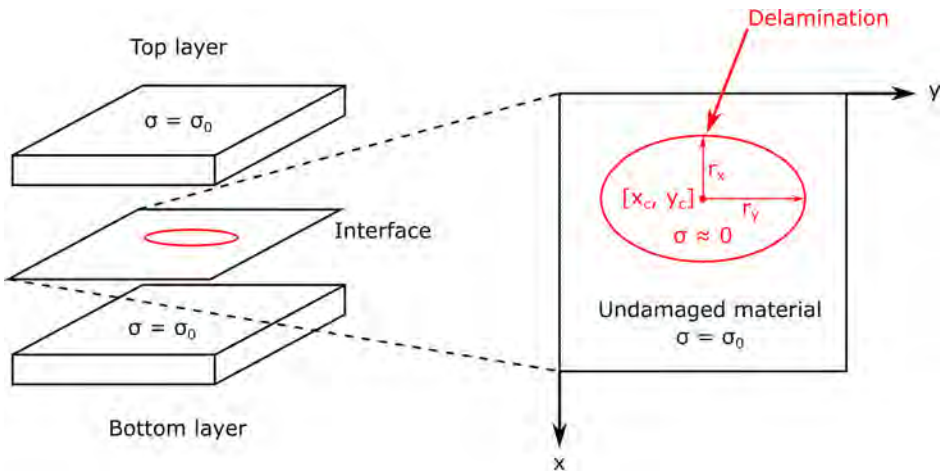

Figure 4.7. Geometric model for a delamination. The laminate shown consists of a thin 'interface' layer sandwiched between two undamaged layers. The interface layer consists of an elliptical delamination (shown in red) with a conductivity of approximately zero. The undamaged region in the top, bottom, and interface layers has a conductivity equal to the undamaged baseline conductivity of the material.

[142]–[145]. The geometry of an ellipse can be described using the parametric representation $s = [x_c, y_c, r_x, r_y]$, where x_c and y_c are the x- and y-coordinates, respectively, of the center of the ellipse and r_x and r_y are the radii along the x- and y-axes, respectively. This model is illustrated schematically in Figure 4.7.

4.4.2 Metaheuristic Algorithm-Enabled Conductivity-to-Damage Geometry Problem

Going back to the damage shaping problem, the goal is to recover the geometry of a specific damage mode from observed conductivity changes. In order to integrate this problem with a metaheuristic algorithm, the vector $\delta\boldsymbol{F}(s_m)$ is defined as shown in equation (4.9).

$$\delta\boldsymbol{F}(s_m) = \boldsymbol{F}(\boldsymbol{\sigma}(s_m)) - \boldsymbol{F}(\boldsymbol{\sigma}_0) \tag{4.9}$$

In the above equation, $\boldsymbol{F}(\boldsymbol{\sigma}(s_m))$ are the voltages predicted by solving the EIT forward problem on a domain containing damage described by the metaheuristic algorithm-predicted geometry, s_m. The goal of the precise damage shaping problem then is to find the optimum

damage geometry, s_m^*, that minimizes the l_1-norm of the difference between $\delta \boldsymbol{F}(s_m)$, given by equation (4.9), and $\delta \boldsymbol{V}$, given by equation (3.9). This can be stated as the optimization problem shown in equation (4.10).

$$s_m^* = \underset{s_m^{\min} \leq s_m \leq s_m^{\max}}{\arg\min} \left(|\delta \boldsymbol{V} - \delta \boldsymbol{F}(s_m)|_1 \right) \tag{4.10}$$

$$f = |\delta \boldsymbol{V} - \delta \boldsymbol{F}(s_m)|_1 \tag{4.11}$$

$$|f_n^* - f_{n+1}^*| \leq 1 \times 10^{-3} \tag{4.12}$$

The fitness function, f, is calculated according to equation (4.11). During a single search, the metaheuristic algorithm generates candidate solutions for s_m within the bounds $s_m^{\min}$ and $s_m^{\max}$ to minimize f. The search stops when a pre-specified convergence criterion (dependent on the algorithm type) is satisfied. The optimum solution is stored, the search space is updated based on the optimum solution, and a new search initiates within the updated bounds. This continues until the convergence criterion shown in equation (4.12) is satisfied, where f_n^* is the minimum fitness function obtained after the nth search. This approach can now readily be specialized to any type of damage mode by replacing s_m with the appropriate parametric description of damage geometry. Later in this thesis, this approach will be integrated with the geometric models developed earlier for through-holes and delaminations via the FE method.

4.5 Summary

This chapter presented a framework for solving conductivity-to-mechanics inverse problems using metaheuristic algorithms. These problems are extremely challenging because they are under-determined and multi-modal. As such, gradient-based optimization schemes that are traditionally used are not applicable here. Instead, the novel solution strategy proposed in this thesis integrates metaheuristic (global search) algorithms with physics-based mechanics models. This approach was specialized to two specific problems. First, piezore-

sistive inversion was considered, where the goal is to recover displacements, strains, and stresses from observed conductivity changes. In this case, a metahueristic algorithm was integrated with an analytical piezoresistivity model and used to solve an elasticity BVP for the displacements and strains. Second, the precise damage shaping problem was formulated, where the goal is to recover the precise shape and size of specific damage modes from observed conductivity changes. Two special damage cases were considered —through-holes and delaminations —and parameterized geometric models for these damage cases were developed and integrated with a metaheuristic algorithm. The solution strategies developed for both problems in this chapter will be experimentally validated later in this thesis

5. EXPERIMENTAL PROCEDURES

This chapter discusses the experimental work performed in this thesis to validate the proposed metahueristic algorithm-enabled solution strategies for piezoresistive inversion and precise damage shaping. This includes composite manufacturing, electrical testing for measuring conductivity, mechanical testing for measuring elastic properties, EIT data collection procedures, digital image correlation (DIC) setup and data collection, through-hole and impact damage testing, and optical microscopy for destructive evaluation. Two types of self-sensing composites were manufactured: CNF-modified polymer nanocomposites and CNF-modified GFRP nanocomposite laminates. The following sections describe the manufacturing and experimental testing procedures in detail.

5.1 CNF-Modified Polymer Nanocomposites

CNF-modified polymer nanocomposites were manufactured to experimentally validate the metaheuristic algorithm-enabled piezoresistive inversion methodology. These specimens were produced without a fiber reinforcement phase. Three types of specimens were manufactured: electrical testing specimens, mechanical testing specimens, and an EIT specimen.

5.1.1 Manufacturing Procedure

The manufacturing procedure used was based on the work of Tallman et al [87]. Polymer resin (Fibre Glast 2000) was mixed with the appropriate amounts of Pyrograf III PR-24-XT-HHT CNFs (Applied Sciences), surfactant (Triton X-100), and acetone in a glass beaker using a resin-to-acetone volume ratio of 2:1 and a surfactant-to-CNF weight ratio of 0.76:1. Acetone facilitates mixing by lowering the viscosity and surfactant modifies the surface chemistry to aid dispersion of the CNFs. The mixture was stirred by hand for 5 minutes and then mixed in a planetary centrifuge for 3 minutes. Next, the mixture was sonicated for 4 hours in an ultrasonic bath sonicator at 35 W with an excitation frequency of 45 kHz. After sonication, the mixture was stirred for 24 hours on a magnetic hot plate stirrer at 600 rpm and a temperature of 60 °C. This allows the acetone in the mixture to evaporate. After stirring,

the mixture was cooled down to room temperature by placing the glass beaker in shallow cold water. Next, hardener was added using a resin-to-hardener weight ratio of 100:27 and air release agent was added using an air release agent-to-total mixture weight ratio of 0.001:1. The mixture was then stirred by hand for 5 minutes and degassed for 30 minutes at room temperature in a vacuum chamber. The degassed mixture was then poured into molds that had previously been coated with a mold release agent (Fibre Glast 1153). The mixture for the electrical testing specimens was poured into two 3-D printed co-polyester molds measuring 50 mm × 50 mm × 6.35 mm each. The mixture for the EIT specimen was poured into a single 3-D printed co-polyester mold measuring 200 mm × 50 mm × 4 mm with a centrally located hole of diameter 12.7 mm. The mixture for the mechanical testing specimens was poured into two ASTM D638-14 [146] dog-bone shaped silicone rubber (Smooth-On) molds. All molds were then placed in an oven and cured for 5 hours at 60 °C.

5.1.2 Electrical Testing and SEM Imaging

Electrical testing specimens with CNF weight fractions of 0.25%, 0.50%, 1.0%, 1.5%, and 2.0% were manufactured according to the previously described procedure. Once fully cured, the specimens were removed from the 50 mm × 50 mm × 6.35 mm molds by trimming off the edges of the molds using a water-cooled tile saw. Each specimen was then cut into four smaller 25.4 mm × 25.4 mm × 6.35 mm squares using the tile saw. Colloidal silver electrodes were painted on two opposite edges of each square and the resistance, R, between the electrodes was measured using a digital multi-meter. The conductivity was then calculated as $\sigma = l/RA_e$, where l is the distance between the electrodes and A_e is the cross-sectional area of a single electrode. The conductivities measured for each weight fraction are plotted in Figure 5.1. The analytical piezoresistivity model, given by equation (4.2), was then fit to the experimental data by adjusting the values of α and β in the expression for the average inter-filler spacing. The optimum values were found to be $\alpha = 1.58$ and $\beta = -0.28$. Additionally, $\sigma_f = 10^5$ S/m, $l_f = 50$ μm, $d_f = 100$ nm, $K = 1.0$, and $\psi = 0.4$ were used in equation (4.2).

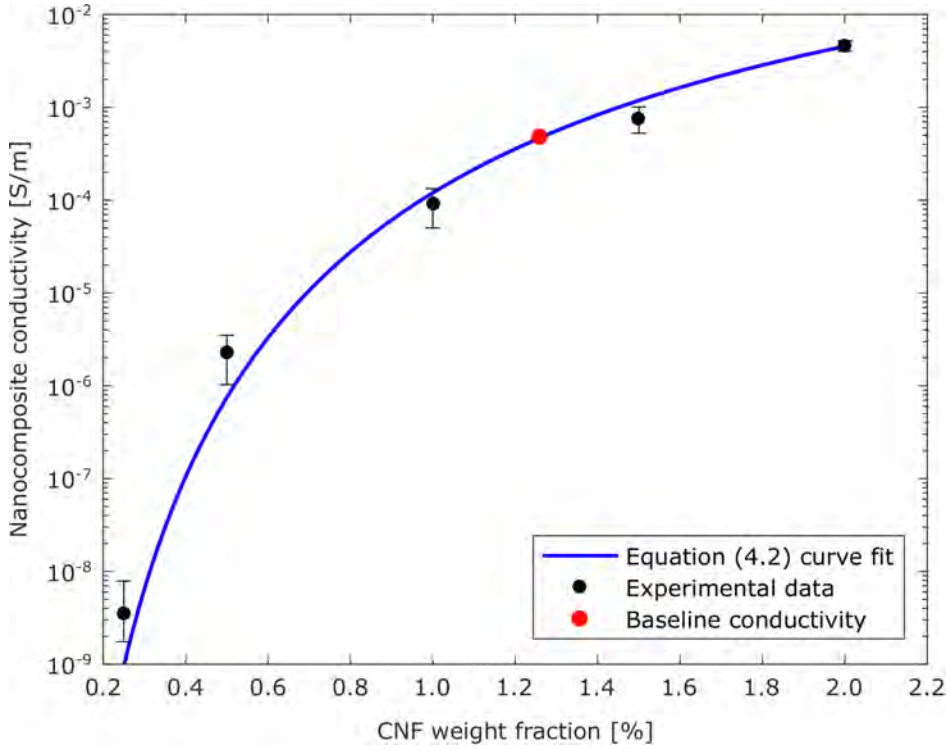

Figure 5.1. Experimentally measured and analytically predicted conductivities of CNF-modified polymer nanocomposite. The analytical piezoresistivity model, given by equation (4.2), was calibrated to the experimental data by adjusting the values of α and β in the expression for the average inter-filler spacing. The optimum values were found to be $\alpha = 1.58$ and $\beta = -0.28$.

After electrical testing, some of the squares were manually fractured and a thin platinum coating was applied to the fracture surface. Scanning electron microscopy (SEM) was then performed on the fracture surface using a Thermo-Fisher Scientific Teneo system. SEM images for a 2.0% CNF weight fraction square are shown in Figure 5.2.

5.1.3 Mechanical Testing

Mechanical testing specimens with 1.0% weight fraction of CNFs were manufactured according to the previously described procedure and molded into to tensile testing coupons according to ASTM D638-14 [146]. A CNF weight fraction of 1.0% was deliberately chosen because the EIT testing (described in the next section) utilizes a specimen with a CNF weight fraction of 1.0%. Each coupon was instrumented with two electrical resistance strain gauges:

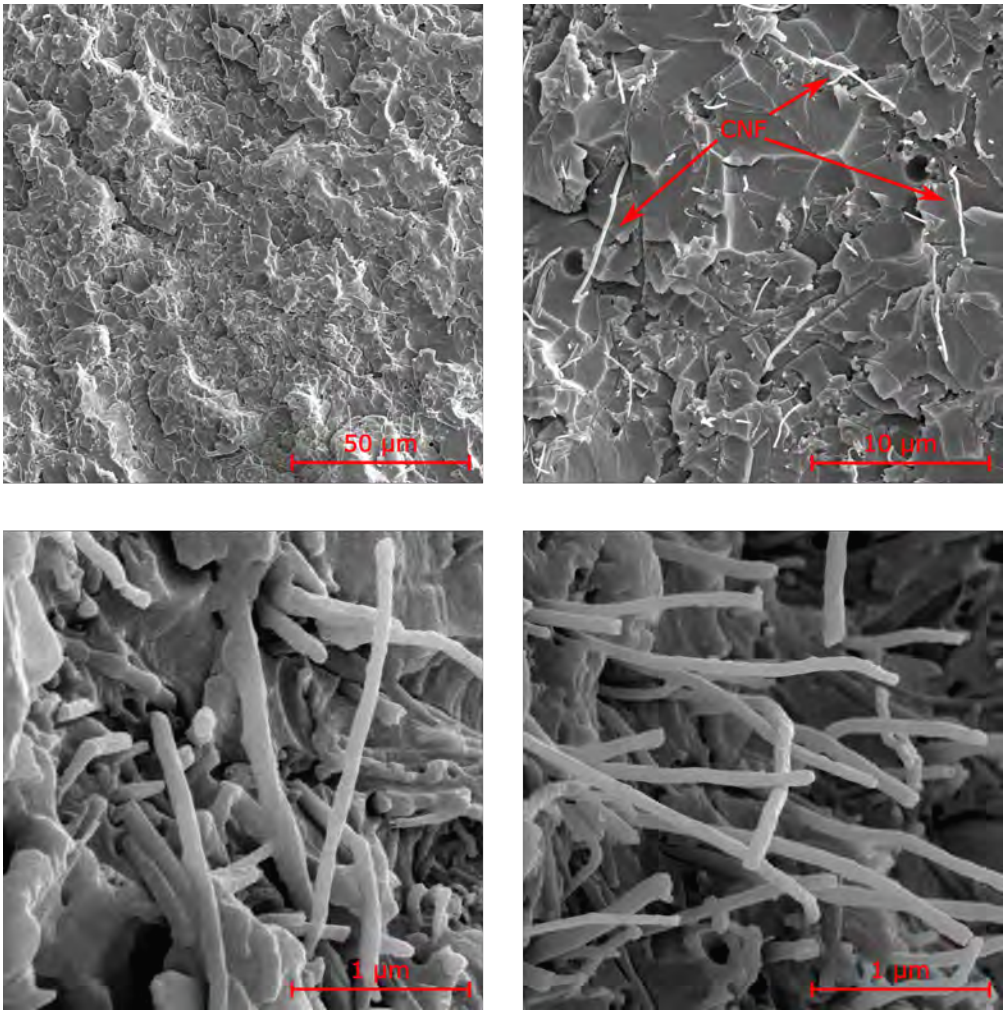

Figure 5.2. SEM images of 2.0% weight fraction nanocomposite. The image on the top right has CNFs annotated for illustrative purposes. The CNFs are more clearly visible as cylindrical rod-like structures in the bottom left and right images.

one for measuring axial strain and one for measuring transverse strain. Each coupon was then mounted on a load frame (Instron 8801) and loaded in tension at a constant displacement rate of 1.5 mm/s until failure. The mechanical testing results are shown in Figure 5.3. Using linear curve fitting, the elastic modulus was estimated as $E = 2.534$ GPa and the Poisson's ratio was estimated as $\nu = 0.35$. The failure stress of the material was estimated as $S_F = 40$ MPa.

5.1.4 EIT and DIC Data Collection

A CNF-modified polymer specimen with a nanofiller weight fraction of 1.0% was manufactured for EIT testing, as described earlier. The cured specimen was removed from the oven and trimmed to 196 mm $\times$ 46.5 mm using a water-cooled tile saw. The specimen had an as-molded thickness of 4 mm. Grip tabs measuring 57 mm $\times$ 46.5 mm $\times$ 1.72 mm were applied to the specimen using epoxy adhesive to prevent damage due to the gripping pressure of the load frame. Electrodes were applied by painting 3.175 mm wide colloidal silver patches along the gauge length of the specimen, on either side of the hole. Next, copper tape tabs were applied to the silver patches to act as extended electrodes. The copper tape was then covered with strips of masking tape to ensure good contact with the silver electrodes during the test. The fully prepared EIT specimen is shown in Figure 5.4.

The EIT specimen was then mounted on a load frame and the entire tabbed portions were gripped. The electrodes were connected to a current source (Keithley 6221) and a DAQ system (National Instruments PXIe-6368) to measure the electrode voltages. A current magnitude of 10 μA was used for the injections. One set of voltages was collected from the specimen in its undeformed configuration using the across injection scheme illustrated in Figure 5.4. From earlier testing of similar specimens, the displacement at failure was estimated as $u_F \approx 0.8$ mm. Based on this, tensile displacements of 31%, 62%, and 93% of u_F were applied and voltage measurements were collected after each applied displacement.

After EIT testing, the specimen was dismounted from the load frame, the electrode connections were removed, and the specimen was prepared for DIC measurements. For this, the gauge section was coated with white paint and an ordered speckle pattern was applied

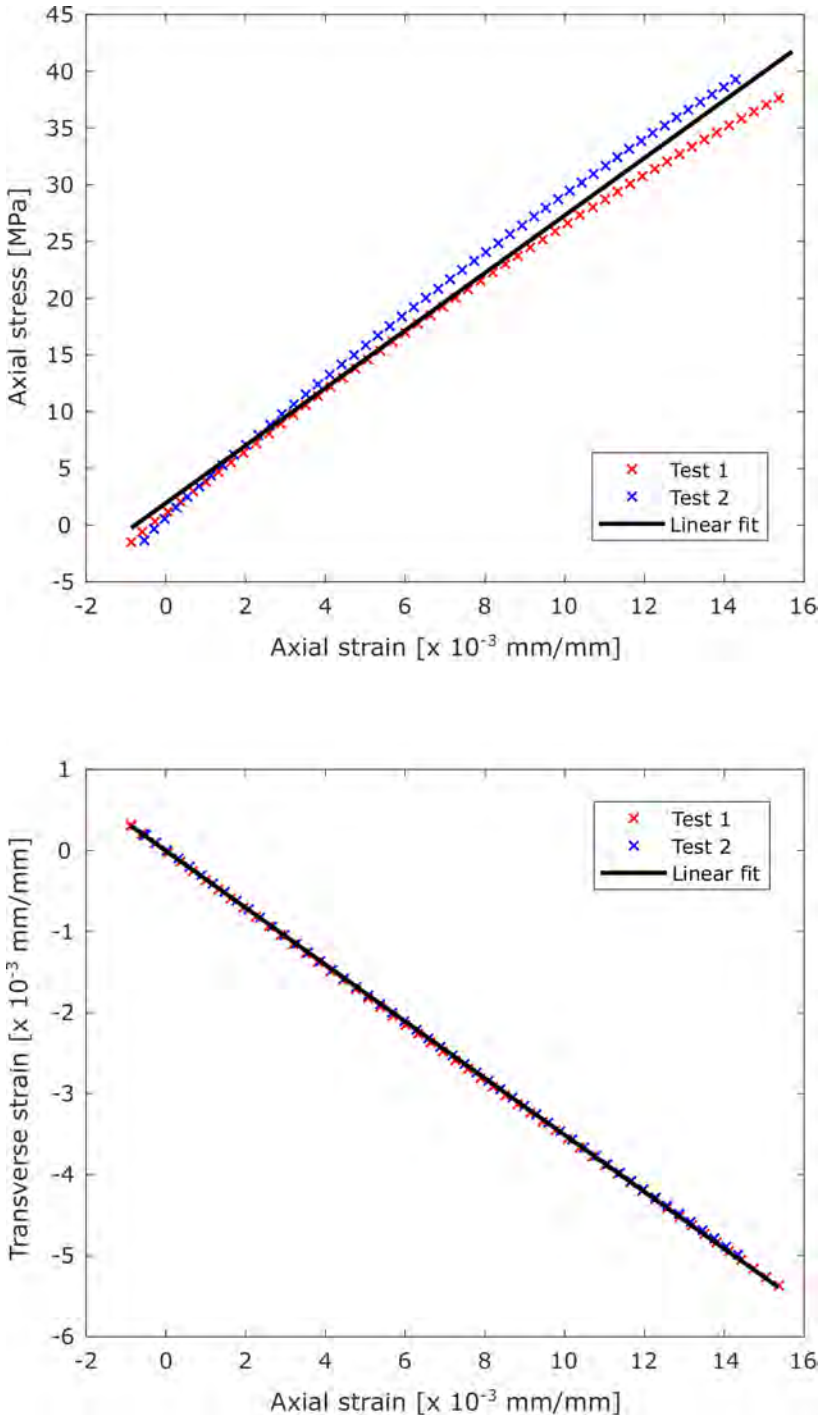

Figure 5.3. Mechanical testing results for CNF-modified polymer with 1.0% weight fraction of CNFs. Top: Axial stress versus axial strain. The elastic modulus was estimated as $E = 2.534$ GPa and the failure stress was estimated as $S_F = 40$ MPa. Bottom: Transverse strain versus axial strain. The Poisson's ratio was estimated as $\nu = 0.35$.

using a dotted roller dipped in black ink. The specimen was again mounted onto the load frame and gripped. A 5 MP DIC camera system (Correlated Solutions) was set up and calibrated and the cameras were focused on the gauge section. The specimen was then loaded in tension at a constant displacement rate of 1.5 mm/s until failure and DIC data was collected simultaneously.

5.2 CNF-Modified GFRP Nanocomposite Laminates

CNF-modified GFRP nanocomposite laminates were manufactured to experimentally validate the metaheuristic algorithm-enabled precise damage shaping methodology. Three types of specimens were manufactured: electrical testing specimens, through-hole testing specimens, and impact testing specimens.

5.2.1 Manufacturing Procedure

The lay-up procedure used here is based on the work of Tallman et al [86]. A CNF-modified polymer resin mixture with 1.0% weight fraction of nanofillers was prepared using the procedure described earlier and degassed for 20 minutes in a vacuum chamber. Unidirectional glass-fiber sheets (Fibre Glast Saertex) were then impregnated with the CNF-modified polymer to produce two laminates with stacking sequences of [0/90/90/0] and thicknesses of 3 mm. These will be referred to as laminates 1 and 2. The lay-up procedure for each laminate is as follows. An 18" × 18" aluminum tool was cleaned with acetone and sealant tape was applied around the edges. A layer of release film and a layer of peel ply were then laid down on the tool. Next, four 10" × 10" sheets of glass fiber were laid down and impregnated individually with the CNF-modified polymer using a paint brush. This was followed by laying down another layer of peel ply and a layer of breather fabric. Next, two small peel ply layers were sandwiched between four small breather fabric layers and laid on top of the larger breather fabric. The entire lay-up was then vacuum bagged. A cross-sectional schematic of the lay-up is shown in Figure 5.5. After applying a vacuum and checking for leaks, both lay-ups were transferred to an oven and cured for 5 hours at 60 °C. After curing, two specimens measuring 3.25" × 3.25" were cut from each laminate using a water-cooled

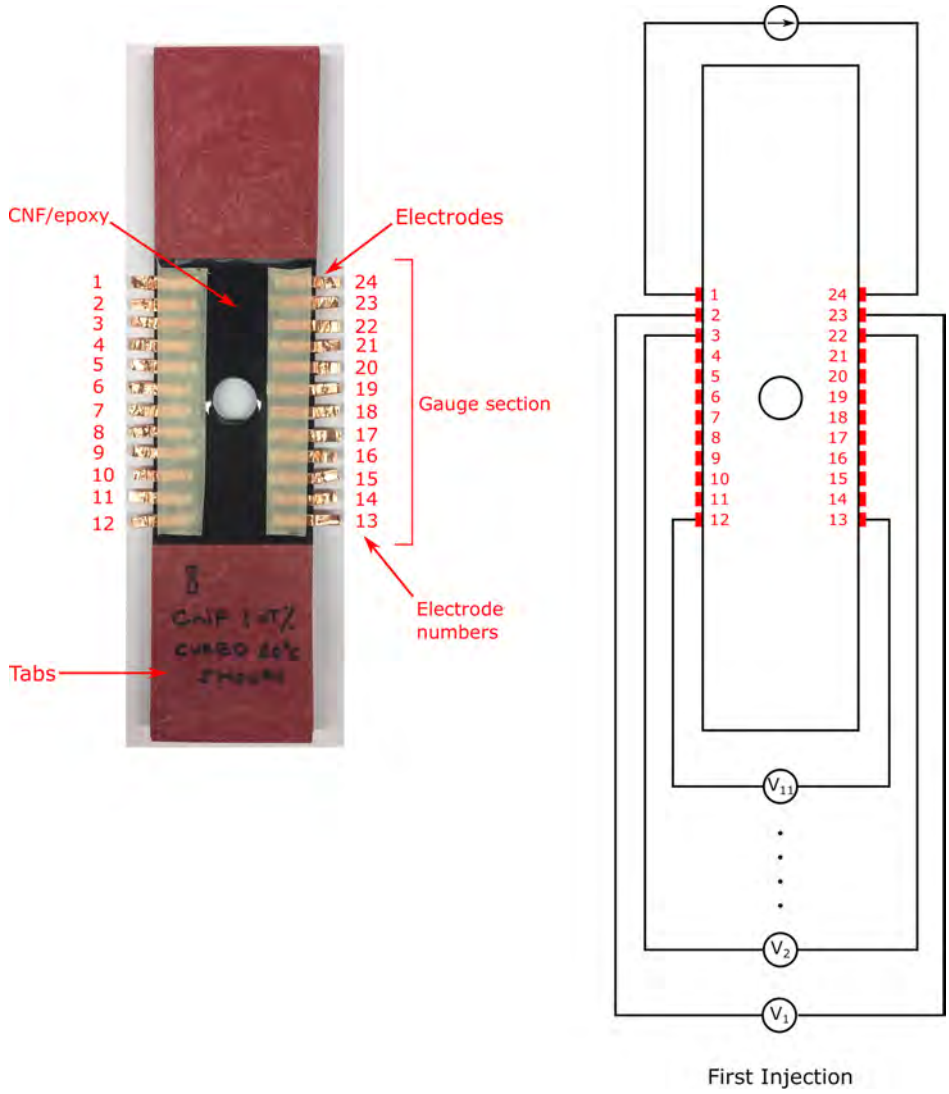

Figure 5.4. Left: Photo of fully prepared EIT specimen. Electrodes are applied to the gauge section on opposite sides of the hole and grip tabs are applied to the top and bottom portions of the specimen. Note that the electrodes are numbered counter-clockwise. Right: Illustration of first current injection and voltage measurement according to across injection scheme. Current is injected in electrode 1 and electrode 24 is grounded.

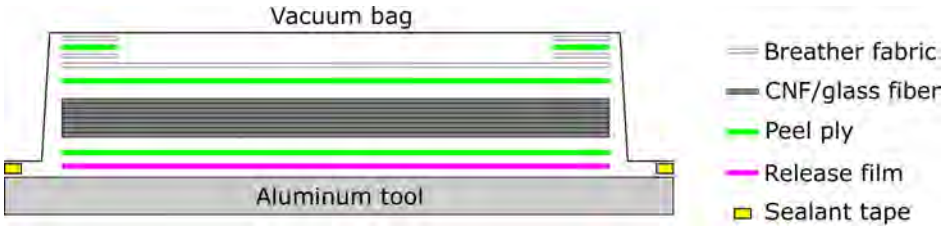

Figure 5.5. Cross-sectional schematic of lay-up used to manufacture CNF-modified GFRP laminates.

tile saw, resulting in a total of four plate-like specimens. One of these is used later for through-hole testing and the other three are used later for impact testing. A representative specimen is shown in Figure 5.7. Additionally, ten smaller specimens measuring 0.25" × 0.25" were cut out of the remaining material of the 10" × 10" laminates for in-plane and through-thickness conductivity measurements.

5.2.2 Electrical Testing

In order to estimate the baseline conductivity of CNF-modified GFRP, in-plane and through-thickness conductivity measurements were collected from each of the 0.25" × 0.25" specimens cut from laminates 1 and 2. The conductivity in the x-, y-, and z-direction was measured from each specimen. Figure 5.6 shows a schematic of the specimen and the coordinate system. To measure the conductivity in the x-direction, the faces of the specimen with normal vectors pointing in the $\pm x$-direction were fully coated with colloidal silver. The resistance, R, between the electrodes was measured using a multi-meter and the conductivity was calculated as $\sigma_x = l_x/RA_e$, where l_x is the length of the specimen in the x-direction and A_e is the area of a single electrode. This procedure was repeated to measure the conductivity in the y- and z-directions. The conductivity measurement scheme is illustrated in Figure 5.6 and the measured values of σ_x, σ_y, and σ_z are listed in Table 5.1.

5.2.3 EIT Data Collection and Optical Microscopy

The four plate-like specimens measuring 3.25"× 3.25" were used for through-hole testing, impact testing, and EIT data collection as follows. From the two specimens cut from laminate

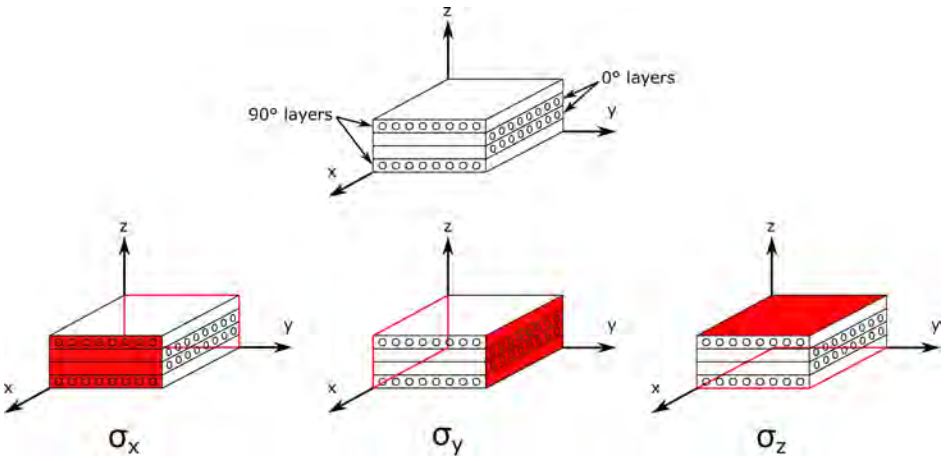

Figure 5.6. Schematic showing the principal coordinate system and the conductivity measurement scheme. Top: Schematic of a 0.25" × 0.25" specimen showing the coordinate system and the orientations of the individual layers. The ellipses indicate the fiber cross-sections. Bottom row, left to right: Conductivity measurement scheme in the x-, y-, and z-directions. The filled red rectangles represent electrodes on the front faces of the specimen and the outlined red rectangles represent electrodes on the back faces of the specimen.

Table 5.1. Mean and standard deviations of conductivities measured in the x-, y-, and z-directions from laminates 1 and 2.

Laminate	σ_x [S/m]	σ_y [S/m]	σ_z [S/m]
1	0.024 ± 0.003	0.023 ± 0.004	$(3.5 \pm 1.8) \times 10^{-4}$
2	0.054 ± 0.003	0.057 ± 0.004	$(5.6 \pm 2.2) \times 10^{-4}$

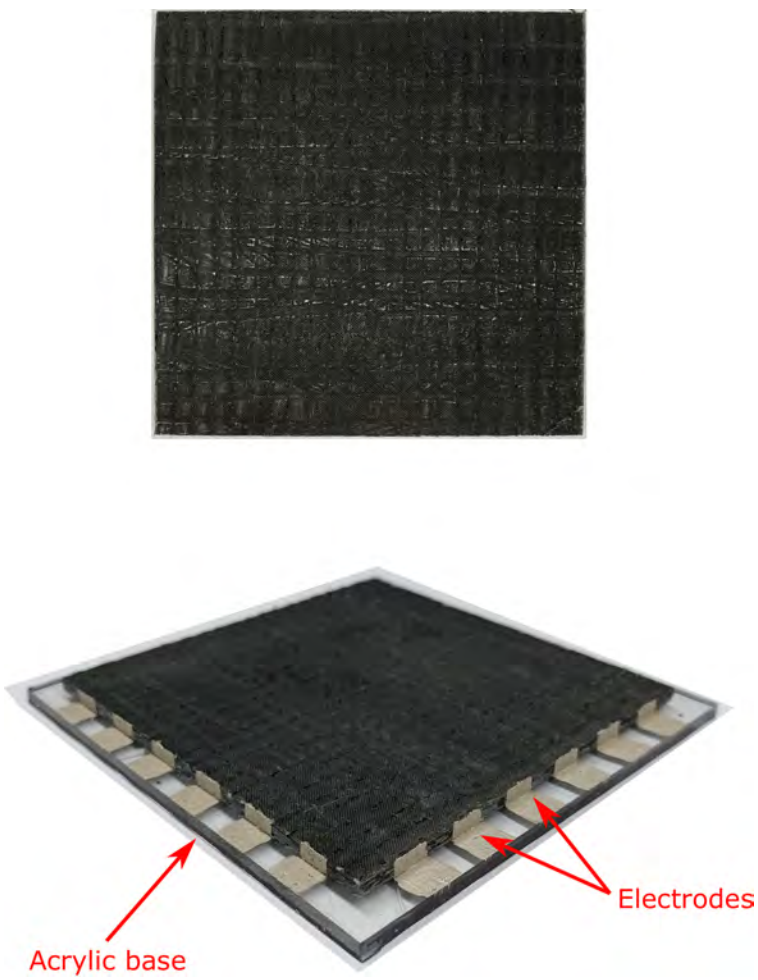

Figure 5.7. Representative 3.25" × 3.25" plate-like specimen. Top: Top-down view of specimen without electrodes. Bottom: Specimen with colloidal silver electrodes painted and mounted on acrylic base.

1, one specimen was used for through-hole testing and the other specimen was impacted with an energy of 25 J. From the two specimens cut from laminate 2, one was impacted with 23 J and the other was impacted with 28 J. EIT data was collected from each specimen by first painting evenly spaced colloidal silver patches along each edge. Each specimen was then adhered to an acrylic base using superglue and additional colloidal silver patches were painted on the acrylic to act as extended electrodes. Figure 5.7 shows a representative specimen with electrodes applied and mounted on an acrylic base. Each specimen was then connected to a current source and a DAQ system.

For the through-hole testing specimen, a current magnitude of 0.25 mA was used. One set of voltages was collected from the specimen before drilling a hole using an adjacent current injection scheme. Three circular holes of radii 1.19 mm, 2.38 mm, and 3.18 mm were then drilled and voltages were collected after drilling each new hole.

For the impact testing specimens, the impact energies (23 J, 25 J, and 28 J) were chosen deliberately so that a measurable delamination was induced without perforating the specimens. For the 23 J and 28 J impact specimens, a current magnitude of 0.25 mA was used. For the 25 J specimen, a current magnitude of 0.1 mA was used. One set of voltages was collected from each specimen before impacting using an adjacent injection scheme. Each specimen was then mounted on a 6" $\times$ 4" aluminum plate with a central square cut-out measuring 2" $\times$ 2". The aluminum plate was clamped inside a drop tower (CEAST 9340) and the specimens were impacted using a steel hemispherical striking head with a diameter of 15.8 mm. Voltages were collected from each specimen after impacting.

In order to determine the delamination shape and size, each specimen was destructively evaluated as follows. A water-cooled tile saw was used to completely cut through the specimen to expose the cross-section. The delamination length along the cross-section was then recorded using an optical microscope (Zeiss Axioscope 2 MAT) and evenly spaced micrographs of the cross-section were taken. Another cut was then made to expose a new cross-section, the delamination length was recorded again, and micrographs of the cross-section were taken again. This process was repeated until a cross-section with no delamination was observed.

5.3 Summary

This chapter described the manufacturing and testing methods employed in this thesis. Two types of self-sensing composites were manufactured and characterized. First, CNF-modified polymer nanocomposites were manufactured to validate the metaheuristic algorithm-enabled piezoresistive inversion methodology. The electrical and mechanical properties of the nanocomposite were measured and the analytical piezoresistivity model (equation (4.2)) was fit to the experimental data. A nanocomposite plate with a central hole

was then manufactured and loaded in tension while EIT and DIC data were collected. Second, CNF-modified GFRP nanocomposite laminates were manufactured to experimentally validate the metaheuristic algorithm-enabled precise damage shaping methodology. The electrical properties of the laminates were measured and plate-like specimens cut from the laminates were damaged by drilling through-holes and impacting (to induce delaminations). EIT data was collected before and after damage was inflicted. Optical microscopy was also performed on the impacted specimens to measure the delamination size. The next chapter presents the experimental EIT results for each type of self-sensing composite as well as the results obtained by solving the associated conductivity-to-mechanics inverse problem.

6. EXPERIMENTAL RESULTS AND ANALYSES

This chapter presents the experimental results and their analyses. First, for the CNF-modified polymer nanocomposite experiment, the EIT results are presented and discussed. The GA is then used to solve the piezoresistive inversion problem for the nanocomposite and the resulting strain solutions are presented. The stresses are then calculated using the inversely computed strains and used to predict failure. DIC results are also presented to validate the inversely computed strains and stresses. Second, the piezoresistive inversion problem is solved using SA and PSO and a comparison is drawn between the performances of the GA, SA, and PSO in terms of solution quality, variability, accuracy, and efficiency. Third, the results for the CNF-modified GFRP laminate experiments are presented and discussed. The EIT and GA-enabled damage shaping results for through-hole testing are presented first, followed by the EIT and GA-enabled damage shaping results for delamination (impact) testing. Optical micrographs from destructive evaluation of the impact testing specimens are also presented to validate the delamination shaping results.

6.1 Piezoresistive Inversion on CNF-Modified Polymer Nanocomposite

This section presents and analyzes the EIT and metaheuristic algorithm-enabled piezoresistive inversion results from the elastically deformed CNF-modified polymer nanocomposite specimen.

6.1.1 EIT Results

In order to determine a suitable baseline conductivity, the EIT forward problem was solved for several values of σ_0 in the range 1×10^{-7} S/m $\leq \sigma_0 \leq 1 \times 10^{-2}$ S/m. The value of σ_0 that minimized the l_2-norm of the difference between the voltages collected from the undeformed nanocomposite and the voltages predicted by solving the forward problem was chosen as the optimum baseline conductivity. This value was found to be $\sigma_0 = 4.857 \times 10^{-4}$ S/m. Note that this is a uniform baseline conductivity and not a true EIT solution. The baseline conductivity is indicated as a red circle in Figure 5.1. The corresponding CNF

weight fraction is 1.26%. The conductivity change for each applied displacement (31%, 62%, and 93% of u_F) was calculated by solving the constrained EIT inverse problem, shown again in the following equation for convenience.

$$\delta\boldsymbol{\sigma}^* = \min_{-0.7\boldsymbol{\sigma}_0 \leq \delta\boldsymbol{\sigma} \leq 0.7\boldsymbol{\sigma}_0} \frac{1}{2} \left(\left\| \begin{bmatrix} \boldsymbol{J} \\ \alpha \boldsymbol{L} \end{bmatrix} \delta\boldsymbol{\sigma} - \begin{bmatrix} \delta\boldsymbol{V} \\ \boldsymbol{0} \end{bmatrix} \right\|_2^2 \right) \tag{6.1}$$

In equation (6.1), the limits on $\delta\boldsymbol{\sigma}$ are based on the observation that the nanocomposite did not experience failure during EIT testing. Since a 100% conductivity loss only occurs due to material rupture, the maximum conductivity change increase and decrease were estimated to be 70% of the baseline conductivity. This estimation was based on previous work where piezoresistive nanocomposites were elastically deformed [116], [132], [133].

The conductivity changes obtained by solving equation (6.1) are shown in Figure 6.1. It can be immediately observed from Figure 6.1 that the magnitude of the conductivity change increases as the applied displacement increases. That is, positive conductivity changes become more positive and negative conductivity changes become more negative with increasing tensile displacement. It can also be seen that as the applied displacement increases, the conductivity decreases on the left and right edges of the hole while the conductivity increases above and below the hole. A magnified view of the conductivity change in the gauge section for each applied displacement is shown in Figure 6.2. The phenomenon observed in Figure 6.2 can be understood by considering the mechanical state of the nanocomposite in the gauge section. From elementary mechanics, it is known that a state of tension exists on the left and right edges of the hole while a state of compression exists above and below the hole. Therefore, the large tensile strains on the left and right edges of the hole increase the distance between neighboring nanofillers and cause a decrease in conductivity. Conversely, the compressive strains above and below the hole decrease the distance between neighboring nanofillers and cause an increase in conductivity. Another important observation from Figure 6.2 is that conductivity changes are localized within the gauge section of the nanocomposite. This is because the top and bottom (tabbed) portions of the specimen are entirely gripped

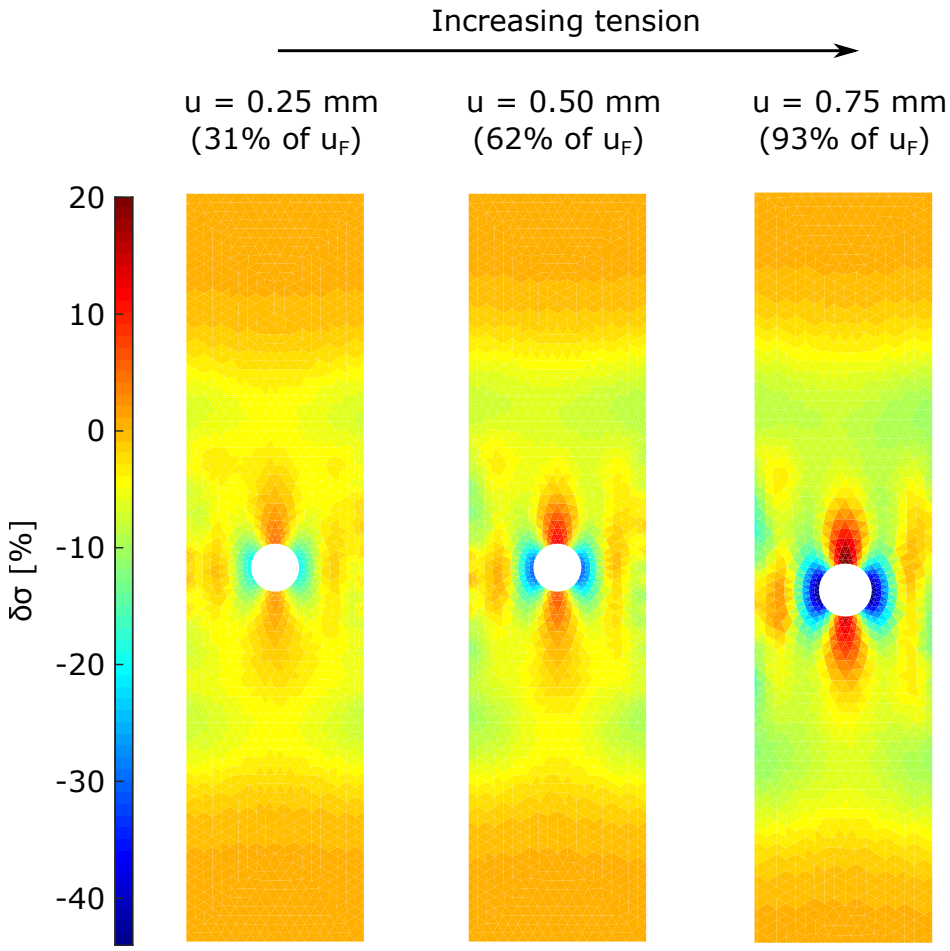

Figure 6.1. EIT conductivity change for each applied displacement in CNF-modified polymer nanocomposite. Note that the magnitude of the conductivity change increases as the applied displacement increases.

and displacement by the load frame. As such, the gauge section can be isolated to formulate the BVP for piezoresistive inversion.

6.1.2 Conductivity-to-Strain and Stress Results

Next, the metaheuristic algorithm-enabled piezoresistive inversion problem was solved for the nanocomposite using a GA. As described earlier, a BVP must be set up and the optimum boundary conditions obtained using the metaheuristic algorithm. In order to formulate the BVP, consider the experimental loading setup. The bottom gripped portion of the specimen is fixed during the experiment so the displacement on the bottom edge of the gauge section is

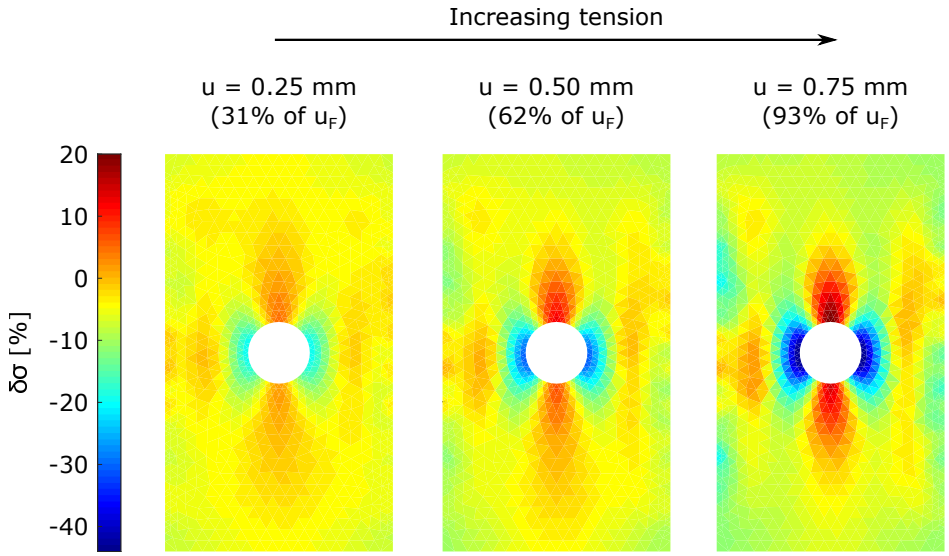

Figure 6.2. EIT conductivity change for each applied displacement in the gauge section of CNF-modified polymer nanocomposite. Note the large magnitude of the conductivity change in the vicinity of the hole due to the strain concentration. The conductivity increases above and below the hole due to compression and the conductivity decreases on the left and right of the hole due to tension.

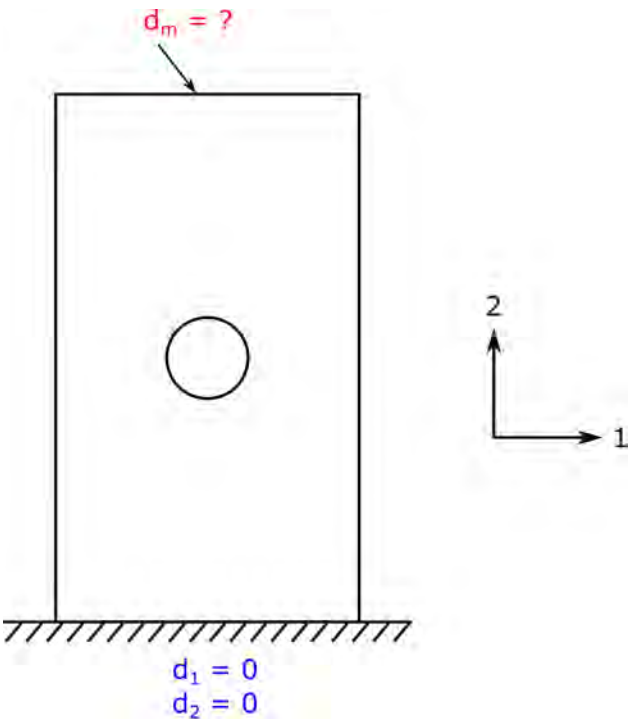

Figure 6.3. BVP for gauge section of nanocomposite specimen. The known boundary condition (blue) is zero displacement on the bottom edge and the unknown boundary condition (red) is a displacement $\boldsymbol{d}_m$ on the top edge. The GA searches for the optimum components of $\boldsymbol{d}_m$ in the 1- and 2-directions.

zero. This is the known boundary condition. The top gripped portion has an experimentally applied displacement that is to be determined. This is the unknown displacement boundary condition, $\boldsymbol{d}_m$, that the GA seeks. The BVP showing the known and unknown boundary conditions is illustrated in Figure 6.3. It should be noted that although a fixed boundary condition on the bottom edge is considered here, an uncertain boundary condition on the bottom edge can also be considered. In such a case, the GA would seek the displacements on both the top and bottom edges.

Recall again that the nanocomposite did not experience failure during EIT testing. Therefore, it is acceptable to assume that the unknown displacement, $\boldsymbol{d}_m$, must be less than the displacement at failure, $u_F = 0.80$ mm. The upper bound for the initial search space for $\boldsymbol{d}_m$ was specified as u_F and the lower bound for the initial search space was defined as $-u_F$, while being cognizant of the fact that the specimen does not have the same failure displacement in compression as it does in tension. The parameters specified for the GA were

five bits for each component of $\boldsymbol{d}_m$, a population size of 200, a 2% mutation probability, a BSA stopping criterion of 90%, and a maximum of 300 generations. Using these parameters, successive searches for $\boldsymbol{d}_m$ were performed using the GA until the convergence criterion in equation (4.8) was satisfied. The resulting displacement fields were used to compute the first principal strains. These are shown in the top row in Figure 6.4. The first principal strain is important because conductivity changes predicted via equation (4.2) are primarily driven by the first principal strain. In order to validate the inversely computed strains, a series of standard FE simulations were performed where the experimentally applied displacements were applied to FE models of the gauge section of the nanocomposite. These were meant to represent the 'exact' solutions. The resulting first principal strains are shown in the middle row in Figure 6.4. Additionally, the DIC measurements recorded during the experiment were used to calculate the first principal strains. These are shown in the bottom row in Figure 6.4. The DIC post-processing was performed using VIC-3D (Correlated Solutions) with a subset size of 31. Note that the DIC images use a different color scale.

From Figure 6.4, it can be immediately seen that the inversely computed strains agree very well with the standard FEM strains and the DIC strains. Some artifacts are present in the GA-predicted strains but there is overall good agreement. The convergence behavior for the GA is shown in Figure 6.5. For the first search of each displacement case, the BSA stopping criterion is achieved after 100 generations, on average, and the minimum fitness function at the end of each search decreases with successive searches. The global convergence criterion in equation (4.8) is satisfied after the fourth search.

Next, the inversely computed strains were used to calculate stresses using the constitutive relations for linear elastic materials, shown in equation (6.2). Here, E and ν are the experimentally measured elastic modulus and Poisson's ratio, respectively, and S_{ij} are the components of the Cauchy stress tensor. The symbol S is used deliberately for stress to avoid confusion with the symbol for conductivity, σ.

$$S_{ij} = \frac{E}{1+2\nu}\left[\varepsilon_{ij} + \left(\frac{\nu}{1-2\nu}\right)\varepsilon_{kk}\delta_{ij}\right] \tag{6.2}$$

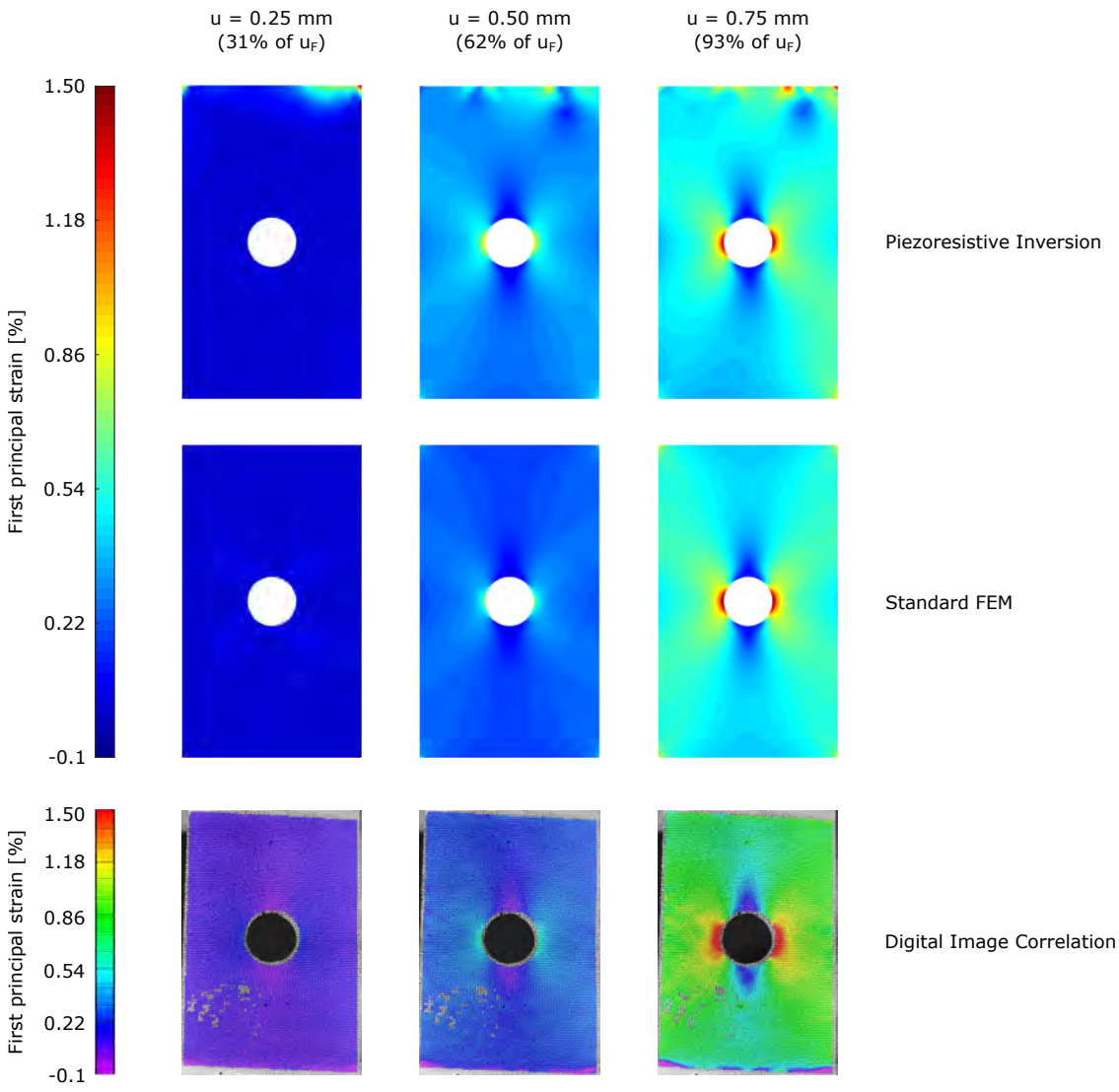

Figure 6.4. First principal strains obtained using the GA, standard FEM, and DIC.

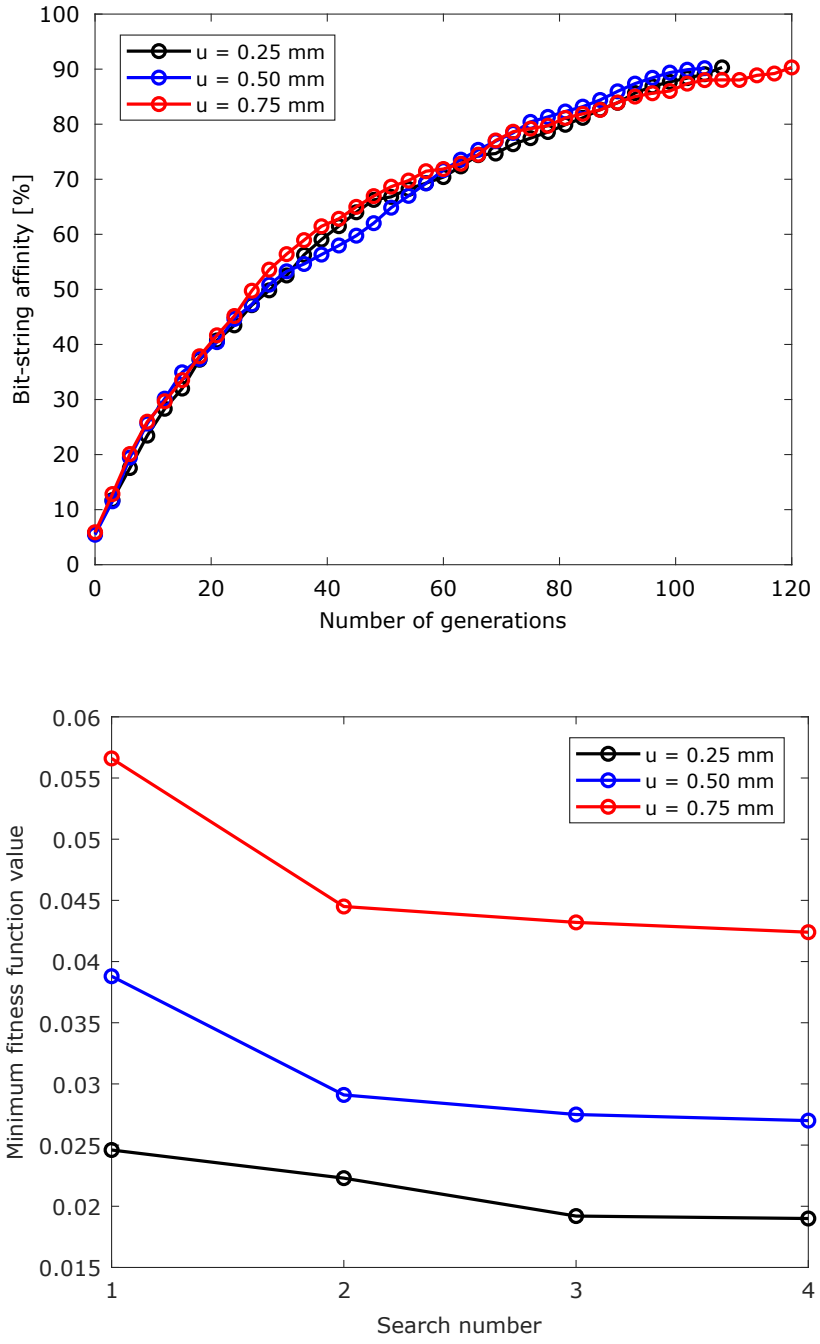

Figure 6.5. Convergence analysis for GA-enabled piezoresistive inversion. Top: BSA convergence for first search of each displacement case. Bottom: Fitness function convergence for multiple searches of each displacement case. The global convergence criterion is satisfied after the fourth search.

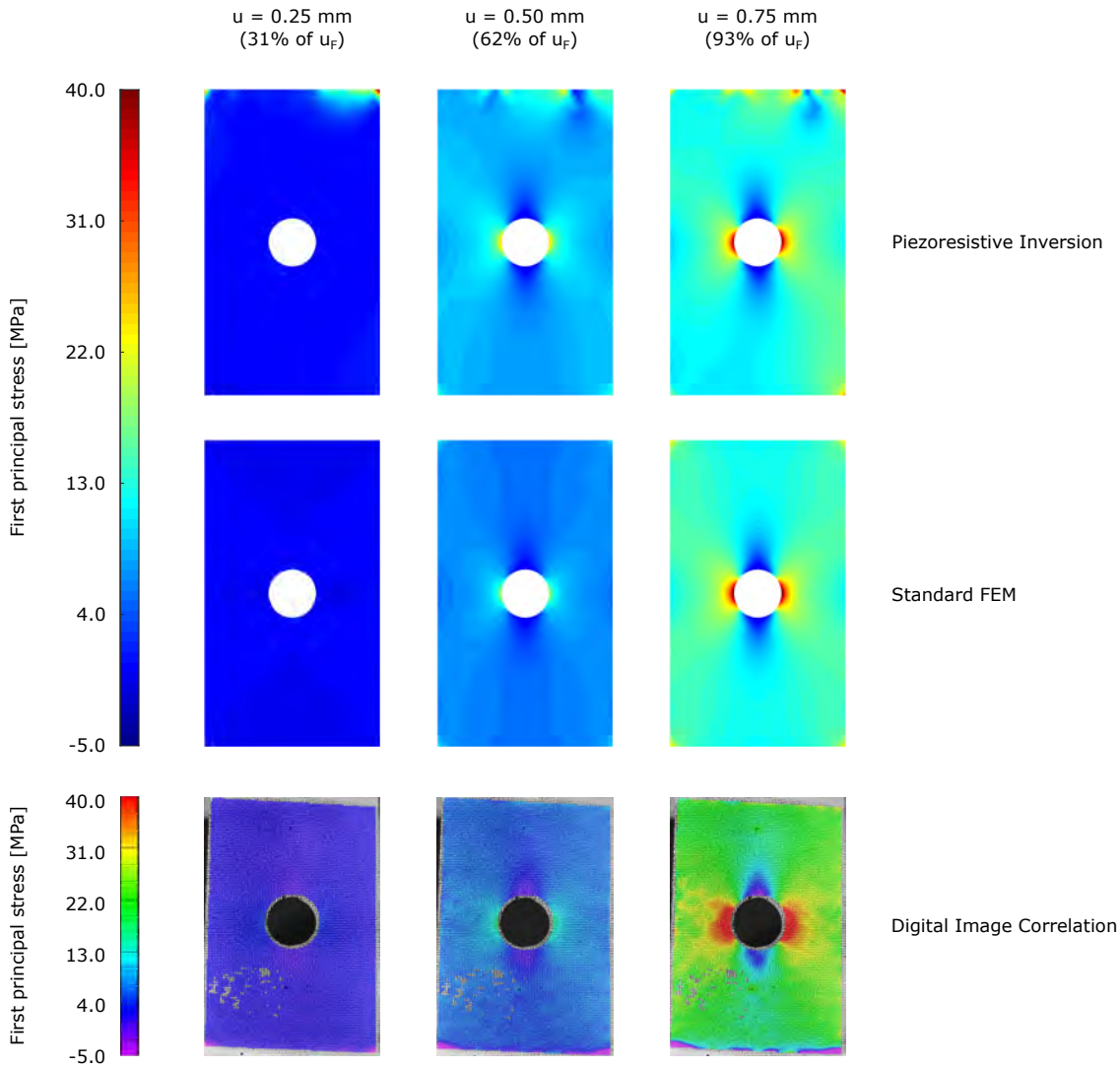

Figure 6.6. First principal stresses obtained using the GA, standard FEM, and DIC.

The inversely computed first principal stresses for each displacement case are shown in Figure 6.6 along with the standard FEM-predicted and DIC-measured first principal stresses. It can be clearly seen from Figure 6.6 that the GA is able to accurately reconstruct the stress state of the nanocomposite. Similar to the strains, minor artifacts are present in the stresses. This is due to the variability in the individual components of the GA-predicted displacement boundary condition. That is, some components of $\boldsymbol{d}_m$ vary considerably from others. This variability is amplified in the strains and stresses because these quantities are computed using the gradient of the displacement field.

6.1.3 Failure Prediction Results

Next, having solved the piezoresistive inversion problem to obtain the strains and stresses, it is demonstrated that the inversely computed mechanical state of a self-sensing composite can be used to accurately predict material failure. For this, a simple stress-based failure criterion for brittle materials is used which predicts failure when the first principal stress exceeds the failure stress of the material. This is shown in equation (6.3), where S_1 is the first principal stress and S_F is the experimentally determined failure stress.

$$\frac{S_1}{S_F} \geq 1 \tag{6.3}$$

The above failure metric was calculated for each applied displacement case and the results are shown in Figure 6.7. It can be seen from Figure 6.7 that as the applied displacement increases, equation (6.3) predicts that failure is most likely to occur at the left and right edges of the hole. The inversely computed solutions are able to accurately capture this phenomenon and show good agreement with standard FEM and DIC solutions.

6.2 Comparison of GA, SA, and PSO for Piezoresistive Inversion

In the previous section, piezoresistive inversion for the CNF-modified polymer nanocomposite experiment was solved using the GA. Although the inversely computed solutions showed good accuracy overall, some minor artifacts were observed in the strains and stresses in Figures 6.4 and 6.6, respectively. This was attributed to small variations in the GA-generated displacement boundary condition vector, $\boldsymbol{d}_m$, that are amplified when gradients are calculated. As such, it is important to explore other metaheuristic algorithms to see if the solution variability can be reduced and the quality of the inversely computed strains and stresses can be improved. To that end, the piezoresistive inversion problem for the CNF-modified polymer nanocomposite was solved using two additional algorithms —SA and PSO —and their performances were compared to the performance of the GA. Note that the same EIT solutions (shown in Figure 6.2) and BVP (shown in Figure 6.3) were used for all three algorithms. For SA, an initial guess of zero displacement, an initial temperature of 0.01, and

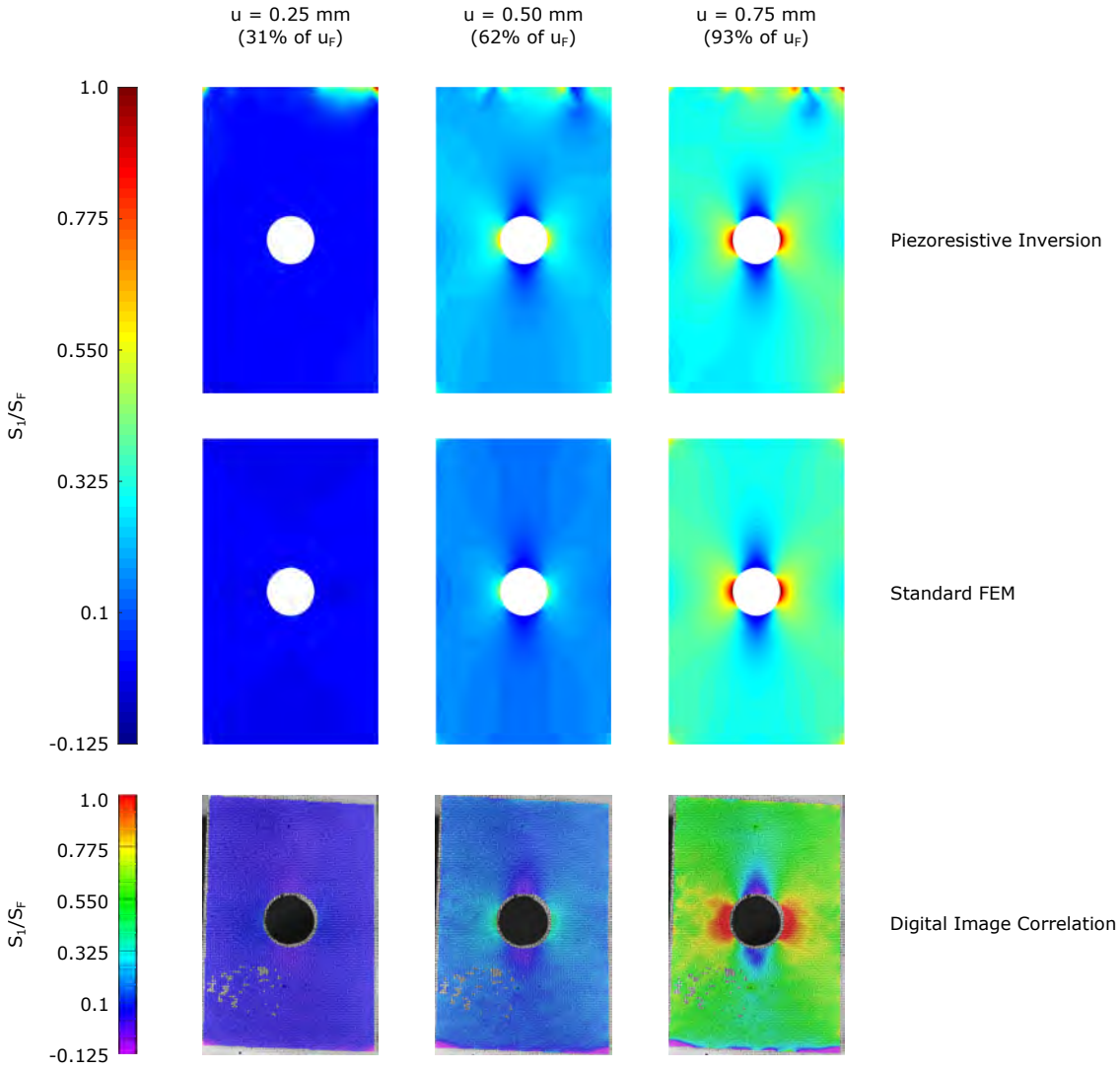

Figure 6.7. Stress-based failure metric calculated for the inversely computed solutions, standard FEM, and DIC.

a reannealing interval of 20 were specified. For PSO, an initial swarm span of 500, and an initial swarm size of 100. The convergence criterion for both algorithms was specified as a function tolerance of 1×10^{-6}. That is, convergence is achieved when the relative change in fitness function is less than 1×10^{-6}. These initialization parameters were selected to optimize the performances of the SA and PSO algorithms by giving the lowest fitness function value in the shortest run-time.

6.2.1 Displacements and Strains

The displacements obtained using the three algorithms are shown in Figure 6.8. It can be seen that SA and PSO are able to reconstruct the overall shape and magnitude of the displacement with good accuracy. However, there is considerable variability in the displacement magnitude along the top edge generated using the SA. This is particularly pronounced for the case of $u = 0.50$ mm. The PSO solutions show comparatively less variability in the displacement magnitude along the top edge.

The fitness function convergence for multiple searches of the three algorithms is shown in Figure 6.9. The GA shows the most marked change in the minimum fitness function value after the first search. For the cases when $u = 0.50$ mm and $u = 0.75$ mm, both SA and PSO show very little change in the minimum fitness function. However, the change is considerable for the case when $u = 0.25$ mm. The global convergence criterion in equation (4.8) is satisfied for all three algorithms after the fourth search.

The first principal strains computed using the three algorithm, standard FEM, and DIC are shown in Figure 6.10. The strains have been scaled according to the maximum and minimum strains obtained via standard FEM. As a result, the strains for SA and PSO have dark red regions close to the top edge of the domain. This is because the strains in these regions are much larger than 1.5%. This was done to illustrate that variations in the displacement boundary condition for the top edge for SA and PSO can lead to large, unrealistic strains. Therefore, re-scaling the strains according to standard FEM solutions allows for much clearer visualizing of the strain state in the vicinity of the hole. From Figure

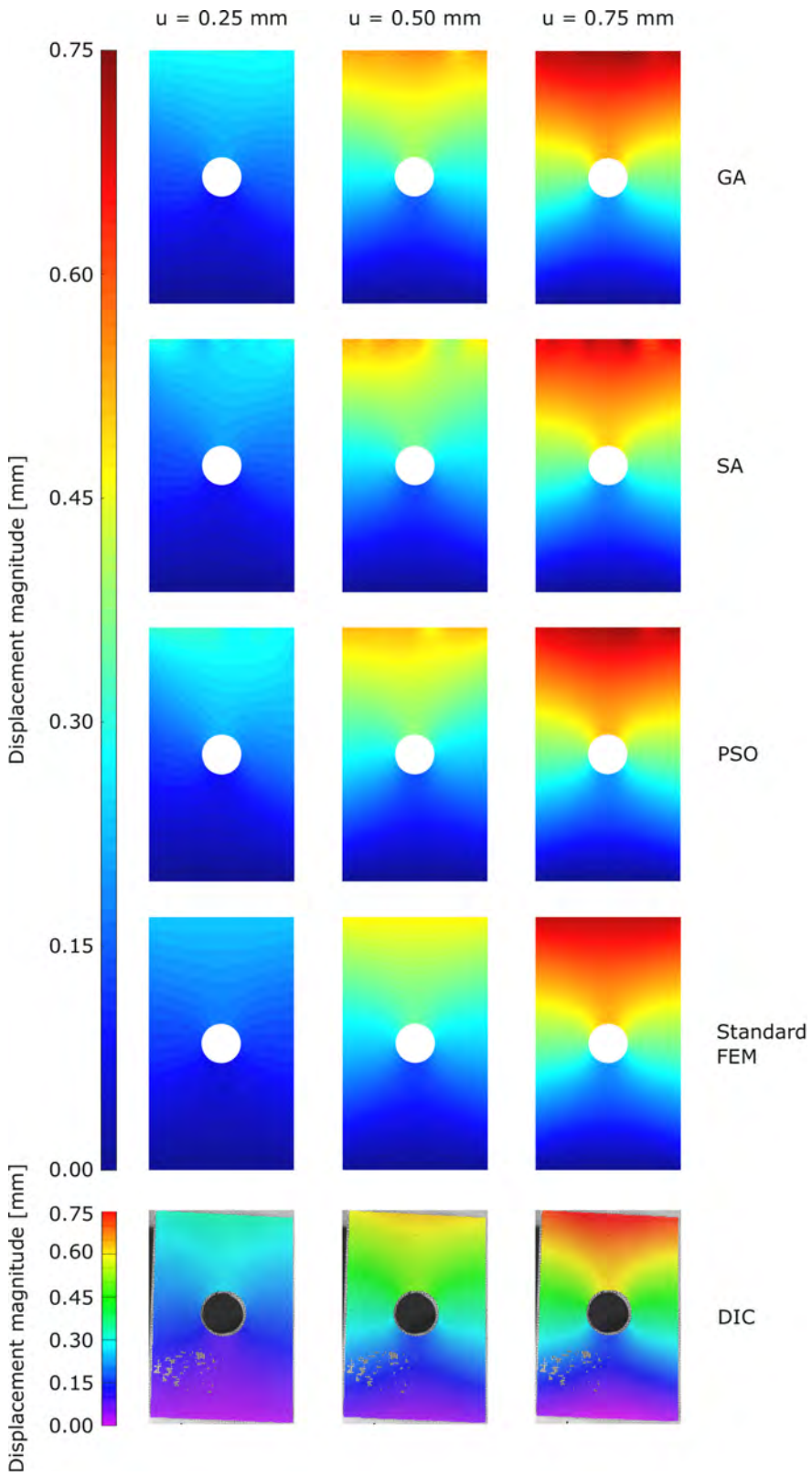

Figure 6.8. Displacement magnitude computed using the GA, SA, PSO, standard FEM, and DIC. ©2020 IEEE.

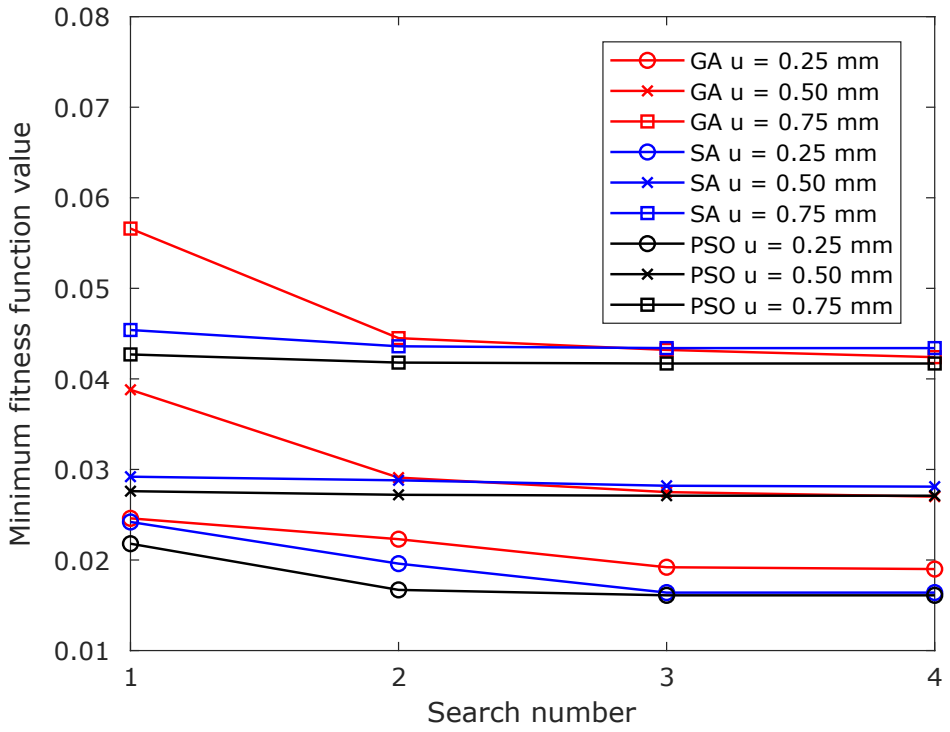

Figure 6.9. Fitness function convergence for GA, SA, and PSO. ©2020 IEEE.

6.10, it can be seen that the strains in the vicinity of the hole predicted using SA and PSO agree well with the standard FEM solutions and DIC measurements.

The variability in the SA and PSO strain solutions can be more closely studied in Figure 6.11. This figure shows the first principal strains in a small rectangular region close to the top edge of the domain. The strains have been scaled according to the first principal strains from SA (since these are the largest). For SA, the strain artifacts become larger in magnitude as the applied displacement increases and the largest strains occur at the top left and top right corners for the case when $u = 0.75$ mm. The strain artifacts for PSO are comparatively smaller in magnitude than SA. The largest artifacts occur at the top left and top right corners for the case when $u = 0.25$ mm.

6.2.2 Variability and Accuracy

Metaheuristic algorithms perform a non-smooth search, meaning no gradients of the fitness function are calculated to compute step size or search direction. Instead, solutions are generated and selected based on a combination of probabilistic and heuristic techniques. Therefore, if a metaheuristic algorithm is used to search for a solution to a problem multiple times, some variability in the solution may be observed for multiple searches. Given that small variations in displacement can cause large variations in strains, it is worthwhile to examine the degree of variability in the GA-, SA-, and PSO-generated displacement boundary condition, $\boldsymbol{d}_m$. For this, each algorithm was run ten times for the case when $u = 0.75$ mm. The mean and standard deviation of the nodal displacement magnitude along the top edge for each algorithm is shown on the top in Figure 6.12. It can be observed that SA has the largest variability between different searches and it also has the largest inter-node variation in displacement magnitude. This observation lends credence to the explanation that the strains for SA are larger than those for the GA and PSO because there are much more pronounced 'jumps' in the displacement between adjacent nodes for SA. The inter-node displacement variation is similar for the GA and PSO. Furthermore, both the GA and PSO show a similar trend in the displacement along the top edge. That is, the displacement decreases sharply close to the left edge and then steadily increases towards the mid-point

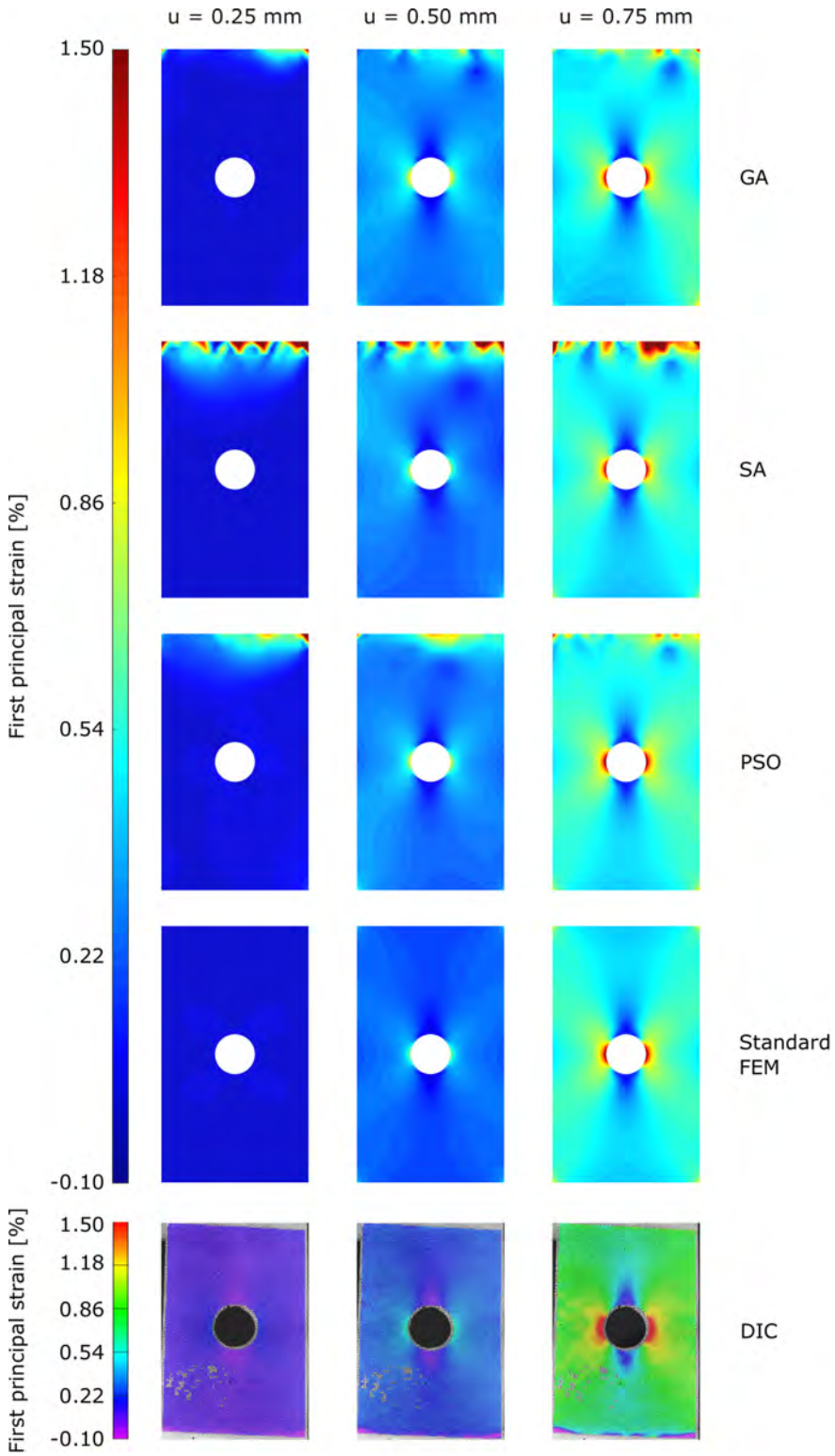

Figure 6.10. First principal strain computed using the GA, SA, PSO, standard FEM, and DIC. ©2020 IEEE.

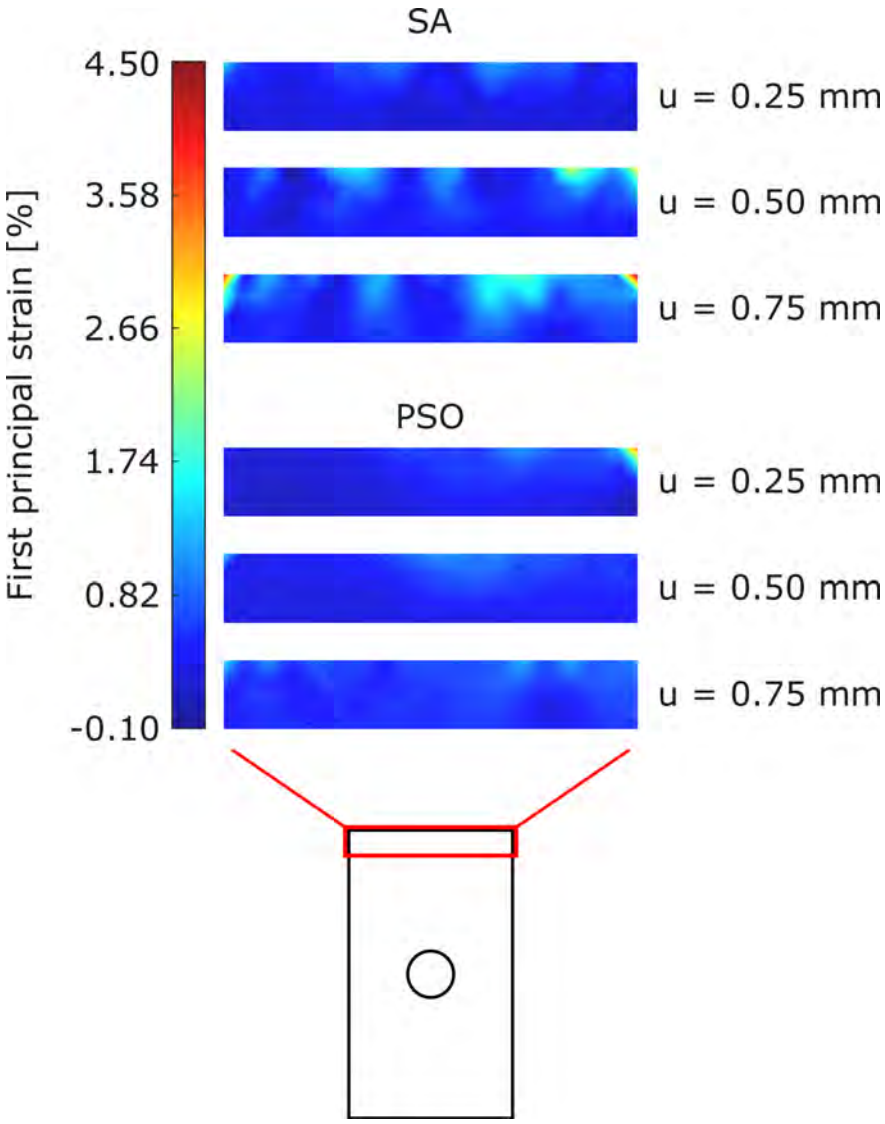

Figure 6.11. First principal strains computed using SA and PSO in a region of interest near the top edge of the domain, indicated by the red rectangle. ©2020 IEEE.

of the edge. The displacement then decreases sharply close to the right edge. These sharp changes in displacement are the cause of the strain artifacts observed in Figure 6.10. One possible cause of this variability is noise in the experimental data.

In order to quantify the accuracy of the inversely computed solutions, the percent error between the GA-, SA-, and PSO-generated displacement of the top edge and the FEM solution was calculated for the case when $u = 0.75$ mm. Note that the FEM solution is meant to represent the 'exact' solution in this case. The percent error is shown on the bottom in Figure 6.12. Two key observations can be made. First, the error for SA is highest close to the corners of the top edge. Second, the error trends for the GA and PSO are similar across the plate. However, the PSO displacement has a larger error variability in the center of the plate. This explains why larger strains are observed for PSO than the GA. Based on these results, it can be stated that, of the three algorithms, the GA has the overall best accuracy and smallest variability.

6.2.3 Efficiency

Lastly, in order to determine which algorithm is the most efficient at solving the piezoresistive inversion problem, a new 'efficiency' metric was defined as shown in equation (6.4). In this equation, ψ_n is the efficiency for the nth search, f_n^* is the minimum fitness function value obtained after the nth search, and t_n is the run-time (in minutes) for the nth search of the algorithm. Therefore, a lower fitness function value or a shorter run-time result in a higher efficiency.

$$\psi_n = \frac{1}{f_n^* t_n} \tag{6.4}$$

The efficiencies computed for all searches of all three algorithms are plotted in Figure 6.13. It can be immediately seen that for a given displacement case, the GA has the highest efficiency. This indicates that the GA generates the best quality solution in the shortest run-time. It can also be seen that the efficiency of each algorithm increases as the applied displacement increases. For the cases when $u = 0.25$ mm and $u = 0.50$ mm, the efficiency of the GA increases considerably with successive searches. This is because, as the search space

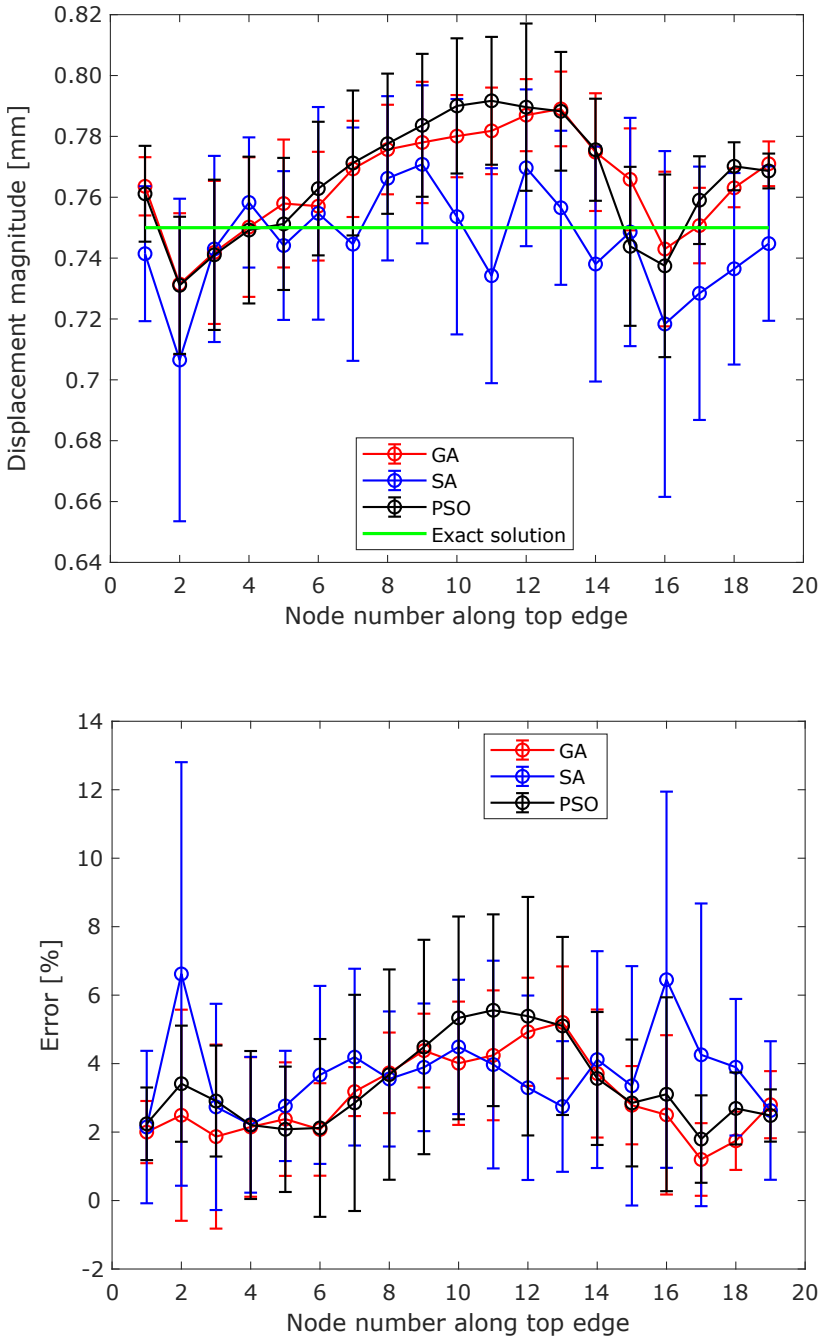

Figure 6.12. Variation in the nodal displacement magnitude of the top edge for ten searches of each algorithm for the case when $u = 0.75$ mm. The node numbers run from left to right along the top edge. That is, node 1 is located at the top left corner and node 19 is located at the top right corner. Top: Nodal displacement magnitude for the GA, SA, and PSO compared with the FEM (exact) solution. Bottom: Percent error between the GA-, SA-, and PSO-generated solutions and the FEM solution. ©2020 IEEE.

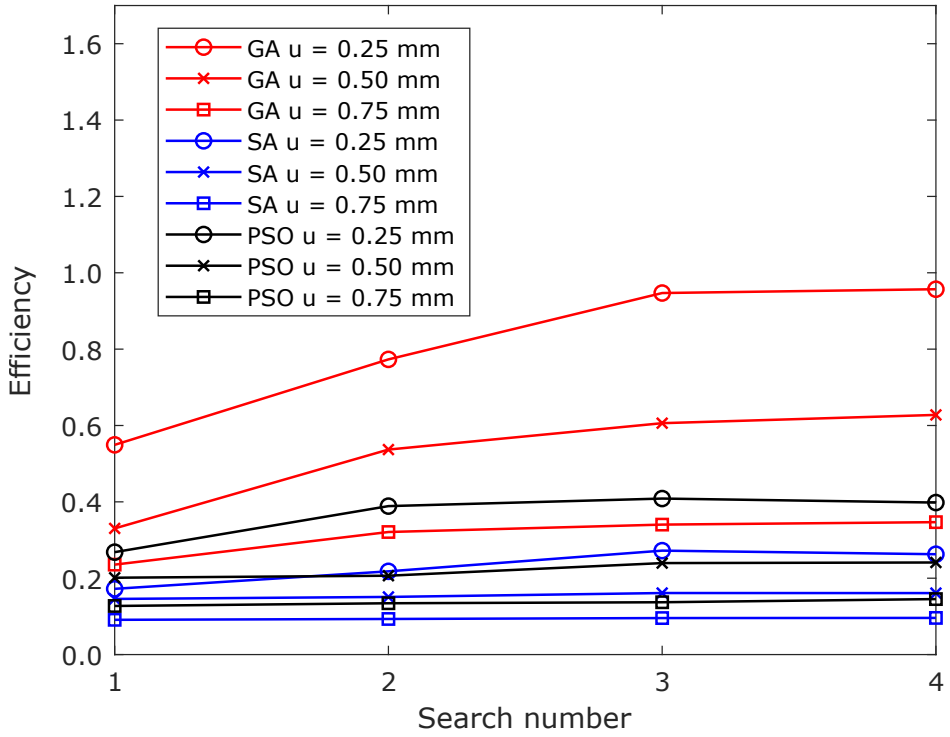

Figure 6.13. Efficiency computed for all searches using all three algorithms. ©2020 IEEE.

is reduced, the GA requires fewer generations and shorter run-times to find an optimum solution. It can also be seen that SA has a lowest efficiency followed by PSO. Furthermore, the efficiencies of SA and PSO show very little change with increasing number of searches. Therefore, it can be definitively stated that the GA is the most efficient algorithm for solving this problem.

6.3 Precise Damage Shaping on CNF-Modified GFRP Nanocomposite Laminates

This section presents and analyzes the EIT and metaheuristic algorithm-enabled precise damage shaping results from the through-hole and impact testing experiments performed on CNF-modified GFRP nanocomposite laminates.

6.3.1 Through-Hole Shaping Results

In order to determine a suitable EIT baseline for the CNF-modified GFRP laminates, the mean conductivities listed in Table 5.1 were used an initial estimate. Linear least squares minimization was then used to iteratively update the initial estimate to find a uniform optimum baseline conductivity that minimized the difference between the experimental pre-damage voltages and the numerically computed voltages. Again, this is a uniform conductivity and not true EIT. For the through-hole testing specimens, the optimum in-plane baseline conductivities were found to be $\sigma_{x0} = \sigma_{y0} = 0.025$ S/m. The constrained EIT inverse problem shown in equation (6.5) was then solved to obtain the conductivity change. Note that the constraints on $\delta\boldsymbol{\sigma}$ in equation (6.5) are based on realistic assumptions about the expected conductivity change. That is, it is well understood that damage such as through-holes and delaminations causes a decrease in conductivity. The maximum decrease that is physically possible has a magnitude equal to the baseline conductivity and the maximum increase is relatively small. Therefore, an upper bound of 1% and a lower bound of -100% of the baseline conductivity is used in equation (6.5).

$$\delta\boldsymbol{\sigma}^* = \min_{-\boldsymbol{\sigma}_0 \leq \delta\boldsymbol{\sigma} \leq 0.01\boldsymbol{\sigma}_0} \frac{1}{2} \left(\left\| \begin{bmatrix} \boldsymbol{J} \\ \alpha \boldsymbol{L} \end{bmatrix} \delta\boldsymbol{\sigma} - \begin{bmatrix} \delta\boldsymbol{V} \\ \boldsymbol{0} \end{bmatrix} \right\|_2^2 \right) \tag{6.5}$$

The EIT results obtained using the above equation are shown in the left column in Figure 6.14. It can be observed from Figure 6.14 that EIT is able to detect the presence of the holes. Another interesting observation is that larger magnitude conductivity changes generally indicate more severe damage. For example, for the case of three holes, the EIT image shows a larger conductivity change in vicinity of the largest hole than the conductivity change in the vicinity of the two smaller holes. Therefore, some limited information about the size of the holes can be obtained from the EIT image.

In order to precisely recover the shapes and sizes of the holes from the EIT-imaged conductivity changes, the precise damage shaping problem was solved using the GA. Recall that a geometric model for through-holes was developed earlier. In order to solve equation (4.10), the GA was integrated with this geometric model using an adaptive meshing algorithm

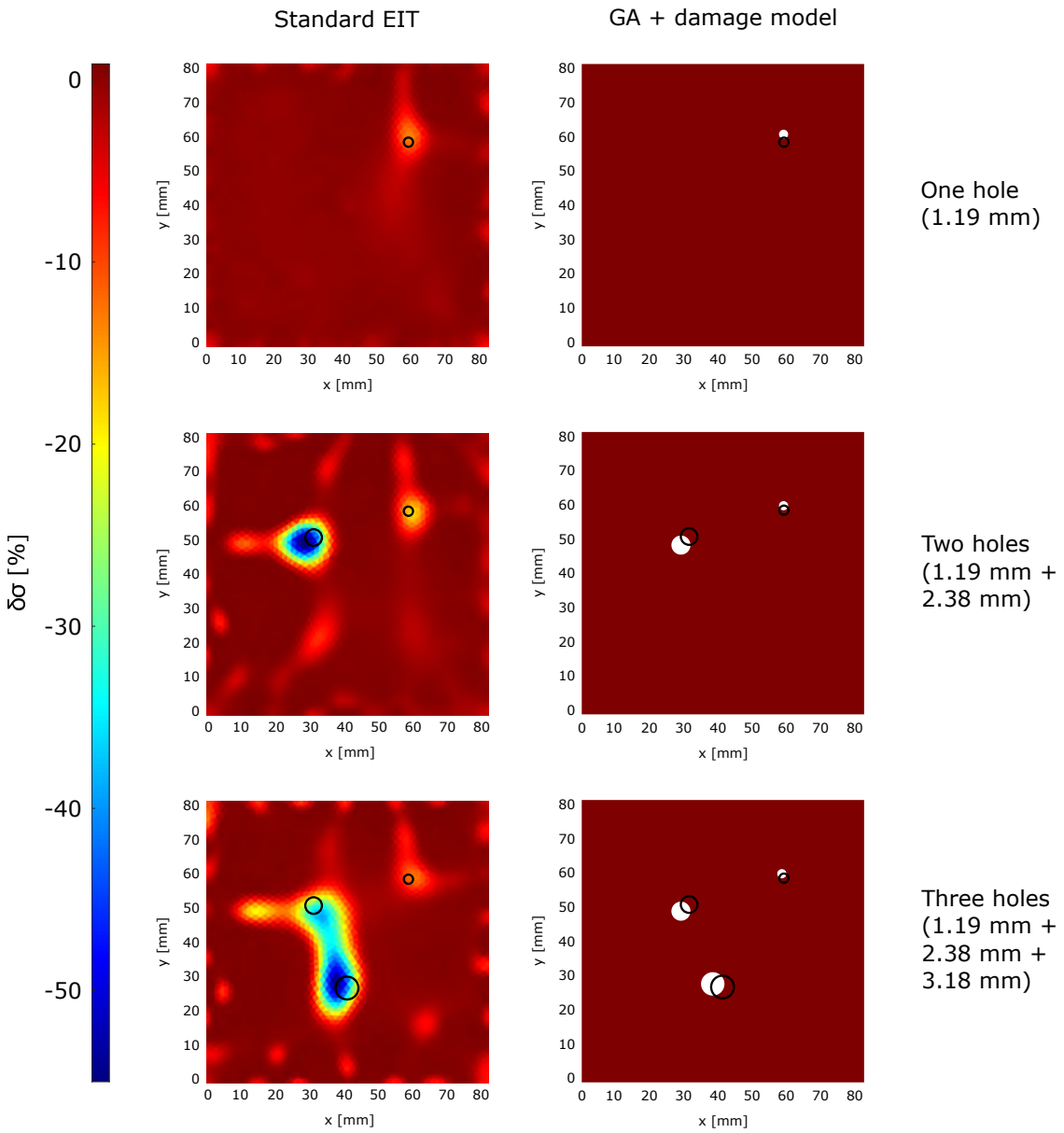

Figure 6.14. EIT conductivity changes (left column) and GA-enabled precise damage shaping results (right column). The black circles indicate the actual sizes and locations of the holes.

[147], [148] that generated circular cavities inside a FE mesh described by $s_m = [x_c, y_c, r]$. The bounds on the initial search space for the GA, $s_m^{\min}$ and $s_m^{\max}$, were specified based on the sizes, locations, and conductivity change magnitudes observed in the EIT images. For example, for the case of one hole, the lower bound was $s_m^{\min} = [55, 55, 0.5]$ mm and the upper bound was $s_m^{\max} = [62, 62, 5]$ mm. The parameters used for the GA were a population size of 50, a BSA stopping criterion of 99%, and a maximum of 30 generations.

The results from the GA-enabled through-hole shaping problem are shown in the right column in Figure 6.14. For the case of one hole, the algorithm is able to reconstruct a hole with a radius of 1.33 m. For two holes, the algorithm reconstructs one hole with a radius of 1.34 mm and a second hole with a radius of 2.79 mm. Lastly, for the case of three holes, the GA reconstructs one hole with a radius of 1.34 mm, a second hole with a radius of 2.79 mm, and a third hole with a radius of 3.43 mm. It is clear that these results are considerably more accurate and provide much more information about damage shape than standard EIT. The average percent errors in the through-hole sizes and locations predicted using the GA are listed in Table 6.1.

Table 6.1. Average percent error in GA-generated hole sizes and locations relative to actual hole sizes and locations. In this table, e_{x_c} and e_{y_c} are the average percent errors in the x- and y-coordinates of the center of the hole and e_r is the average percent error in the hole radius.

Hole number	e_{x_c} [%]	e_{y_c} [%]	e_r [%]
1	1.67	3.33	11.76
2	3.33	5.77	17.22
3	9.52	3.70	7.86

The BSA convergence for the first search of each case and the fitness function convergence for all searches are shown in Figure 6.15. For the first search for the case of one hole, BSA convergence is achieved after 16 generations and further searches do not improve the solution quality. For the cases of two holes, 20 generations are required to achieve BSA convergence and the solution improves slightly after repeated searches. For the first search of the case of three holes, the maximum number of generations is reached before BSA convergence is achieved. Furthermore, this case shows the most pronounced improvement in solution quality

for consecutive searches. This is because as the number of holes increases, the number of parameters in the geometric model also increases and the algorithm requires a larger number of generations to converge.

6.3.2 Delamination Shaping Results

The optimum baseline conductivities of the impact testing specimens were obtained using an iterative update method, similar to the through-hole testing specimens. For the 23 J and 28 J impact specimens, the optimum baseline conductivities were found to be $\sigma_{x0} = \sigma_{y0} = 0.055$ S/m and $\sigma_{z0} = 5 \times 10^{-4}$ S/m. For the 25 J impact specimen, the optimum baseline conductivities were found to be $\sigma_{x0} = \sigma_{y0} = 0.02$ S/m and $\sigma_{z0} = 3 \times 10^{-4}$ S/m.

The EIT conductivity change obtained by solving equation (6.5) for each impact case is shown in the first (top) row in Figure 6.19. It can be seen that EIT is able to detect the damage due to each impact. Furthermore, as the impact energy increases, the magnitude of the conductivity change in the impacted region also increases. This indicates that damage in the material is increasing as the impact energy increases. However, the precise size of the impact-induced delamination cannot be immediately determined from the EIT conductivity change.

In order to precisely compute delamination size from the EIT conductivity changes, the metaheuristic algorithm-enabled damage shaping problem was solved using the GA. For this, recall that a geometric model for delaminations was developed earlier. In order to integrate this model with the GA and to make it applicable to a FE analysis, 3-D FE models of each laminate were set up. Each model was assigned the optimum baseline conductivities (σ_{x0}, σ_{y0}, and σ_{z0}) determined earlier. Note that instead of modeling an individual laminate as composed of multiple layers with anisotropic conductivity, each laminate has been modeled as an effective or homogenized material with the same bulk conductive properties as the actual laminate. Each FE model used a layer of quadrilateral elements sandwiched between two layers of hexahedral elements. The quadrilateral element layer is the FE equivalent of the 'interface' layer shown in Figure 4.7. The GA was then used to generate elliptical conductivity artifacts described by $s_m = [x_c, y_c, r_x, r_y]$ inside the interface layer. The artifact

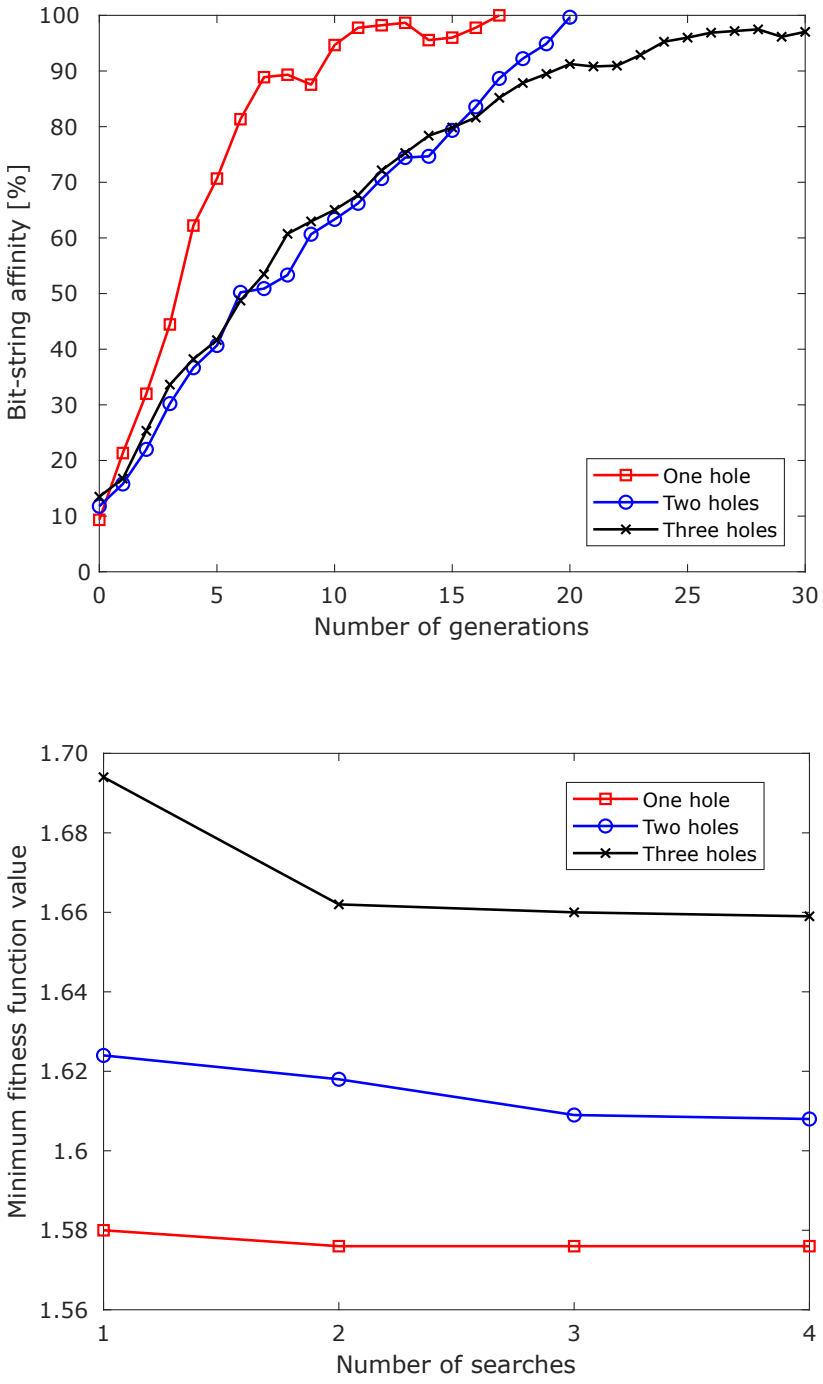

Figure 6.15. Top: BSA convergence for the first search of each case. Bottom: Fitness function convergence for all searches of each case.

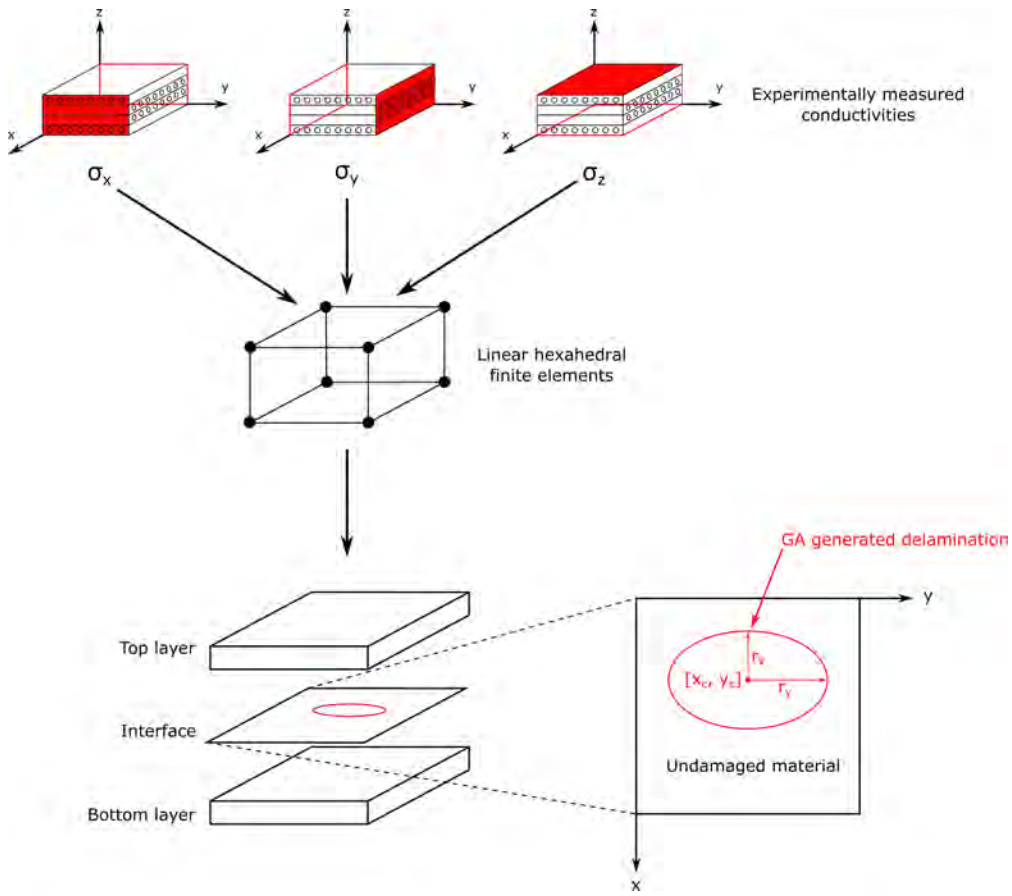

Figure 6.16. Schematic of delamination modeling process for GA-enabled precise damage shaping. The experimentally measured baseline conductivities are used to construct 3-D FE models of each laminate using linear hexahedral elements. The middle layer of the mesh is then collapsed to infinitesimal thickness, to represent an interface at the mid-plane of the laminate. The GA then generates elliptical conductivity artifacts inside this interface layer.

was assigned a uniform a conductivity of $\sigma_x = \sigma_y = \sigma_z = \sigma_d = 1 \times 10^{-6}$ S/m. A schematic of the delamination modeling process is shown in Figure 6.16. For the GA, a population size of 20, a BSA stopping criterion of 65%, and a maximum of 20 generations were used. A lower BSA stopping criterion than the through-hole shaping problem was used because it was observed that the fitness function attains its minimum value at a relatively low BSA. Therefore, trying to achieve a higher BSA only adds computational cost. The delamination shapes in the interface layer reconstructed using the GA are shown in the second row in Figure 6.19.

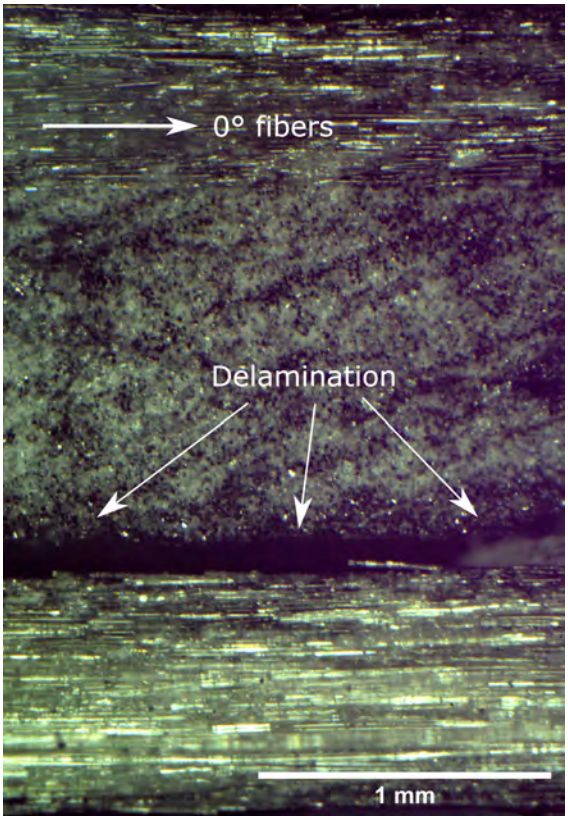

Figure 6.17. Optical micrograph of cross-section of 23 J impact specimen. A delamination is clearly visible between the third (0°) and fourth (90°) layers. The fibers in the 90° layers are pointing out of the page.

Optical microscopy was performed to measure the delamination size in each laminate. Figure 6.17 shows a representative optical micrograph of the cross-section of the 23 J impact laminate. A delamination can clearly be seen between the third (0°) and fourth (90°) layers. In fact, for all impact cases it was observed that the delamination occurred between the third and fourth layers. The complete delamination shape was reconstructed by making several cuts through each laminate using a water-cooled tile saw and measuring the delamination length at each exposed cross-section using the microscope. The measured delamination lengths and cut thicknesses were then used to reconstruct the in-plane shape of the delamination. This process is illustrated for a single cut in Figure 6.18 and the reconstructed delamination shapes are shown in the third row in Figure 6.19.

It can be immediately observed from Figure 6.19 that the delamination shapes and sizes reconstructed using the GA agree very well with the delaminations measured using optical

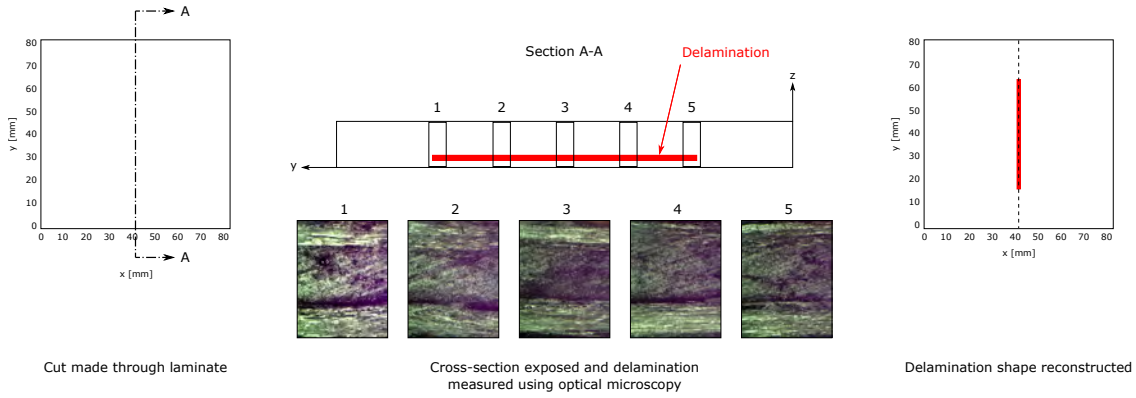

Figure 6.18. Schematic of delamination shape reconstruction for a single cut using optical microscopy. A cut is made through the laminate (left) and the cross-section is exposed. Optical microscopy is used to record the delamination length along the cross-section (center) and several optical micrographs are taken. The delamination length and cut thickness are used to piece together the delamination shape (right). This process is repeated for multiple cuts to reconstruct the full delamination shape in the specimen.

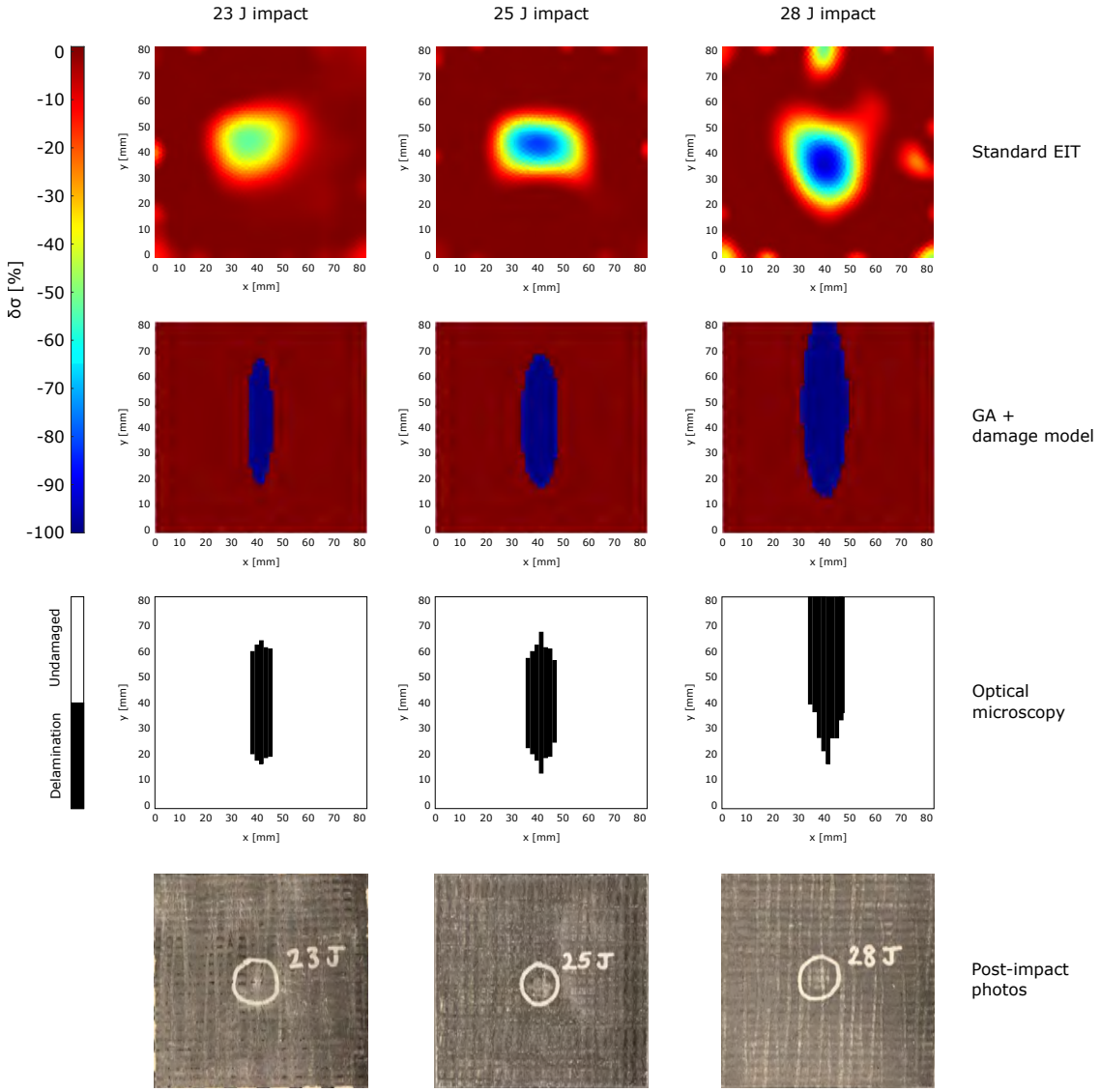

Figure 6.19. EIT, GA-enabled damage shaping, and optical microscopy results. First (top) row: EIT conductivity change. Second row: GA-generated delamination shapes in the interface layer. Third row: Actual delamination shapes reconstructed using optical microscopy. Bottom row: Post-impact photos of specimens. The impact locations are indicated by the silver circles.

microscopy. As the impact energy increases, the size of the delamination also increases and the GA is able to capture the growth of the delamination very well. There are minor differences between the GA-generated shapes and the actual delamination shapes. This difference occurs because an impact does not cause a pure delamination. Instead, a combination of failure modes exist in the material such as matrix cracking and fiber breakage. However, the metaheuristic algorithm-enabled inversion does not capture all of these modes and, therefore, compensates for the additional damage by artificially increasing the size of the delamination. Despite this, the GA-generated delaminations provide much more insight into the underlying mechanics of the material than standard EIT.

Lastly, the convergence of the GA-enabled delamination shaping problem can be studied in Figures 6.20 and 6.21. The fitness function for the first search of each impact case, shown in Figure 6.20, attains an optimal value at a small number of generations. Furthermore, from Figure 6.21, the change in the minimum fitness function value is very small for repeated searches, indicating that there is no significant improvement in the solution and successive searches are not necessary to produce a good quality solution.

6.4 Summary

This chapter presented the results from three main analyses performed in this thesis: i) metaheuristic algorithm-enabled piezoresistive inversion, ii) a comparison of metaheuristic algorithms for solving the piezoresistive inversion problem, and iii) metaheuristic algorithm-enabled precise damage shaping.

The metaheuristic algorithm-enabled piezoresistive inversion problem was solved for an elastically deformed CNF-modified polymer nanocomposite. EIT was used to image the conductivity change in the nanocomposite and it was shown that strain concentrations manifest as marked changes in the local conductivity of the material. The precise underlying displacements, strains, and stresses were then recovered from the EIT-imaged conductivity changes using a GA integrated with an analytical piezoresistivity model. The inversely computed mechanical state of the material was validated by comparison with standard FE simulations

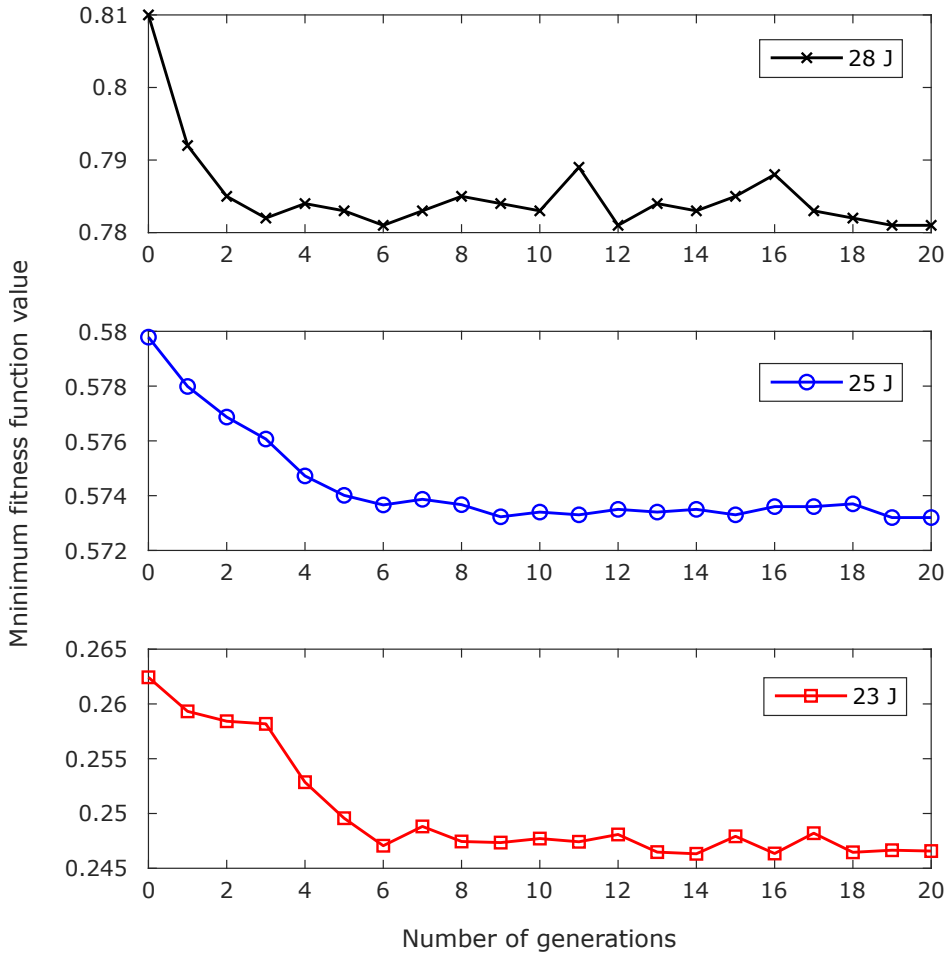

Figure 6.20. Fitness function convergence for first search of each impact case.

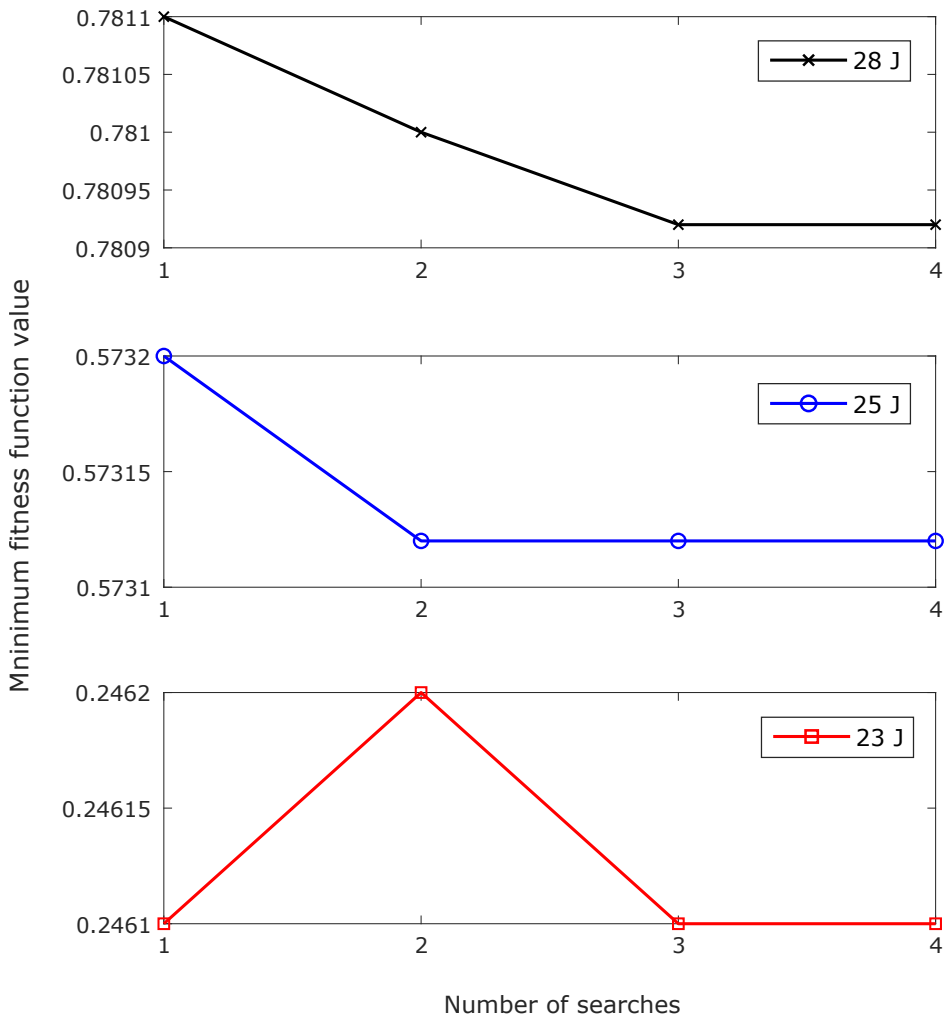

Figure 6.21. Minimum fitness function convergence for all searches of each impact case.

and DIC measurements, and it was shown that this technique can be used to accurately predict structural failure.

Next, a comparison was drawn between three algorithms for solving the piezoresistive inversion problem – GA, SA, and PSO. The solution quality, variability for multiple searches, accuracy relative to standard FEM, and the efficiency of each algorithm were evaluated. It was determined that the GA had the best solution quality, the smallest variation for multiple searches, the lowest percent error, and the highest efficiency, and was therefore the best algorithm for solving the piezoresistive inversion problem.

Finally, the metaheuristic algorithm-enabled precise damage shaping problem was solved on CNF-modified GFRP nanocomposite laminates. Two specific damage cases were considered – through-holes and impact-induced delaminations. For the through-hole testing specimens, EIT was able to detect the presence of the holes. A GA was then integrated with the previously developed geometric model for through-holes via an adaptive meshing algorithm and used to reconstruct the precise shape and size of the through-holes. The results showed good agreement with the actual hole sizes and locations. For the impact testing specimens, EIT was able to detect the impact damage but did not provide precise information about the delamination shape or size. For this, the GA was integrated with the geometric model for delaminations developed previously. 3-D FE models of each laminate were constructed and the middle layer of elements was collapsed to infinitesimal thickness to represent an interface. The GA was then used to find the optimum shape of an elliptical conductivity artifact inside this interface layer for each impact case. The delamination shaping results showed excellent agreement with the actual delamination shapes obtained using optical microscopy.

7. SUMMARY OF SCHOLARLY CONTRIBUTIONS

This chapter provides a summary of the major scholarly contributions of this thesis and discusses their impact in the broader context of self-sensing SHM. The overarching goal of this work was to develop and validate methodologies for solving conductivity-to-mechanics inverse problems using metaheuristic algorithms. This research was motivated by the fact that current state-of-the-art self-sensing SHM is limited in that it provides little-to-no information about the precise mechanical state of a structure. This information must be ascertained by solving conductivity-to-mechanics inverse problems. These problems are challenging but extremely important because conductivity is generally not a SHM-relevant property. Instead, it would be much more beneficial to know, for example, the pressure distribution in a tactile sensor, the displacement of a prosthetic implant, or the deflection of a bridge or an aircraft wing. In light of this limitation, this thesis makes three important contributions toward solving conductivity-to-mechanics inverse problems, as summarized in the following sections.

7.1 Metaheuristic Algorithm-Enabled Piezoresistive Inversion

The first major goal of this thesis was to develop a methodology for determining the displacements, strains, and stresses in self-sensing composites using observed conductivity changes. This is an under-determined inverse problem because conductivity is generally described as a single-valued scalar while strain has six independent components. Furthermore, because piezoresistivity is driven primarily by the first principal strains, the relation between conductivity and strain is not one-to-one. That is, multiple strain states can give rise to the same observed conductivity change. As such, in order to solve the piezoresistive inversion problem, a metaheuristic global search algorithm is required. Furthermore, to ensure mechanically feasible solutions, the metaheuristic algorithm must be integrated with a physics-based piezoresistivity model. This thesis mathematically formulates this methodology and experimentally solves the piezoresistive inversion problem using a GA on a self-sensing polymer nanocomposite.

This is an important contribution to the state of the art because, previously, gradient-based optimization techniques have been used to solve the piezoresistive inversion problem

[132], [133]. The applicability of these techniques, while efficient and elegant, is limited to loading scenarios where the actual solution is relatively 'close' to the initial estimate. The methodology proposed here addresses this limitation because it incorporates a global search algorithm. As such, this technique can accurately determine the underlying displacements, strains, and stresses for general loading scenarios and can even be used to predict failure. The impact of this is far reaching and diverse. For example, knowing the conductivity distribution in a wearable electronic sensor, the exact pressure distribution in the sensor can be inversely determined. Similarly, the conductivity change in a aircraft wing deflected in-flight can be used to precisely determine the stresses and predict when and where failure is likely to occur. Furthermore, while this technique has been explored for self-sensing composites in this thesis, its applicability can be easily extended to other engineering venues and to a wide array of self-sensing material systems such as cements [51], concrete [49], ceramics [149], and polymer-based sensing skins [150] and paints [151].

7.2 A Comparison of Metaheuristic Algorithms for Piezoresistive Inversion

Having solved the piezoresistive inversion problem using a GA, the second major goal of this thesis was to explore other metaheuristic algorithms and compare their performances to that of the GA. This was motivated by the fact that integrating a GA with a linear elasticity BVP via the FE method and an analytical piezoresistivity model is computationally expensive. Additionally, the inversely recovered strains and stresses showed minor artifacts due to the variability in the GA-generated displacement boundary conditions. It was postulated that other metaheuristic algorithms may provide better quality solutions with higher efficiency. To that end, two algorithms were used to solve the previous piezoresistive inversion problem —SA and PSO —and a comparison was drawn in terms of solution quality, variability, accuracy, and efficiency. Both SA and PSO were able to produce good quality displacement solutions but still exhibited strain artifacts due to large inter-node displacement variability. It was observed that the GA had the fewest strain artifacts, the smallest variability in nodal displacements, the highest accuracy, and was also the most efficient algorithm in terms of producing the lowest fitness function value in the shortest run-time.

Despite the impressive performance of the GA, this work demonstrates that good quality solutions for piezoresistive inversion problems can be obtained using other widely available and well-known metaheuristic algorithms.

7.3 Metaheuristic Algorithm-Enabled Precise Damage Shaping

The third major goal of this thesis was to develop a methodology for precisely determining the shape and size of specific damage modes in self-sensing composites using observed conductivity changes. This is important because knowing the damage state, especially for sub-surface or outwardly invisible damages, is often more critical to the safety of composite structures than just the strain field. This is a challenging inverse problem because no well-defined mathematical relationship exists between damage geometry (shape and size) and material conductivity. Therefore, gradient-based optimization schemes are not applicable and metaheuristic algorithms are needed. Furthermore, geometric models that realistically describe how specific damage modes affect material conductivity are also required to ensure physically meaningful solutions. This thesis first develops mechanics-inspired geometric models for two specific damage modes: through-holes and delaminations. Next, the metaheuristic-algorithm enabled precise damage shaping problem is mathematically formulated and integrated with the damage models. A GA is then used to solve the precise damage shaping problem on self-sensing composite laminates to recover the precise shape and size of through-holes and delaminations.

This is an important advancement to the state of the art because prevailing conductivity-based health monitoring provides no information about the underlying damage mechanisms and shapes. From a NDE perspective, knowing the exact mechanism and size of damage within a structure is crucial. For example, if the exact size and location of a delamination within a composite airframe can be determined, the structure can either be repaired immediately or taken out of service to avert catastrophic failure. Similarly, the health of a bridge or a wind turbine blade can be accurately prognosticated by knowing the condition of damage within the structure. This methodology contributes significantly toward the goal

of improving the safety of high-risk engineering structures by enabling spatially continuous, precise damage characterization.

8. RECOMMENDATIONS FOR FUTURE WORK

The methodologies developed in this thesis are the first ever comprehensive effort to solve conductivity-to-mechanics inverse problems in self-sensing materials. Although these techniques are effective and powerful, they do have certain limitations and there is room for improvement. Furthermore, this new and incredibly challenging subject has immense potential for advancing SHM and there are numerous areas for future research endeavors. This chapter identifies some of the limitations of this thesis and also identifies areas where future research can make significant contributions. Possible pathways for addressing these limitations and for solving future problems are also delineated.

1. **Solve inverse mechanics problems in other material systems**: The metaheuristic algorithm-enabled piezoresistive inversion and precise damage shaping methodologies developed herein are robust because they can easily be extended to different material systems and loading scenarios. Therefore, future research should aim to solve these problems on large, civil-inspired structures incorporating cementitious piezoresistive materials [50], [98], biomedical materials such as those used in self-sensing prosthetic implants [152], flexible tactile sensors such as wearable electronics [153], and even micro-scale systems such as biological tissue [154]. Furthermore, for these problems it would be more efficient to integrate resistivity-strain relations [44], [139] rather than analytical piezoresistivity models with suitable inversion techniques.

2. **Develop mechanics-based metaheuristic algorithms to improve efficiency**: The GA, SA, and PSO used in this thesis were by no means optimized for solving inverse mechanics problems. The parameters used for each algorithm were carefully selected to give the best performance but the computational burden of using global search algorithms was still significant. As such, one possible avenue of future research is to develop metaheuristic algorithms with inherent features/programming that make them more amenable to mechanics problems. This may also circumvent the need to use high-performance computing architecture to solve complex problems with a large number of unknowns. Furthermore, hybrid optimization techniques that aug-

ment metaheuristic algorithms with gradient-based methods should also be explored to improve efficiency.

3. **Develop geometric models for other damage modes**: This thesis considered two specific damage models for solving the precise damage shaping problem: through-holes and delaminations. Future research should work toward developing and experimentally validating geometric models for other damage modes. This is because composites do not generally experience one specific damage mode. Instead, it is well understood that a complex combination of delamination, matrix cracking, and fiber breakage can occur in realistic structural scenarios. Therefore, it is necessary to integrate realistic physics for all these damage modes with suitable inversion algorithms. As such, one possible avenue of future research is to develop universal damage models that can capture realistic physics of multiple damage mechanisms and integrate these models with suitable inversion algorithms for complete damage characterization in self-sensing materials.

4. **Extend damage shaping methodology to complex shapes**: The precise damage shaping methodology developed herein used parametric representations of damage geometry. Specifically, through-holes were parameterized as circles and delaminations were parameterized as ellipses. Although these parameterizations were physics-informed and similar descriptions exist in prevailing literature [142]–[145], shapes for failure modes in realistic loading scenarios are generally more complex than circles and ellipses. Therefore, future work should develop geometric damage models that incorporate complex shapes. For general polygons, this might involve applying concepts from topology optimization.

5. **Develop machine learning-based methods for solving conductivity-to-mechanics inverse problems**: Machine learning-based methods such as artificial neural networks (ANNs) have recently been explored for precise damage characterization using EIT-imaged conductivity changes in self-sensing materials [155], [156]. These methods have incredible potential for solving conductivity-to-mechanics inverse prob-

lems but they require copious training data in to achieve good accuracy. Therefore, a promising avenue of future work is to develop and experimentally validate ANNs for solving piezoresistive inversion and precise damage shaping in self-sensing materials.

REFERENCES

[1] C. R. Farrar and K. Worden, "An Introduction to Structural Health Monitoring," *New Trends in Vibration Based Structural Health Monitoring*, pp. 1–17, 2010.

[2] F.-K. Chang, J. F. Markmiller, J. Yang, and Y. Kim, "Structural Health Monitoring," *System Health Management: with Aerospace Applications*, pp. 419–428, 2011.

[3] H. Sohn, C. R. Farrar, F. M. Hemez, D. D. Shunk, D. W. Stinemates, B. R. Nadler, and J. J. Czarnecki, "A Review of Structural Health Monitoring Literature: 1996–2001," *Los Alamos National Laboratory, USA*, vol. 1, 2003.

[4] D. Balageas, C.-P. Fritzen, and A. Güemes, *Structural Health Monitoring*. John Wiley & Sons, 2010, vol. 90.

[5] E. Guillen, "Investigation launched into 'serious' Airbus A380 engine failure," *NBC News*, Oct. 1, 2017. [Online]. Available: https://www.nbcnews.com/storyline/airplane-mode/investigation-launched-serious-airbus-a380-engine-failure-n806301.

[6] Reuters, "Death toll rises in Taiwan bridge collapse," *Deutsche Welle*, Feb. 2, 2019. [Online]. Available: https://www.dw.com/en/death-toll-rises-in-taiwan-bridge-collapse/a-50652949.

[7] D. Montalvao, N. M. M. Maia, and A. M. R. Ribeiro, "A Review of Vibration-Based Structural Health Monitoring with Special Emphasis on Composite Materials," *Shock and Vibration Digest*, vol. 38, no. 4, pp. 295–324, 2006.

[8] A. Deraemaeker and K. Worden, *New Trends in Vibration Based Structural Health Monitoring*. Springer Science & Business Media, 2012, vol. 520.

[9] C. P. Fritzen, "Vibration-based Structural Health Monitoring – Concepts and Applications," in *Key Engineering Materials*, Trans Tech Publ, vol. 293, 2005, pp. 3–20.

[10] C. R. Farrar, S. W. Doebling, and D. A. Nix, "Vibration–Based Structural Damage Identification," *Philosophical Transactions of the Royal Society of London. Series A: Mathematical, Physical and Engineering Sciences*, vol. 359, no. 1778, pp. 131–149, 2001.

[11] Z. Zhang, K. Shankar, E. V. Morozov, and M. Tahtali, "Vibration-Based Delamination Detection in Composite Beams Through Frequency Changes," *Journal of Vibration and Control*, vol. 22, no. 2, pp. 496–512, 2016.

[12] R. Janeliukstis, S. Rucevskis, M. Wesolowski, and A. Chate, "Experimental Structural Damage Localization in Beam Structure Using Spatial Continuous Wavelet Transform and Mode Shape Curvature Methods," *Measurement*, vol. 102, pp. 253–270, 2017.

[13] S. Khatir, A. Behtani, S. Tiachacht, A. Bouazouni, M. A. Wahab, and Y. Zhou, "Delamination Detection in Laminated Composite Using Virtual Crack Closure Technique (VCCT) and Modal Flexibility Based on Dynamic Analysis," in *Journal of Physics: Conference Series*, IOP Publishing, vol. 842, 2017, p. 012 084.

[14] M. Mitra and S. Gopalakrishnan, "Guided Wave Based Structural Health Monitoring: A Review," *Smart Materials and Structures*, vol. 25, no. 5, p. 053 001, 2016.

[15] A. Raghavan, "Guided-Wave Structural Health Monitoring," PhD thesis, 2007.

[16] A. J. Croxford, P. D. Wilcox, B. W. Drinkwater, and G. Konstantinidis, "Strategies for Guided-Wave Structural Health Monitoring," *Proceedings of the Royal Society A: Mathematical, Physical and Engineering Sciences*, vol. 463, no. 2087, pp. 2961–2981, 2007.

[17] V. Memmolo, E. Monaco, N. Boffa, L. Maio, and F. Ricci, "Guided Wave Propagation and Scattering for Structural Health Monitoring of Stiffened Composites," *Composite Structures*, vol. 184, pp. 568–580, 2018.

[18] M. H. Sherafat, R. Guitel, N. Quaegebeur, P. Hubert, L. Lessard, and P. Masson, "Structural Health Monitoring of a Composite Skin-Stringer Assembly Using Within-the-Bond Strategy of Guided Wave Propagation," *Materials & Design*, vol. 90, pp. 787–794, 2016.

[19] S. K. Chakrapani and V. Dayal, "The Interaction of Rayleigh Waves with Delaminations in Composite Laminates," *The Journal of the Acoustical Society of America*, vol. 135, no. 5, pp. 2646–2653, 2014. DOI: 10.1121/1.4869684.

[20] J. dos Reis, C. Oliveira Costa, and J. Sá da Costa, "Strain Gauges Debonding Fault Detection for Structural Health Monitoring," *Structural Control and Health Monitoring*, vol. 25, no. 12, e2264, 2018.

[21] S. Takeda, Y. Aoki, T. Ishikawa, N. Takeda, and H. Kikukawa, "Structural Health Monitoring of Composite Wing Structure During Durability Test," *Composite Structures*, vol. 79, no. 1, pp. 133–139, 2007.

[22] H. Choi, S. Choi, and H. Cha, "Structural Health Monitoring System Based on Strain Gauge Enabled Wireless Sensor Nodes," in *2008 5th International Conference on Networked Sensing Systems*, IEEE, 2008, pp. 211–214.

[23] G. Park, H. Sohn, C. R. Farrar, D. J. Inman, *et al.*, "Overview of Piezoelectric Impedance-Based Health Monitoring and Path Forward," *Shock and Vibration Digest*, vol. 35, no. 6, pp. 451–464, 2003.

[24] V. Giurgiutiu, *Structural Health Monitoring: with Piezoelectric Wafer Active Sensors*. Elsevier, 2007.

[25] V. Giurgiutiu, A. Zagrai, and J. Jing Bao, "Piezoelectric Wafer Embedded Active Sensors for Aging Aircraft Structural Health Monitoring," *Structural Health Monitoring*, vol. 1, no. 1, pp. 41–61, 2002.

[26] G. Park and D. J. Inman, "Structural Health Monitoring using Piezoelectric Impedance Measurements," *Philosophical Transactions of the Royal Society A: Mathematical, Physical and Engineering Sciences*, vol. 365, no. 1851, pp. 373–392, 2007.

[27] H.-N. Li, D.-S. Li, and G.-B. Song, "Recent Applications of Fiber Optic Sensors to Health Monitoring in Civil Engineering," *Engineering Structures*, vol. 26, no. 11, pp. 1647–1657, 2004.

[28] J. M. López-Higuera, L. R. Cobo, A. Q. Incera, and A. Cobo, "Fiber Optic Sensors in Structural Health Monitoring," *Journal of Lightwave Technology*, vol. 29, no. 4, pp. 587–608, 2011.

[29] A. Güemes, A. Fernández-López, P. F. Díaz-Maroto, A. Lozano, and J. Sierra-Perez, "Structural Health Monitoring in Composite Structures by Fiber-Optic Sensors," *Sensors*, vol. 18, no. 4, p. 1094, 2018.

[30] H. Guo, G. Xiao, N. Mrad, and J. Yao, "Fiber Optic Sensors for Structural Health Monitoring of Air Platforms," *Sensors*, vol. 11, no. 4, pp. 3687–3705, 2011.

[31] M. Ramakrishnan, G. Rajan, Y. Semenova, and G. Farrell, "Overview of Fiber Optic Sensor Technologies for Strain/Temperature Sensing Applications in Composite Materials," *Sensors*, vol. 16, no. 1, p. 99, 2016.

[32] G. Zhou and L. Sim, "Damage Detection and Assessment in Fibre-Reinforced Composite Structures with Embedded Fibre Optic Sensors-Review," *Smart Materials and Structures*, vol. 11, no. 6, p. 925, 2002.

[33] S. Zike and L. P. Mikkelsen, "Correction of Gauge Factor for Strain Gauges used in Polymer Composite Testing," *Experimental Mechanics*, vol. 54, no. 3, pp. 393–403, 2014.

[34] J. Vitola, F. Pozo, D. A. Tibaduiza, and M. Anaya, "Distributed Piezoelectric Sensor System for Damage Identification in Structures Subjected to Temperature Changes," *Sensors*, vol. 17, no. 6, p. 1252, 2017.

[35] M. Wevers, L. Rippert, J.-M. Papy, and S. Van Huffel, "Processing of Transient Signals from Damage in CFRP Composite Materials Monitored with Embedded Intensity-Modulated Fiber Optic Sensors," *Ndt & E International*, vol. 39, no. 3, pp. 229–235, 2006.

[36] M. E. Efimov, M. Y. Plotnikov, A. V. Kulikov, M. V. Mekhrengin, and A. Y. Kireenkov, "Fiber-Optic Interferometric Sensor Based on the Self-Interference Pulse Interrogation Approach for Acoustic Emission Sensing in the Graphite/Epoxy Composite," *IEEE Sensors Journal*, vol. 19, no. 18, pp. 7861–7867, 2019.

[37] S. Jothibasu, Y. Du, S. Anandan, G. S. Dhaliwal, A. Kaur, S. E. Watkins, K. Chandrashekhara, and J. Huang, "Strain Monitoring Using Distributed Fiber Optic Sensors Embedded in Carbon Fiber Composites," in *Sensors and Smart Structures Technologies for Civil, Mechanical, and Aerospace Systems 2018*, International Society for Optics and Photonics, vol. 10598, 2018, p. 105980I.

[38] H. Wang and J.-G. Dai, "Strain Transfer Analysis of Fiber Bragg Grating Sensor Assembled Composite Structures Subjected to Thermal Loading," *Composites Part B: Engineering*, vol. 162, pp. 303–313, 2019.

[39] K. Shivakumar and L. Emmanwori, "Mechanics of Failure of Composite Laminates with an Embedded Fiber Optic Sensor," *Journal of Composite Materials*, vol. 38, no. 8, pp. 669–680, 2004.

[40] A. Fedorov, N. Kosheleva, V. Matveenko, and G. Serovaev, "Strain Measurement and Stress Analysis in the Vicinity of a Fiber Bragg Grating Sensor Embedded in a Composite Material," *Composite Structures*, vol. 239, p. 111 844, 2020.

[41] D. D. L. Chung, "Carbon Materials for Structural Self-sensing, Electromagnetic Shielding and Thermal Interfacing," *Carbon*, vol. 50, no. 9, pp. 3342–3353, 2012.

[42] T. N. Tallman, S. Gungor, K. W. Wang, and C. E. Bakis, "Tactile Imaging and Distributed Strain Sensing in Highly Flexible Carbon Nanofiber/Polyurethane Nanocomposites," *Carbon*, vol. 95, pp. 485–493, 2015.

[43] S. Rana, P. Subramani, R. Fangueiro, and A. G. Correia, "A Review on Smart Self-Sensing Composite Materials for Civil Engineering Applications," *AIMS Materials Science*, vol. 3, no. 2, pp. 357–379, 2016.

[44] G. M. Koo and T. N. Tallman, "Higher-Order Resistivity-Strain Relations for Self-Sensing Nanocomposites Subject to General Deformations," *Composites Part B: Engineering*, vol. 190, p. 107 907, 2020.

[45] G. M. Koo and T. N. Tallman, "Frequency-Dependent Alternating Current Piezoresistive Switching Behavior in Self-Sensing Carbon Nanofiber Composites," *Carbon*, vol. 173, pp. 384–394, 2021.

[46] E. T. Thostenson and T.-W. Chou, "Carbon Nanotube Networks: Sensing of Distributed Strain and Damage for Life Prediction and Self Healing," *Advanced Materials*, vol. 18, no. 21, pp. 2837–2841, 2006.

[47] E. T. Thostenson and T.-W. Chou, "Real-Time In Situ Sensing of Damage Evolution in Advanced Fiber Composites Using Carbon Nanotube Networks," *Nanotechnology*, vol. 19, no. 21, p. 215 713, 2008.

[48] B. Han, X. Yu, and J. Ou, *Self-Sensing Concrete in Smart Structures*. Butterworth-Heinemann, 2014.

[49] Z. Tian, Y. Li, J. Zheng, and S. Wang, "A State-of-the-Art on Self-Sensing Concrete: Materials, Fabrication and Properties," *Composites Part B: Engineering*, vol. 177, p. 107 437, 2019.

[50] S. Gupta, J. G. Gonzalez, and K. J. Loh, "Self-Sensing Concrete Enabled by Nano-Engineered Cement-Aggregate Interfaces," *Structural Health Monitoring*, vol. 16, no. 3, pp. 309–323, 2017.

[51] A. O. Monteiro, P. B. Cachim, and P. M. Costa, "Self-Sensing Piezoresistive Cement Composite Loaded with Carbon Black Particles," *Cement and Concrete Composites*, vol. 81, pp. 59–65, 2017.

[52] R. Riedel, L. Toma, E. Janssen, J. Nuffer, T. Melz, and H. Hanselka, "Piezoresistive Effect in siOC Ceramics for Integrated Pressure Sensors," *Journal of the American Ceramic Society*, vol. 93, no. 4, pp. 920–924, 2010.

[53] M. Zarnik, D. Belavic, K. P. Friedel, and A. Wymyslowski, "A Procedure for Validating the Finite Element Model of a Piezoresistive Ceramic Pressure Sensor," *IEEE Transactions on Components and Packaging Technologies*, vol. 27, no. 4, pp. 668–675, 2004.

[54] L. Du, Z. Zhao, L. Xiao, Z. Fang, Q. Tian, X. Sun, and X. Wang, "Nickel–Chromium Alloy Piezoresistive Pressure Sensor Using Eutectic Bonding," *Micro & Nano Letters*, vol. 7, no. 12, pp. 1184–1188, 2012.

[55] X. Shi, C.-H. Cheng, C. Chao, L. Wang, and Y. Zheng, "A Piezoresistive Normal and Shear Force Sensor Using Liquid Metal Alloy as Gauge Material," in *2012 7th IEEE International Conference on Nano/Micro Engineered and Molecular Systems (NEMS)*, IEEE, 2012, pp. 483–486.

[56] H. Chiriac, M. Urse, F. Rusu, C. Hison, and M. Neagu, "Ni–Ag Thin Films as Strain-Sensitive Materials for Piezoresistive Sensors," *Sensors and Actuators A: Physical*, vol. 76, no. 1-3, pp. 376–380, 1999.

[57] C. M. Murray, S. M. Doshi, D. H. Sung, and E. T. Thostenson, "Hierarchical Composites with Electrophoretically Deposited Carbon Nanotubes for In Situ Sensing of Deformation and Damage," *Nanomaterials*, vol. 10, no. 7, p. 1262, 2020.

[58] F. Panozzo, M. Zappalorto, L. Maragoni, S. K. Nothdurfter, A. Rullo, and M. Quaresimin, "Modelling the Electrical Resistance Change in a Multidirectional Laminate with a Delamination," *Composites Science and Technology*, vol. 162, pp. 225–234, 2018.

[59] C. Li and T.-W. Chou, "Modeling of Damage Sensing in Fiber Composites Using Carbon Nanotube Networks," *Composites Science and Technology*, vol. 68, no. 15-16, pp. 3373–3379, 2008.

[60] Y. Wang, Y. Wang, B. Wan, B. Han, G. Cai, and Z. Li, "Properties and Mechanisms of Self-Sensing Carbon Nanofibers/Epoxy Composites for Structural Health Monitoring," *Composite Structures*, vol. 200, pp. 669–678, 2018.

[61] R. B. Ladani, S. Wu, A. J. Kinloch, K. Ghorbani, A. P. Mouritz, and C. H. Wang, "Enhancing Fatigue Resistance and Damage Characterisation in Adhesively-Bonded Composite Joints by Carbon Nanofibres," *Composites Science and Technology*, vol. 149, pp. 116–126, 2017.

[62] L. Vertuccio, L. Guadagno, G. Spinelli, P. Lamberti, V. Tucci, and S. Russo, "Piezoresistive Properties of Resin Reinforced with Carbon Nanotubes for Health-Monitoring of Aircraft Primary Structures," *Composites Part B: Engineering*, vol. 107, pp. 192–202, 2016.

[63] S. Nag-Chowdhury, H. Bellegou, I. Pillin, M. Castro, P. Longrais, and J. Feller, "Non-Intrusive Health Monitoring of Infused Composites with Embedded Carbon Quantum Piezo-Resistive Sensors," *Composites Science and Technology*, vol. 123, pp. 286–294, 2016.

[64] X. Du, H. Zhou, W. Sun, H.-Y. Liu, G. Zhou, H. Zhou, and Y.-W. Mai, "Graphene/Epoxy Interleaves for Delamination Toughening and Monitoring of Crack Damage in Carbon Fibre/Epoxy Composite Laminates," *Composites Science and Technology*, vol. 140, pp. 123–133, 2017.

[65] S.-J. Joo, M.-H. Yu, W. S. Kim, and H.-S. Kim, "Damage Detection and Self-Healing of Carbon Fiber Polypropylene (CFPP)/Carbon Nanotube (CNT) Nano-Composite via Addressable Conducting Network," *Composites Science and Technology*, vol. 167, pp. 62–70, 2018.

[66] H. Dai, E. T. Thostenson, and T. Schumacher, "Processing and Characterization of a Novel Distributed Strain Sensor Using Carbon Nanotube-Based Nonwoven Composites," *Sensors*, vol. 15, no. 7, pp. 17 728–17 747, 2015.

[67] G. Georgousis, C. Pandis, A. Kalamiotis, P. Georgiopoulos, A. Kyritsis, E. Kontou, P. Pissis, M. Micusik, K. Czanikova, J. Kulicek, *et al.*, "Strain Sensing in Polymer/Carbon Nanotube Composites by Electrical Resistance Measurement," *Composites Part B: Engineering*, vol. 68, pp. 162–169, 2015.

[68] J. Sebastian, N. Schehl, M. Bouchard, M. Boehle, L. Li, A. Lagounov, and K. Lafdi, "Health Monitoring of Structural Composites with Embedded Carbon Nanotube Coated Glass Fiber Sensors," *Carbon*, vol. 66, pp. 191–200, 2014.

[69] A. Naghashpour and S. Van Hoa, "A Technique for Real-Time Detecting, Locating, and Quantifying Damage in Large Polymer Composite Structures made of Carbon Fibers and Carbon Nanotube Networks," *Structural Health Monitoring*, vol. 14, no. 1, pp. 35–45, 2015.

[70] A. Naghashpour and S. Van Hoa, "A Technique for Real-Time Detection, Location and Quantification of Damage in Large Polymer Composite Structures made of Electrically Non-Conductive Fibers and Carbon Nanotube Networks," *Nanotechnology*, vol. 24, no. 45, p. 455 502, 2013.

[71] C. Viets, S. Kaysser, and K. Schulte, "Damage Mapping of GFEP via Electrical Resistance Measurements Using Nanocomposite Epoxy Matrix Systems," *Composites Part B: Engineering*, vol. 65, pp. 80–88, 2014.

[72] D. Zhang, L. Ye, D. Wang, Y. Tang, S. Mustapha, and Y. Chen, "Assessment of Transverse Impact Damage in GF/EP Laminates of Conductive Nanoparticles Using Electrical Resistivity Tomography," *Composites Part A: Applied Science and Manufacturing*, vol. 43, no. 9, pp. 1587–1598, 2012.

[73] A. Kovalovs, S. Rucevskis, V. Kulakov, and M. Wesołowski, "Damage Detection in Carbon Fibre Reinforced Composites Using Electric Resistance Change Method," in *IOP Conference Series: Materials Science and Engineering*, IOP Publishing, vol. 471, 2019, p. 102 014.

[74] A. Kovalovs, "Numerical Analysis of Electrodes Position for Delamination Detection by Using Electric Resistance Change Method," in *IOP Conference Series: Materials Science and Engineering*, IOP Publishing, vol. 603, 2019, p. 032 090.

[75] A. Todoroki, Y. Tanaka, and Y. Shimamura, "Delamination Monitoring of Graphite/Epoxy Laminated Composite Plate of Electric Resistance Change Method," *Composites Science and Technology*, vol. 62, no. 9, pp. 1151–1160, 2002.

[76] A. Todoroki and Y. Tanaka, "Delamination Identification of Cross-Ply Graphite/Epoxy Composite Beams Using Electric Resistance Change Method," *Composites Science and Technology*, vol. 62, no. 5, pp. 629–639, 2002.

[77] A. Todoroki, M. Tanaka, and Y. Shimamura, "Measurement of Orthotropic Electric Conductance of CFRP Laminates and Analysis of the Effect on Delamination Monitoring with an Electric Resistance Change Method," *Composites Science and Technology*, vol. 62, no. 5, pp. 619–628, 2002.

[78] S. Gungor and C. E. Bakis, "Indentation Damage Detection in Glass/Epoxy Composite Laminates with Electrically Tailored Conductive Nanofiller," *Journal of Intelligent Material Systems and Structures*, vol. 27, no. 5, pp. 679–688, 2016.

[79] A. P. Calderón, "On an Inverse Boundary Value Problem," *Computational & Applied Mathematics*, pp. 2–3, 2006.

[80] T. de Castro Martins, A. K. Sato, F. S. de Moura, E. D. L. B. de Camargo, O. L. Silva, T. B. R. Santos, Z. Zhao, K. Möeller, M. B. P. Amato, J. L. Mueller, *et al.*, "A Review of Electrical Impedance Tomography in Lung Applications: Theory and Algorithms for Absolute Images," *Annual Reviews in Control*, vol. 48, pp. 442–471, 2019.

[81] V. Tomicic and R. Cornejo, "Lung Monitoring with Electrical Impedance Tomography: Technical Considerations and Clinical Applications," *Journal of Thoracic Disease*, vol. 11, no. 7, p. 3122, 2019.

[82] G. Hansen, T. Holt, and J. Dmytrowich, "Thoracic Electrical Impedance Tomography to Minimize Right Heart Strain Following Cardiac Arrest," *Annals of Pediatric Cardiology*, vol. 12, no. 3, p. 315, 2019.

[83] T. Tidswell, A. Gibson, R. H. Bayford, and D. S. Holder, "Three-Dimensional Electrical Impedance Tomography of Human Brain Activity," *NeuroImage*, vol. 13, no. 2, pp. 283–294, 2001.

[84] T. N. Tallman and D. J. Smyl, "Structural Health and Condition Monitoring via Electrical Impedance Tomography in Self-Sensing Materials: A Review," *Smart Materials and Structures*, vol. 29, no. 12, p. 123 001, Oct. 2020. DOI: 10.1088/1361-665x/abb352.

[85] H. Dai, G. J. Gallo, T. Schumacher, and E. T. Thostenson, "A Novel Methodology for Spatial Damage Detection and Imaging Using a Distributed Carbon Nanotube-Based Composite Sensor Combined with Electrical Impedance Tomography," *Journal of Nondestructive Evaluation*, vol. 35, no. 2, pp. 1–15, 2016.

[86] T. N. Tallman, S. Gungor, K. Wang, and C. E. Bakis, "Damage Detection via Electrical Impedance Tomography in Glass Fiber/Epoxy Laminates with Carbon Black Filler," *Structural Health Monitoring*, vol. 14, no. 1, pp. 100–109, 2015.

[87] T. N. Tallman, S. Gungor, K. W. Wang, and C. Bakis, "Damage Detection and Conductivity Evolution in Carbon Nanofiber Epoxy via Electrical Impedance Tomography," *Smart Materials and Structures*, vol. 23, no. 4, p. 045 034, 2014.

[88] A. Baltopoulos, N. Polydorides, L. Pambaguian, A. Vavouliotis, and V. Kostopoulos, "Damage Identification in Carbon Fiber Reinforced Polymer Plates Using Electrical Resistance Tomography Mapping," *Journal of Composite Materials*, vol. 47, no. 26, pp. 3285–3301, 2013.

[89] S. Nonn, M. Schagerl, Y. Zhao, S. Gschossmann, and C. Kralovec, "Application of Electrical Impedance Tomography to an Anisotropic Carbon Fiber-Reinforced Polymer Composite Laminate for Damage Localization," *Composites Science and Technology*, vol. 160, pp. 231–236, 2018.

[90] A. J. Thomas, J. J. Kim, T. N. Tallman, and C. E. Bakis, "Damage Detection in Self-Sensing Composite Tubes via Electrical Impedance Tomography," *Composites Part B: Engineering*, vol. 177, p. 107 276, 2019.

[91] T.-C. Hou, K. J. Loh, and J. P. Lynch, "Spatial Conductivity Mapping of Carbon Nanotube Composite Thin Films by Electrical Impedance Tomography for Sensing Applications," *Nanotechnology*, vol. 18, no. 31, p. 315 501, 2007.

[92] T.-C. Hou, K. J. Loh, and J. P. Lynch, "Electrical Impedance Tomography of Carbon Nanotube Composite Materials," in *Sensors and Smart Structures Technologies for Civil, Mechanical, and Aerospace Systems 2007*, International Society for Optics and Photonics, vol. 6529, 2007, p. 652 926.

[93] K. Loh, T.-C. Hou, J. Lynch, and N. Kotov, "Nanotube-Based Sensing Skins for Crack Detection and Impact Monitoring of Structures," in *Proceedings of the 6th International Workshop on Structural Health Monitoring, Stanford, CA, USA*, 2007, p. 16 851 692.

[94] K. J. Loh, T.-C. Hou, J. P. Lynch, and N. A. Kotov, "Spatial Structural Sensing by Carbon Nanotube-Based Skins," in *Sensors and Smart Structures Technologies for Civil, Mechanical, and Aerospace Systems 2008*, International Society for Optics and Photonics, vol. 6932, 2008, p. 693 207.

[95] K. J. Loh, T.-C. Hou, J. P. Lynch, and N. A. Kotov, "Carbon Nanotube Sensing Skins for Spatial Strain and Impact Damage Identification," *Journal of Nondestructive Evaluation*, vol. 28, no. 1, pp. 9–25, 2009.

[96] W. Lestari, B. Pinto, V. La Saponara, J. Yasui, and K. J. Loh, "Sensing Uniaxial Tensile Damage in Fiber-Reinforced Polymer Composites Using Electrical Resistance Tomography," *Smart Materials and Structures*, vol. 25, no. 8, p. 085 016, 2016.

[97] B. R. Loyola, V. La Saponara, K. J. Loh, T. M. Briggs, G. O'Bryan, and J. L. Skinner, "Spatial Sensing Using Electrical Impedance Tomography," *IEEE Sensors Journal*, vol. 13, no. 6, pp. 2357–2367, 2013.

[98] M. Hallaji, A. Seppänen, and M. Pour-Ghaz, "Electrical Impedance Tomography-Based Sensing Skin for Quantitative Imaging of Damage in Concrete," *Smart Materials and Structures*, vol. 23, no. 8, p. 085 001, 2014.

[99] M. Hallaji and M. Pour-Ghaz, "A New Sensing Skin for Qualitative Samage Detection in Concrete Elements: Rapid Difference Imaging with Electrical Resistance Tomography," *NDT & E International*, vol. 68, pp. 13–21, 2014.

[100] A. Seppänen, M. Hallaji, and M. Pour-Ghaz, "A Functionally Layered Sensing Skin for the Detection of Corrosive Elements and Cracking," *Structural Health Monitoring*, vol. 16, no. 2, pp. 215–224, 2017.

[101] D. Smyl, M. Pour-Ghaz, and A. Seppänen, "Detection and Reconstruction of Complex Structural Cracking Patterns with Electrical Imaging," *NDT & E International*, vol. 99, pp. 123–133, 2018.

[102] R. Harikumar, R. Prabu, and S. Raghavan, "Electrical Impedance Tomography (EIT) and its Medical Applications: A Review," *Int. J. Soft Comput. Eng*, vol. 3, no. 4, pp. 193–198, 2013.

[103] D. Nguyen, C. Jin, A. Thiagalingam, and A. McEwan, "A Review on Electrical Impedance Tomography for Pulmonary Perfusion Imaging," *Physiological measurement*, vol. 33, no. 5, p. 695, 2012.

[104] D. Silvera-Tawil, D. Rye, M. Soleimani, and M. Velonaki, "Electrical Impedance Tomography for Artificial Sensitive Robotic Skin: A Review," *IEEE Sensors Journal*, vol. 15, no. 4, pp. 2001–2016, 2014.

[105] T. Rymarczyk, P. Tchórzewski, K. Niderla, P. Adamkiewicz, and J. Sikora, "Electrical Tomography System for Acquisition and Monitoring of Geospatial Areas," in *2019 Applications of Electromagnetics in Modern Engineering and Medicine (PTZE)*, IEEE, 2019, pp. 188–192.

[106] O. L. Silva, R. G. Lima, T. C. Martins, F. S. de Moura, R. S. Tavares, and M. S. G. Tsuzuki, "Influence of Current Injection Pattern and Electric Potential Measurement Strategies in Electrical Impedance Tomography," *Control Engineering Practice*, vol. 58, pp. 276–286, 2017.

[107] T. K. Bera and J. Nagaraju, "Studying the Resistivity Imaging of Chicken Tissue Phantoms with Different Current Patterns in Electrical Impedance Tomography (EIT)," *Measurement*, vol. 45, no. 4, pp. 663–682, 2012.

[108] S. Russo, S. Nefti-Meziani, N. Carbonaro, and A. Tognetti, "A Quantitative Evaluation of Drive Pattern Selection for Optimizing EIT-Based Stretchable Sensors," *Sensors*, vol. 17, no. 9, p. 1999, 2017.

[109] M. R. Islam and M. A. Kiber, "Electrical Impedance Tomography Imaging Using Gauss-Newton Algorithm," in *2014 International Conference on Informatics, Electronics & Vision (ICOEV)*, IEEE, 2014, pp. 1–4.

[110] Y. Zhao, L. Wang, S. Gupta, K. J. Loh, and M. Schagerl, "Comparison of Electrical Impedance Tomography Inverse Solver Approaches for Damage Sensing," in *Nondestructive Characterization and Monitoring of Advanced Materials, Aerospace, and Civil Infrastructure 2017*, International Society for Optics and Photonics, vol. 10169, 2017, p. 1 016 915.

[111] W. Shang, W. Xue, Y. Li, and Y. Xu, "Improved Primal–Dual Interior-Point Method Using the Lawson-Norm for Inverse Problems," *IEEE Access*, vol. 8, pp. 41 053–41 061, 2020.

[112] D. Smyl, S. Bossuyt, W. Ahmad, A. Vavilov, and D. Liu, "An Overview of 38 Least Squares–Based Frameworks for Structural Damage Tomography," *Structural Health Monitoring*, vol. 19, no. 1, pp. 215–239, 2020.

[113] T. N. Tallman and J. A. Hernandez, "The Effect of Error and Regularization Norms on Strain and Damage Identification via Electrical Impedance Tomography in Piezoresistive Nanocomposites," *NDT & E International*, vol. 91, pp. 156–163, 2017.

[114] D. S. Holder, *Electrical Impedance Tomography: Methods, History and Applications*. CRC Press, 2004.

[115] T. N. Tallman, "Conductivity-Based Nanocomposite Structural Health Monitoring via Electrical Impedance Tomography.," PhD thesis, 2015.

[116] H. Hassan, F. Semperlotti, K.-W. Wang, and T. N. Tallman, "Enhanced Imaging of Piezoresistive Nanocomposites Through the Incorporation of Nonlocal Conductivity Changes in Electrical Impedance Tomography," *Journal of Intelligent Material Systems and Structures*, vol. 29, no. 9, pp. 1850–1861, 2018.

[117] D. Liu, D. Smyl, D. Gu, and J. Du, "Shape-Driven Difference Electrical Impedance Tomography," *IEEE Transactions on Medical Imaging*, vol. 39, no. 12, pp. 3801–3812, 2020.

[118] D. Liu, D. Gu, D. Smyl, J. Deng, and J. Du, "B-Spline-Based Sharp Feature Preserving Shape Reconstruction Approach for Electrical Impedance Tomography," *IEEE Transactions on Medical Imaging*, vol. 38, no. 11, pp. 2533–2544, 2019.

[119] D. Liu and J. Du, "A Moving Morphable Components Based Shape Reconstruction Framework for Electrical Impedance Tomography," *IEEE Transactions on Medical Imaging*, vol. 38, no. 12, pp. 2937–2948, 2019.

[120] N. V. Ranade and D. C. Gharpure, "Enhancing Sharp Features by Locally Relaxing Regularization for Reconstructed Images in Electrical Impedance Tomography," *Journal of Electrical Bioimpedance*, vol. 10, no. 1, pp. 2–13, 2019.

[121] D. Goldberg, *Genetic Algorithms in Search, Optimization and Machine Learning*, 1st. Boston, MA, USA: Addison-Wesley Longman Publishing Co., Inc., 1989, ISBN: 0201157675.

[122] M. Mitchell, *An Introduction to Genetic Algorithms*. Cambridge, MA, USA: MIT Press, 1998, ISBN: 0262631857.

[123] S. Raghavan, P. Imbrie, and W. A. Crossley, "Spectral Analysis of R-Lines and Vibronic Sidebands in the Emission Spectrum of Ruby Using Genetic Algorithms," *Applied Spectroscopy*, vol. 62, no. 7, pp. 759–765, 2008.

[124] S. N. Sivanandam and S. N. Deepa, "Genetic algorithms," in *Introduction to Genetic Algorithms*, Springer, 2008, pp. 15–37.

[125] P. J. Van Laarhoven and E. H. Aarts, "Simulated Annealing," in *Simulated Annealing: Theory and Applications*, Springer, 1987, pp. 7–15.

[126] N. Metropolis, A. W. Rosenbluth, M. N. Rosenbluth, A. H. Teller, and E. Teller, "Equation of State Calculations by Fast Computing Machines," *The Journal of Chemical Physics*, vol. 21, no. 6, pp. 1087–1092, 1953.

[127] L. Ingber, "Adaptive Simulated Annealing (ASA): Lessons Learned," *arXiv preprint cs/0001018*, 2000.

[128] J. Yao, Z. Wan, and Y. Fu, "Acceleration Harmonic Estimation for Hydraulic Servo Shaking Table by Using Simulated Annealing Algorithm," *Applied Sciences*, vol. 8, no. 4, p. 524, 2018.

[129] J. Kennedy and R. Eberhart, "Particle Swarm Optimization," in *Proceedings of ICNN'95 - International Conference on Neural Networks*, IEEE, vol. 4, 1995, pp. 1942–1948.

[130] E. Mezura-Montes and C. A. C. Coello, "Constraint-Handling in Nature-Inspired Numerical Optimization: Past, Present and Future," *Swarm and Evolutionary Computation*, vol. 1, no. 4, pp. 173–194, 2011.

[131] M. E. H. Pedersen, "Good Parameters for Particle Swarm Optimization," *Hvass Lab., Copenhagen, Denmark, Tech. Rep. HL1001*, pp. 1551–3203, 2010.

[132] T. N. Tallman and K. W. Wang, "An Inverse Methodology for Calculating Strains from Conductivity Changes in Piezoresistive Nanocomposites," *Smart Materials and Structures*, vol. 25, no. 11, p. 115 046, 2016.

[133] T. N. Tallman, S. Gungor, G. M. Koo, and C. E. Bakis, "On the Inverse Determination of Displacements, Strains, and Stresses in a Carbon Nanofiber/Polyurethane Nanocomposite from Conductivity Data Obtained via Electrical Impedance Tomography," *Journal of Intelligent Material Systems and Structures*, vol. 28, no. 18, pp. 2617–2629, 2017.

[134] D. D. L. Chung, "A Critical Review of Piezoresistivity and its Application in Electrical-Resistance-Based Strain Sensing," *Journal of Materials Science*, pp. 1–30, 2020.

[135] N. Hu, Z. Masuda, G. Yamamoto, H. Fukunaga, T. Hashida, and J. Qiu, "Effect of Fabrication Process on Electrical Properties of Polymer/Multi-Wall Carbon Nanotube Nanocomposites," *Composites Part A: Applied Science and Manufacturing*, vol. 39, no. 5, pp. 893–903, 2008.

[136] R. Rahman and P. Servati, "Effects of Inter-Tube Distance and Alignment on Tunnelling Resistance and Strain Sensitivity of Nanotube/Polymer Composite Films," *Nanotechnology*, vol. 23, no. 5, p. 055 703, 2012.

[137] X. Ren, A. K. Chaurasia, and G. D. Seidel, "Concurrent Multiscale Modeling of Coupling Between Continuum Damage and Piezoresistivity in CNT-Polymer Nanocomposites," *International Journal of Solids and Structures*, vol. 96, pp. 340–354, 2016.

[138] A. K. Chaurasia and G. D. Seidel, "Computational Micromechanics Analysis of Electron Hopping and Interfacial Damage Induced Piezoresistive Response in Carbon Nanotube-Polymer Nanocomposites Subjected to Cyclic Loading Conditions," *European Journal of Mechanics-A/Solids*, vol. 64, pp. 112–130, 2017.

[139] G. M. Koo and T. N. Tallman, "On the Development of Tensorial Deformation-Resistivity Constitutive Relations in Conductive Nanofiller-Modified Composites," in *Smart Materials, Adaptive Structures and Intelligent Systems*, American Society of Mechanical Engineers, vol. 51951, 2018, V002T05A004.

[140] T. N. Tallman and K. W. Wang, "An Arbitrary Strains Carbon Nanotube Composite Piezoresistivity Model for Finite Element Integration," *Applied Physics Letters*, vol. 102, no. 1, p. 011 909, 2013.

[141] T. Takeda, Y. Shindo, Y. Kuronuma, and F. Narita, "Modeling and Characterization of the Electrical Conductivity of Carbon Nanotube-Based Polymer Composites," *Polymer*, vol. 52, no. 17, pp. 3852–3856, 2011.

[142] K. Wang, L. Zhao, H. Hong, J. Zhang, and N. Hu, "An Extended Analytical Model for Predicting the Compressive Failure Behaviors of Composite Laminate With an Arbitrary Elliptical Delamination," *International Journal of Solids and Structures*, vol. 185, pp. 439–447, 2020.

[143] Z. Jia, C. Chen, F. Wang, and C. Zhang, "Analytical Study of Delamination Damage and Delamination-Free Drilling Method of CFRP Composite," *Journal of Materials Processing Technology*, vol. 282, p. 116 665, 2020.

[144] S. Maleki, R. Rafiee, A. Hasannia, and M. R. Habibagahi, "Investigating the Influence of Delamination on the Stiffness of Composite Pipes Under Compressive Transverse Loading Using Cohesive Zone Method," *Frontiers of Structural and Civil Engineering*, vol. 13, no. 6, pp. 1316–1323, 2019.

[145] A. Köllner and C. Völlmecke, "Post-Buckling Behaviour and Delamination Growth Characteristics of Delaminated Composite Plates," *Composite Structures*, vol. 203, pp. 777–788, 2018.

[146] "D638-14 Standard Test Method for Tensile Properties of Plastics," ASTM International, West Conshohocken, PA, Standard, 2014.

[147] D. Engwirda, "Unstructured Mesh Methods for the Navier-Stokes Equations," *Undergraduate Thesis, School of Engineering, University of Sidney*, 2005.

[148] D. Engwirda, "Locally Optimal Delaunay-Refinement and Optimisation-Based Mesh Generation," 2014.

[149] C. E. Smith, G. N. Morscher, and Z. H. Xia, "Monitoring Damage Accumulation in Ceramic Matrix Composites Using Electrical Resistivity," *Scripta Materialia*, vol. 59, no. 4, pp. 463–466, 2008.

[150] H. Chen, L. Miao, Z. Su, Y. Song, M. Han, X. Chen, X. Cheng, D. Chen, and H. Zhang, "Fingertip-Inspired Electronic Skin Based on Triboelectric Sliding Sensing and Porous Piezoresistive Pressure Detection," *Nano Energy*, vol. 40, pp. 65–72, 2017.

[151] S. Makireddi, S. Shivaprasad, G. Kosuri, F. V. Varghese, and K. Balasubramaniam, "Electro-Elastic and Piezoresistive Behavior of Flexible MWCNT/PMMA Nanocomposite Films Prepared by Solvent Casting Method for Structural Health Monitoring Applications," *Composites Science and Technology*, vol. 118, pp. 101–107, 2015.

[152] P. Alpuim, S. A. Filonovich, C. M. Costa, P. F. Rocha, M. I. Vasilevskiy, S. Lanceros-Mendez, C. Frias, A. T. Marques, R. Soares, and C. Costa, "Fabrication of a Strain Sensor for Bone Implant Failure Detection Based on Piezoresistive Doped Nanocrystalline Silicon," *Journal of non-crystalline solids*, vol. 354, no. 19-25, pp. 2585–2589, 2008.

[153] Q. Zheng, J.-h. Lee, X. Shen, X. Chen, and J.-K. Kim, "Graphene-Based Wearable Piezoresistive Physical Sensors," *Materials Today*, 2020.

[154] E. J. Lee, H. Wi, A. L. McEwan, A. Farooq, H. Sohal, E. J. Woo, J. K. Seo, and T. I. Oh, "Design of a Microscopic Electrical Impedance Tomography System for 3D Continuous Non-Destructive Monitoring of Tissue Culture," *Biomedical engineering online*, vol. 13, no. 1, pp. 1–15, 2014.

[155] L. Zhao, T. Tallman, and G. Lin, "Spatial Damage Characterization in Self-Sensing Materials via Neural Network-Aided Electrical Impedance Tomography: A Computational Study," *arXiv preprint arXiv:2010.01674*, 2020.

[156] H. Ghaednia, C. E. Owens, L. E. Keiderling, K. M. Varadarajan, A. J. Hart, J. H. Schwab, and T. N. Tallman, "Is Machine Learning Able to Detect and Classify Failure in Piezoresistive Bone Cement Based on Electrical Signals?" *arXiv preprint arXiv:2010.12147*, 2020.

A. DETAILED FORWARD PROBLEM FORMULATION

A.1 Introduction

This appendix has been adapted from reference [115] and gives a detailed FE formulation of the EIT forward problem with explicit solutions for the complete electrode model (CEM) matrices. Indicial notation is used unless otherwise stated. Repeated indices in the subscripts indicate summation over the dimension of the problem unless a summation operator is explicitly included. Superscripts are reserved for element or node quantities and conductivity is assumed to be a general second-order tensor. Linear triangular elements in two dimensions and linear hexahedral elements in three dimensions were used in this research. However, this appendix only presents the FE formulation of the CEM matrices for linear triangular elements. This formulation can be easily extended to 3-D and to elements with higher-order interpolation functions.

A.2 Formulation and Discretization of the Weak Form for Steady-State Diffusion

The governing equation for steady-state diffusion is Laplace's equation, shown below.

$$-\frac{\partial j_i}{\partial x_i} = \frac{\partial}{\partial x_i}\sigma_{ij}\frac{\partial \phi}{\partial x_j} = f \tag{A.1}$$

In the above, j_i is the current density vector, σ_{ij} is the conductivity tensor, ϕ is the domain potential, and f is an internal current source. It is then assumed that current only flows through the active electrodes and no current flows through the boundary, as described by the following equations.

$$\int_{E_l} \sigma_{ij}\frac{\partial \phi}{\partial x_i} n_j \, \mathrm{d}S_l = I_l \tag{A.2}$$

$$\sigma_{ij}\frac{\partial \phi}{\partial x_i} n_j = 0 \text{ off } \bigcup_{l=1}^{L} E_l \tag{A.3}$$

In the above equations, E_l is the length of the lth electrode, n_j is an outward pointing normal vector, I_l is the current through the lth electrode, and L is the total number of electrodes. Conservation of charge is then enforced as shown in the following equation.

$$\sum_{l=1}^{L} I_l = 0 \tag{A.4}$$

The weak form of equation (A.1) is formed by multiplying both sides by an arbitrary weighting function, ψ, that satisfies the Dirichlet boundary conditions and integrating over the domain, Ω, as shown in the following equation.

$$\int_{\Omega} \psi \frac{\partial}{\partial x_j} \sigma_{ij} \frac{\partial \phi}{\partial x_j} \mathrm{d}\Omega = \int_{\Omega} \psi f \mathrm{d}\Omega \tag{A.5}$$

In the absence of internal current sources, $f = 0$ and equation (A.5) can be rewritten as equation (A.6) using the vector identity $\frac{\partial}{\partial x_j} \psi \sigma_{ij} \frac{\partial \phi}{\partial x_i} = \frac{\partial \psi}{\partial x_i} \sigma_{ij} \frac{\partial \phi}{\partial x_j} + \psi \frac{\partial}{\partial x_j} \sigma_{ij} \frac{\partial \phi}{\partial x_j}$.

$$\int_{\Omega} \frac{\partial}{\partial x_j} \psi \sigma_{ij} \frac{\partial \phi}{\partial x_i} \, \mathrm{d}\Omega - \int_{\Omega} \frac{\partial \psi}{\partial x_i} \sigma_{ij} \frac{\partial \phi}{\partial x_j} \, \mathrm{d}\Omega \tag{A.6}$$

Using the divergence theorem, equation (A.6) can be rewritten as equation (A.7), where Γ is the union of the electrode areas.

$$\int_{\Omega} \frac{\partial}{\partial x_j} \sigma_{ij} \frac{\partial \phi}{\partial x_i} \, \mathrm{d}\Omega = \int_{\partial\Omega} \psi \sigma_{ij} \frac{\partial \phi}{\partial x_i} n_j \, \mathrm{d}S = \int_{\Gamma} \sigma_{ij} \frac{\partial \phi}{\partial x_j} n_j \psi \, \mathrm{d}S \tag{A.7}$$

Next, substituting the domain-electrode CEM boundary condition in equation (3.2) into equation (A.7) gives the following equation.

$$\int_{\Omega} \frac{\partial \phi}{\partial x_i} \sigma_{ij} \frac{\partial \phi}{\partial x_j} \, \mathrm{d}\Omega = \sum_{l=1}^{L} \int_{E_l} \frac{1}{z_l} (V_l - \phi) \psi \, \mathrm{d}S_l \tag{A.8}$$

Discretizing equation (A.8) using finite element results in equation (A.9), where e is the element number and ϕ_e and ψ_e are element-wise quantities defined as shown in equations (A.10) and (A.11), respectively.

$$\sum_{e} \int_{\Omega_e} \frac{\partial \psi_e}{\partial x_i} \sigma_{ij} \frac{\partial \phi_e}{\partial x_j} \, \mathrm{d}\Omega_e = \sum_{e} \sum_{l=1}^{L} \int_{\partial\Omega_e} \frac{1}{z_l} (V_l - \phi_e) \psi_e \, \mathrm{d}S_e \tag{A.9}$$

$$\phi_e = \sum_{A=1}^{N} w^A d_e^A \tag{A.10}$$

$$\psi_e = \sum_{A=1}^{N} w^A c_e^A \tag{A.11}$$

In the preceding equations, A is the node number, w^A is the Ath interpolation function, d_e^A is the potential solution at the Ath node of the eth element, and c_e^A is the variation of the Ath node of the eth element. The operator $\sum_e$ implies assembly over all elements in the discretized domain.

A.3 Formulation of CEM Matrices

Substituting the expressions for ϕ_e and ψ_e into the right hand side of equation (A.9) gives equation (A.12).

$$\int_{\Omega_e} \frac{\partial \psi_e}{\partial x_i} \sigma_{ij} \frac{\partial \phi_e}{\partial x_j} \, \mathrm{d}\Omega_e = \sum_{A=1}^{N} \sum_{B=1}^{N} c_e^A \int_{\Omega_e} \frac{\partial w^A}{\partial x_i} \sigma_{ij} \frac{\partial w^B}{\partial x_j} \mathrm{d}\Omega_e \, d_e^A \tag{A.12}$$

In the above equation, d_e^A and c_e^A have been moved outside the integral since they are constant with respect to Ω_e. In order to efficiently solve equation (A.12), interpolation functions are defined on an isoparametric domain, as shown in equation (A.13), where x_i^A is the i-coordinate of the Ath node and ζ is defined in the range of 0 to 1.

$$x_i = \sum_{A=1}^{N} w^A(\zeta) x_i^A \tag{A.13}$$

Next, using the chain rule of differentiation, $\frac{\partial w^A}{\partial x_i} = \frac{\partial w^A}{\partial \zeta_j} \frac{\partial \zeta_j}{\partial x_i}$, equation (A.12) can be rewritten as equation (A.14).

$$\int_{\Omega_e} \frac{\partial \psi_e}{\partial x_i} \sigma_{ij} \frac{\partial \phi_e}{\partial x_j} \, \mathrm{d}\Omega_e = \sum_{A=1}^{N} \sum_{B=1}^{N} c_e^A \int_{\Omega_{e_\zeta}} \frac{\partial w^A}{\partial \zeta_k} \frac{\partial \zeta_k}{\partial x_i} \sigma_{ij} \frac{\partial w^B}{\partial \zeta_l} \frac{\partial \zeta_l}{\partial x_j} \, \mathrm{d}\Omega_e \, d_e^B \tag{A.14}$$

Because of isoparametric mapping, the above integral can be evaluated exactly using numerical quadrature with appropriate Lagrange polynomials. For triangular elements in two dimensions, the interpolation functions are $w^1 = \zeta_1$, $w^2 = \zeta_2$, and $w^3 = 1 - \zeta_1 - \zeta_2$. For

line elements in one dimension, $w^1 = \frac{1}{2}(1-\zeta)$ and $w^2 = \frac{1}{2}(1+\zeta)$. To compute the integral in equation (A.14) in the isoparametric domain, Ω_{e_ζ}, the integrand must be multiplied with the determinant of the Jacobian of the coordinate transformation, $\left|\frac{\partial x_i}{\partial \zeta_j}\right|$. The resulting integral is shown in equation (A.15).

$$\int_{\Omega_e} \frac{\partial \psi_e}{\partial x_i} \sigma_{ij} \frac{\partial \phi_e}{\partial x_j} \, \mathrm{d}\Omega_e = \sum_{A=1}^{N} \sum_{B=1}^{N} c_e^A \int_{\Omega_{e_\zeta}} \frac{\partial w^A}{\partial \zeta_k} \frac{\partial \zeta_k}{\partial x_i} \sigma_{ij} \frac{\partial w^B}{\partial \zeta_l} \frac{\partial \zeta_l}{\partial x_j} \left| \frac{\partial x_i}{\partial \zeta_j} \right| \, \mathrm{d}\Omega_{e_\zeta} \, d_e^B \tag{A.15}$$

The integral in equation (A.15) can be computed as a sum of weighted polynomials evaluated at quadrature points, as shown in equation (A.16).

$$\int_{\Omega_{e_\zeta}} p(\zeta_i) \, \mathrm{d}\Omega_{e_\zeta} = \sum_{m}^{M} a_m p(\zeta_m) \tag{A.16}$$

In the above equation, the summation runs over the number of quadrature points, a_m is the weight associated with the mth quadrature point, and ζ_m is the location of the mth quadrature point in the isoparametric domain. Returning to equation (A.15), since the interpolation functions are know, the local diffusion matrix for the eth element can be formed and equation (A.15) can be rewritten as equation (A.17).

$$\int_{\Omega_e} \frac{\partial \psi_e}{\partial x_i} \sigma_{ij} \frac{\partial \phi_e}{\partial x_j} \, \mathrm{d}\Omega_e = \sum_{A=1}^{N} \sum_{B=1}^{N} c_e^A k_e^{AB} d_e^B = \begin{bmatrix} c_e^1 & c_e^2 & \cdots & c_e^N \end{bmatrix} \boldsymbol{k}_e \begin{bmatrix} d_e^1 \\ d_e^2 \\ \vdots \\ d_e^N \end{bmatrix} \tag{A.17}$$

In the above equation, $\boldsymbol{k}_e$ is the diffusion stiffness matrix for the eth element. The element diffusion stiffness matrices can be assembled into the global diffusion stiffness matrix, $\boldsymbol{A}_M$. For linear triangular elements in two dimensions, $\boldsymbol{k}_e$ can be computed as shown in equation (A.18).

$$\boldsymbol{k}_e = \frac{1}{2}\begin{bmatrix} 1 & 0 \\ 0 & 1 \\ -1 & -1 \end{bmatrix} \begin{bmatrix} x_1^e - x3^e & x_2^e - x_3^e \\ y_1^e - y_3^e & y_2^e - y_3^e \end{bmatrix}^{-1} \begin{bmatrix} \sigma_{11} & \sigma_{12} \\ \sigma_{21} & \sigma_{22} \end{bmatrix} \begin{bmatrix} x_1^e - x3^e & x_2^e - x_3^e \\ y_1^e - y_3^e & y_2^e - y_3^e \end{bmatrix}^{-T} \cdots$$
$$\cdots \begin{bmatrix} 1 & 0 \\ 0 & 1 \\ -1 & -1 \end{bmatrix}^T \left| \begin{bmatrix} x_1^e - x3^e & x_2^e - x_3^e \\ y_1^e - y_3^e & y_2^e - y_3^e \end{bmatrix} \right| \tag{A.18}$$

In the above equation, x_i^e and y_i^e are the x- and y-coordinates, respectively, of the ith node of the eth element. Next, the matrices $\boldsymbol{A}_Z$, $\boldsymbol{A}_W$, and $\boldsymbol{A}_D$ can be formed by considering the remaining integrals in equation (A.9), as follows.

$$\sum_e \int_{\Omega_e} \frac{1}{z_l}(V_l - \phi_e)\psi_e \, \mathrm{d}S_e = \sum_e \left(- \int_{\partial\Omega_e} \frac{1}{z_l}\phi_e\psi_e \, \mathrm{d}S_e + \int_{\partial\Omega_e} \frac{1}{z_l} V_l \psi_e \, \mathrm{d}S_e \right) \tag{A.19}$$

The matrices $\boldsymbol{A}_Z$ and $\boldsymbol{A}_W$ can be formed by moving the right hand side of equation (A.19) to the left hand side of equation (A.9) and substituting the expressions for ϕ_e and ψ_e from equations (A.10) and (A.11). Matrix $\boldsymbol{A}_Z$ is then formed using the first integral on the right hand side of equation (A.19) and considering the eth element of the lth electrode, as shown in the following equation.

$$\begin{aligned} \int_{\Omega_e} \frac{1}{z_l}\phi_e\psi_e \, \mathrm{d}S_e &= \sum_{A=1}^{N}\sum_{B=1}^{N} c_e^A \int_{\Omega_e} \frac{1}{z_l} w^A w^B \, \mathrm{d}S_e \, d_e^B \\ &= \begin{bmatrix} c_e^1 & c_e^2 & \cdots & c_e^N \end{bmatrix} \boldsymbol{A}_Z^{e\,l} \begin{bmatrix} d_e^1 \\ d_e^2 \\ \vdots \\ d_e^N \end{bmatrix} \end{aligned} \tag{A.20}$$

In two dimensional analysis, the integral in equation (A.20) is evaluated over the length of an electrode. As such, the interpolation functions are $w^1 = \frac{1}{2}(1+\zeta)$ and $\frac{1}{2}(1-\zeta)$. The $\boldsymbol{A}_Z$ matrix of the eth element of the lth electrode can then be formed as shown in the following equation.

$$\begin{aligned} \boldsymbol{A}_Z^{e\,l} &= \int_{-1}^{1} \frac{h^e}{8z_l} \begin{bmatrix} 1-2\zeta+\zeta^2 & 1-\zeta^2 \\ 1-\zeta^2 & 1+2\zeta-\zeta^2 \end{bmatrix} \\ &= \frac{h^e}{6z_l} \begin{bmatrix} 2 & 1 \\ 1 & 2 \end{bmatrix} \end{aligned} \tag{A.21}$$

In the above equation, h^e is the length of the eth line element. $\boldsymbol{A}_Z^{e\,l}$ is formed for every line element that is part of an electrode. The individual $\boldsymbol{A}_Z^{e\,l}$ matrices are then assembled into the global $\boldsymbol{A}_Z$ matrix. Next, $\boldsymbol{A}_W$ is formed using the second integral on the right hand side of equation (A.19) and considering the eth element of the lth electrode as follows.

$$\begin{aligned} -\int_{\Omega_e} \frac{1}{z_l}\psi_e V_l \,\mathrm{d}S_e &= -\sum_{A=1}^{N} c_e^A \int_{\Omega_e} \frac{1}{z_l} w^A \,\mathrm{d}S_e \, V_l \\ &= \begin{bmatrix} c_e^1 & c_e^2 & \cdots & c_e^N \end{bmatrix} \boldsymbol{A}_W^{e\,l} V_l \end{aligned} \tag{A.22}$$

In equation (A.22), V_l has been pulled out from the integral because the voltage is assumed to be constant at each electrode. In two dimensional analysis (using interpolation functions for linear line elements), the $\boldsymbol{A}_W$ column vector of the eth element of the lth electrode is then formed as shown in equation (A.23).

$$\begin{aligned} \boldsymbol{A}_W^{e\,l} &= -\int_{-1}^{1} \frac{h^e}{2z_l} \begin{bmatrix} \frac{1}{2}(1-\zeta) \\ \frac{1}{2}(1+\zeta) \end{bmatrix} \\ &= -\frac{h^e}{2z_l} \begin{bmatrix} 1 \\ 1 \end{bmatrix} \end{aligned} \tag{A.23}$$

Lastly, the $\boldsymbol{A}_D$ matrix is computed by considering the total current in the system and enforcing conservation of charge (equation (A.4)). The current through the lth electrode is then given by the following equation.

$$I_l = \int_{E_l} \frac{1}{z_l}(V_l - \phi)\,\mathrm{d}S = \frac{1}{z_l}E_l V_l - \int_{E_l} \frac{1}{z_l}\phi\,\mathrm{d}S \tag{A.24}$$

In the above equation, a constant contact impedance is assumed between the domain and electrodes. The first term on the right hand side of equation (A.24) relates the electrode current to the electrode voltage by E_l/z_l and the second term on the right hand side of equation (A.24) is similar to equation (A.22) but with the nodal solution, ϕ_e, instead of the nodal variation, ψ_e. This term accounts for coupling between the domain voltage and the electrode voltage via $\boldsymbol{A}_W$. Therefore, $\boldsymbol{A}_D$ is a square matrix with a dimension equal to the number of elements in the electrodes. The diagonal entries of $\boldsymbol{A}_D$ are E_l/z_l while the off-diagonal entries are zero.

A.4 Matrix Assembly

The global $\boldsymbol{A}_M$, $\boldsymbol{A}_Z$, and $\boldsymbol{A}_W$ matrices are formed by assembling the local $\boldsymbol{k}_e$, $\boldsymbol{A}_Z^{e\,l}$, and $\boldsymbol{A}_W^{e\,l}$ matrices. In the following steps, only the assembly of $\boldsymbol{A}_M$ is described. The same steps can be readily applied to assemble $\boldsymbol{A}_Z$ and $\boldsymbol{A}_D$. The assembly process can be easily visualized by considering the global variation and global potential solutions. The global variation vector is $\boldsymbol{c} = \begin{bmatrix} c^1 & c^2 & \cdots & c^n & \cdots & c^N \end{bmatrix}$ where c^n is the variation at the nth node and N is the total number of nodes. Similarly, the global potential solution is $\boldsymbol{d} = \begin{bmatrix} d^1 & d^2 & \cdots & d^n & \cdots & d^N \end{bmatrix}$ where d^n is the nodal potential solution at the nth node and N is the total number of nodes. The assembly process performed over all elements in the domain can then be expressed as shown in equation (A.25).

$$\sum_e \int_{\Omega_e} \frac{\partial \psi_e}{\partial x_i}\sigma_{ij}\frac{\partial \phi_e}{\partial x_j}\,\mathrm{d}\Omega_e = \boldsymbol{c}^T \boldsymbol{A}_M \boldsymbol{d} \tag{A.25}$$

The entries of the local stiffness matrices must be placed in the correct locations in the global stiffness matrix so that they multiply out with the correct nodal variations and nodal

potential solutions. When a node is shared between two elements, the entries corresponding to that node in the local stiffness matrices are summed in the global stiffness matrix. For example, consider the local diffusion stiffness matrices for the eth and $(e+1)$th elements, shown in equations (A.26) and (A.27), respectively.

$$\boldsymbol{c}_e^T \boldsymbol{A}_M^e \boldsymbol{d}_e = \begin{bmatrix} c_e^1 & c_e^2 & c_e^3 \end{bmatrix} \begin{bmatrix} k_e^{11} & k_e^{12} & k_e^{13} \\ k_e^{21} & k_e^{22} & k_e^{23} \\ k_e^{31} & k_e^{32} & k_e^{33} \end{bmatrix} \begin{bmatrix} d_e^1 \\ d_e^2 \\ d_e^3 \end{bmatrix} \tag{A.26}$$

$$\boldsymbol{c}_{e+1}^T \boldsymbol{A}_M^{e+1} \boldsymbol{d}_{e+1} = \begin{bmatrix} c_{e+1}^1 & c_{e+1}^2 & c_{e+1}^3 \end{bmatrix} \begin{bmatrix} k_{e+1}^{11} & k_{e+1}^{12} & k_{e+1}^{13} \\ k_{e+1}^{21} & k_{e+1}^{22} & k_{e+1}^{23} \\ k_{e+1}^{31} & k_{e+1}^{32} & k_{e+1}^{33} \end{bmatrix} \begin{bmatrix} d_{e+1}^1 \\ d_{e+1}^2 \\ d_{e+1}^3 \end{bmatrix} \tag{A.27}$$

Next, assume that the local variation and potential solution of the eth element map to the following global variation and potential solution.

$$\begin{bmatrix} c_e^1 & c_e^2 & c_e^3 \end{bmatrix} \mapsto \begin{bmatrix} c^{n-1} & c^n & c^{n+1} \end{bmatrix} \tag{A.28}$$

$$\begin{bmatrix} d_e^1 & d_e^2 & d_e^3 \end{bmatrix} \mapsto \begin{bmatrix} d^{n-1} & d^n & d^{n+1} \end{bmatrix} \tag{A.29}$$

And, assume that the local variation and potential solution of the $(e+1)$th element map to the following global variation and potential solution.

$$\begin{bmatrix} c_{e+1}^1 & c_{e+1}^2 & c_{e+1}^3 \end{bmatrix} \mapsto \begin{bmatrix} c^n & c^{n+1} & c^{n+2} \end{bmatrix} \tag{A.30}$$

$$\begin{bmatrix} d_{e+1}^1 & d_{e+1}^2 & d_{e+1}^3 \end{bmatrix} \mapsto \begin{bmatrix} d^n & d^{n+1} & d^{n+2} \end{bmatrix} \tag{A.31}$$

$$\boldsymbol{c}^T \boldsymbol{A}_M \boldsymbol{d} = \begin{bmatrix} \vdots \\ c^{n-1} \\ c^n \\ c^{n+1} \\ c^{n+2} \\ \vdots \end{bmatrix}^T \begin{bmatrix} \ddots & & & & & \\ & k_e^{11} & k_e^{12} & k_e^{13} & & \\ & k_e^{21} & k_e^{22} + k_{e+1}^{11} & k_e^{23} + k_{e+1}^{22} & k_{e+1}^{13} & \\ & k_e^{31} & k_e^{32} + k_{e+1}^{21} & k_e^{33} + k_{e+1}^{22} & k_{e+1}^{23} & \\ & & k_{e+1}^{31} & k_{e+1}^{32} & k_{e+1}^{33} & \\ & & & & & \ddots \end{bmatrix} \begin{bmatrix} \vdots \\ d^{n-1} \\ d^n \\ d^{n+1} \\ d^{n+2} \\ \vdots \end{bmatrix} \tag{A.32}$$

The global diffusion stiffness matrix can then be assembled as shown in equation (A.32). Note that since the eth and $(e+1)$th elements share global nodes n and $n+1$, the contributions of these nodes are summed in the global diffusion stiffness matrix. This simple example is meant only to illustrate the assembly process. In a FE mesh consisting of several thousand elements, several nodes will be shared between elements and their contributions will be summed in $\boldsymbol{A}_M$. In such cases, the process of assembling $\boldsymbol{A}_M$ can be efficiently performed using the nodal connectivity matrix. The fundamental assembly process illustrated here can also be applied to $\boldsymbol{A}_Z$ and $\boldsymbol{A}_W$. The only difference is that the degree of freedom for $\boldsymbol{A}_Z$ and $\boldsymbol{A}_W$ is one degree lower than that for $\boldsymbol{A}_M$.

B. DETAILED SENSITIVITY MATRIX CALCULATIONS

This appendix has been adapted from reference [115] and gives a detailed formulation of the sensitivity matrix, $\boldsymbol{J}$, and the exact form for linear triangular elements in two dimensions. This formulation can be readily extended to higher-order interpolation functions and three dimensions. The general form of the sensitivity matrix for anisotropic conductivity is as follows.

$$J_{Q\,Re} = -\int_{\Omega_e} \frac{\partial \phi^Q}{\partial x_i} \sigma_{ij} \frac{\partial \overline{\phi}^R}{\partial x_i} \mathrm{d}\Omega_e \tag{B.1}$$

Indicial notation is used in the above equation and repeated indices indicate summation over the dimension of the problem. Note that QR represents a single index of the sensitivity matrix instead of the previously used MN. This is because MN will be used later for a summation over the nodes of each element. Next, substituting equation (A.10) and (A.11) into equation (B.1) gives the following equation.

$$J_{Q\,Re} = -\sum_{A=1}^{N}\sum_{B=1}^{N} d_e^{AQ} \int_{\Omega_e} \frac{\partial w^A}{\partial x_i} \sigma_{ij} \frac{\partial w^B}{\partial x_j}\, \mathrm{d}\Omega_e\, \overline{d}_e^{BR} \tag{B.2}$$

In equation (B.2), d_e^{AQ} is the potential solution at the Ath node of the eth element due to the Qth current injection, and $\overline{d}_e^{BR}$ is the potential solution at the Bth node of the eth element due to a unit current injection at the Rth electrode pair. Next, similar to equation (A.14), the gradients of the interpolation functions are evaluated using the chain rule of differentiation and substituted into equation (B.2). This gives the following equation.

$$-\int_{\Omega_e} \frac{\partial \phi^Q}{\partial x_i} \sigma_{ij} \frac{\partial \overline{\phi}^R}{\partial x_i} \mathrm{d}\Omega_e = -\sum_{A=1}^{N}\sum_{B=1}^{N} d_e^{AQ} \int_{\Omega_e} \frac{\partial w^A}{\partial \zeta_k} \frac{\partial \zeta_k}{\partial x_i} \sigma_{ij} \frac{\partial w^B}{\partial \zeta_l} \frac{\partial \zeta_l}{\partial x_j}\, \mathrm{d}\Omega_e\, \overline{d}_e^{BR} \tag{B.3}$$

The integral in equation (B.3) is computed in the isoparametric domain by multiplying with the determinant of the Jacobian, $\left|\frac{\partial x_i}{\partial \zeta_j}\right|$, as shown in equation (B.4).

$$-\int_{\Omega_e} \frac{\partial \phi^Q}{\partial x_i}\sigma_{ij}\frac{\partial \overline{\phi}^R}{\partial x_i}\mathrm{d}\Omega_e = -\sum_{A=1}^{N}\sum_{B=1}^{N} d_e^{AQ}\int_{\Omega_{e_\zeta}} \frac{\partial w^A}{\partial \zeta_k}\frac{\partial \zeta_k}{\partial x_i}\sigma_{ij}\frac{\partial w^B}{\partial \zeta_l}\frac{\partial \zeta_l}{\partial x_j}\left|\frac{\partial x_m}{\partial \zeta_n}\right| \mathrm{d}\Omega_{e_\zeta}\, \overline{d}_e^{BR} \tag{B.4}$$

The summation in the above equation can be expressed using matrix-vector notation, as follows.

$$\begin{aligned} -\int_{\Omega_e} \frac{\partial \phi^Q}{\partial x_i}\sigma_{ij}\frac{\partial \overline{\phi}^R}{\partial x_i}\mathrm{d}\Omega_e &= \sum_{A=1}^{N}\sum_{B=1}^{N} d_e^{AQ} j_e^{AB}\overline{d}_e^{BR} \\ &= \begin{bmatrix} d_e^{1Q} & d_e^{2Q} & \cdots & d_e^{NQ} \end{bmatrix} \boldsymbol{j}_e \begin{bmatrix} \overline{d}_e^{1R} \\ \overline{d}_e^{2R} \\ \vdots \\ \overline{d}_e^{NR} \end{bmatrix} \end{aligned} \tag{B.5}$$

For linear triangular elements, the matrix $\boldsymbol{j}_e$ can be evaluated as shown in the following equation.

$$\begin{aligned} \boldsymbol{j}_e = -\frac{1}{2}\begin{bmatrix} 1 & 0 \\ 0 & 1 \\ -1 & -1 \end{bmatrix} \begin{bmatrix} x_1^e - x3^e & x_2^e - x_3^e \\ y_1^e - y_3^e & y_2^e - y_3^e \end{bmatrix}^{-1} \begin{bmatrix} \sigma_{11} & \sigma_{12} \\ \sigma_{21} & \sigma_{22} \end{bmatrix} \begin{bmatrix} x_1^e - x3^e & x_2^e - x_3^e \\ y_1^e - y_3^e & y_2^e - y_3^e \end{bmatrix}^{-T} \cdots \\ \cdots \begin{bmatrix} 1 & 0 \\ 0 & 1 \\ -1 & -1 \end{bmatrix}^T \left|\begin{bmatrix} x_1^e - x3^e & x_2^e - x_3^e \\ y_1^e - y_3^e & y_2^e - y_3^e \end{bmatrix}\right| \end{aligned} \tag{B.6}$$

It is worth noting that the computation of each entry of the sensitivity matrix results in a scalar and not a matrix. This is because the nodal solutions d_e^{AQ} and $\overline{d}_e^{BR}$ are known

quantities that, when multiplied with $\boldsymbol{j}_e$, result in a scalar according to equation (B.5). This is different from the local diffusion stiffness matrix, where each entry is a matrix.

VITA

Education

- MS in Aeronautics and Astronautics, Purdue University, USA, August 2015 – May 2017
- BEng in Aerospace Engineering, University of Sheffield, UK, September 2010 – June 2013

Academic Experience

- Graduate Assistant, School of Aeronautics and Astronautics, Purdue University, USA, January 2016 –May 2021

Publications

- H. Hassan and T. N. Tallman, 2021, "Precise Damage Shaping in Self-Sensing Composites Using Electrical Impedance Tomography and Genetic Algorithm," under review in Composites Part B: Engineering.
- H. Hassan and T. N. Tallman, 2021, "Inverse Determination of Delamination Shape and Size in Self-Sensing Composites Using Electrical Impedance Tomography and Genetic Algorithms," in Sensors and Smart Structures Technologies for Civil, Mechanical, and Aerospace Systems. International Society for Optics and Photonics.
- H. Hassan and T. N. Tallman, 2021, "A Comparison of Metaheuristic Algorithms for Solving the Piezoresistive Inverse Problem in Self-Sensing Materials," in IEEE Sensors Journal, vol. 21, no. 1, pp. 659-666.
- H. Hassan and T. N. Tallman, 2020, "Failure prediction in Self-Sensing Nanocomposites via Genetic Algorithm-Enabled Piezoresistive Inversion," in Structural Health Monitoring, 19(3), pp.765-780.

- H. Hassan and T. N. Tallman, 2020, "Damage Sizing in Self-Sensing Materials Using a Genetic Algorithm-Supplemented Electrical Impedance Tomography Formulation," in Sensors and Smart Structures Technologies for Civil, Mechanical, and Aerospace Systems 2020 (Vol. 11379, p. 113790B). International Society for Optics and Photonics.

- T. N. Tallman and H. Hassan, 2020, "A Computational Exploration of the Effect of Alignment and Aspect Ratio on Alternating Current Conductivity in Carbon Nanofiber–Modified Epoxy," in Journal of Intelligent Material Systems and Structures, 31(5), pp.756-770.

- T. N. Tallman and H. Hassan, 2019, "A Network-Centric Perspective on the Microscale Mechanisms of Complex Impedance in Carbon Nanofiber-Modified Epoxy," in Composites Science and Technology, 181, p.107669.

- H. Hassan and T. N. Tallman, 2019, "Experimental Identification of Stress Concentrations in Piezoresistive Nanocomposites via Electrical Impedance Tomography," In Sensors and Smart Structures Technologies for Civil, Mechanical, and Aerospace Systems (Vol. 10970, p. 109701A). International Society for Optics and Photonics.

- H. Hassan, F. Semperlotti, K. W. Wang, and T. N. Tallman, 2018, "Enhanced Imaging of Piezoresistive Nanocomposites Through the Incorporation of Nonlocal Conductivity Changes in Electrical Impedance Tomography," Journal of Intelligent Material Systems and Structures, 29(9), pp.1850-1861.

- H. Hassan and T. N. Tallman, 2018, "Predicting Failure from Conductivity Changes in Piezoresistive Nanocomposites," In Sensors and Smart Structures Technologies for Civil, Mechanical, and Aerospace Systems 2018 (Vol. 10598, p. 1059805). International Society for Optics and Photonics.